Title

Stem cell models of axial patterning and their implications for V2a neurons and engineered neural systems

Author

Elder, Nicholas

Publication Date

2024

Stem cell models of axial patterning and their implications for V2a neurons and engineered neural systems

by
Nicholas Elder

DISSERTATION
Submitted in partial satisfaction of the requirements for degree of
DOCTOR OF PHILOSOPHY

in

Developmental and Stem Cell Biology

in the

GRADUATE DIVISION
of the
UNIVERSITY OF CALIFORNIA, SAN FRANCISCO

Approved:

DocuSigned by:
Alex Pollen
2102D531BF2D416...
Alex Pollen
Chair

DocuSigned by:
Shipman, Seth
[illegible]41E...
Shipman, Seth

DocuSigned by:
Faranak Fattahi
85BEE21893B74CD...
Faranak Fattahi

Committee Members

Dedication

This work is dedicated to Steven and Anastasia, Luke and Zoe, and Dylan; for their love, compassion, encouragement, examples, and support.

Acknowledgements

Since I first started grad school, time seems to have progressed both slowly and all at once. But throughout it all I have been supported by an amazing community of advisors, mentors, and friends whom I would like to thank here. First and foremost, I would like to thank my advisors, Faranak Fattahi and Todd McDevitt, for their encouragement and support over the years. Not only have they both been phenomenal scientific role models, but they have fostered inclusive, collaborative, and supportive lab environments where I could grow and learn. To Todd, thank you for seeing potential in an over-eager rotation student fresh from undergrad. Though I knew I would enjoy working with you from our first meeting, you had the unenviable job of seeing me through my scientific 'teenage years' full of awkward side projects and not-quite-done experiments. You saw the lab through the pandemic and I came out on the other side a much more skilled and confident scientist with only a modest fear of Calibri font. To Faranak, thank you for welcoming me and my project into your lab. I consistently look forward to our one-on-one meetings where you help to make order from my chaos and show me that there is actually an end in sight. I know that I can always count on your compassion and support and it has made some of the hardest periods of graduate school much easier to bear. You have been an amazing advocate for me in scientific and professional settings as well, for which I will always be grateful. Lastly, I would not have made it into a graduate program at UCSF at all if I hadn't benefitted from excellent undergraduate mentors like Rachid El Bejjani, Malcolm Campbell, and Peter Dempsey.

Many, many thanks also go to the senior graduate students and postdocs who have been teachers and mentors to me over the years: Ashley Libby and David Joy for first teaching me hPSC culture and the value of scientific partnerships; Lana Zholudeva for showing me that I know more than I think I do; Mikayla Richter for demonstrating how phenomenally productive one person can be; Ryan Samuel for commiserating with me over my lack of real coding experience and showing me that it's not that hard when someone can just send you their script;

Homa Majd for being the most scientifically curious and optimistic person I've ever met; and Alireza Majd for making me laugh no matter what. There are many more people who deserve thanks, so to all other lab members of the McDevitt and Fattahi labs, I have learned something from each of you and you have all been integral to my grad school experience. Thank you.

The Developmental and Stem Cell Biology program also provided me with a great community throughout grad school, full of both outstanding scientific peers and also camping buddies and rage cage opponents. Special thanks go to Antara Rao, Nicole Koutsodendris, Ryan Samuel, Karissa Hansen, Reed McMullen, and Eliza Gaylord for making the DSCB community welcoming and fun.

In addition to, and partly an extension of, the DSCB community, I need to thank the group of friends that have truly become a chosen family: Emily Bulger, Matt Keefe, Will Flanigan and Ivana Muncie-Vasic. Words cannot thank you enough for how much you have been there for me over the years, so I'll just say thank you for GF crackers, board games, avoiding board games, dancing, camping, and road trips in minivans. You all are the best. In addition to this group of friends in San Francisco, I have been fortunate to have an extended network of friends down in the Palo Alto area as well. Thank you to the Bhatt lab members for allowing me to become an honorary member and for asking me far fewer questions about my research.

Finally, I need to thank my family – siblings, grandparents, aunts, uncles, and cousins included. It is hard to articulate all of the ways that you helped me get to where I am, but it was in no doubt due to your support, encouragement, example and love. To my parents, Steven and Anastasia, thank you for your encouragement, for letting me believe that I could set my own course, and for your support wherever I went (which were increasingly large distances with each passing year). It is without doubt that because of you that I am who I am today. To my life partner and best friend, Dylan Maghini, thank you for your enduring love and support and patience. I can't wait to see where we go together.

Contributions

The work presented here was conducted under the supervision of Dr. Todd McDevitt and Dr. Faranak Fattahi. Chapters 2 and 4 represent published, peer reviewed work that can be found using the references below. The work in Chapter 2 was performed in close collaboration with Ashley Libby, David Joy, and Emily Bulger in addition to other listed authors. The work presented in Chapter 3 is currently being assembled into a manuscript for initial submission soon and thus may differ in its final published form.

Citation for Chapter 2:

Libby, A. R. G., Joy, D. A., **Elder, N. H.**, Bulger, E. A., Krakora, M. Z., Gaylord, E. A., Mendoza-Camacho, F., Butts, J. C., & McDevitt, T. C. (2021). Axial elongation of caudalized human organoids mimics aspects of neural tube development. Development, 148(12), dev198275.

Citation for Chapter 4:

Elder, N., Fattahi, F., McDevitt, T. C., & Zholudeva, L. V. (2022). Diseased, differentiated and difficult: Strategies for improved engineering of in vitro neurological systems. Frontiers in Cellular Neuroscience, 16.

Stem cell models of axial patterning and their implications for V2a neurons and engineered neural systems

Nicholas Elder

Abstract

Human pluripotent stem cells have opened up unprecedented opportunities to model human development and disease. Critical to these models is differentiation of stem cells toward relevant cell identities. Axial elongation of the neural tube is crucial during mammalian embryogenesis for anterior-posterior body axis formation and spinal cord development, but these processes cannot be interrogated directly in humans as they occur early post-implantation. However, this developmental period of regionalization significantly influences downstream cell fate. Here, I explore how models of axial patterning influence neural development and how these developmental models can influence engineered neural systems. First, I report an organoid model of neural tube extension derived from human pluripotent stem cell aggregates which recapitulate aspects of the morphological and temporal gene expression patterns of neural tube development. Next, I investigate the effect of early progenitor regionalization on mature V2a interneurons which reside in the hindbrain and spinal cord. Using a multiomic approach, I identify lasting epigenetic and transcriptional differences as a result of early developmental regionalization. The epigenetic differences suggest that uniquely open regions of chromatin are accessed by different transcription factor families, while the differences in transcription point to differences in axonal extension and synapse formation. I also observe differences in spontaneous activity produced from regionally distinct neuron populations. Computational modeling and knockdown

validation studies identify CREB5 and TCF7L2 as mediators of some of the region-specific differences in gene expression. Finally, I show that attempting to 'skip' developmental patterning by induced transcription factor expression yields a population unlike either developmentally relevant V2a population, highlighting the importance of following developmental steps in establishing cell identities *in vitro*. This observation leads me to explore ways to achieve cell type specificity by contrasting directed and induced differentiation strategies and proposing ways they can complement one another to better recapitulate target cell type identity.

Table of Contents

List of Figures

List of Abbreviations

AASV1	adeno-associated virus integration site 1
ALS	amyotrophic lateral sclerosis
ATAC-seq	assay for transposase-accessible chromatin using sequencing
bHLH	basic helix loop helix
BMP	bone morphogenic protein
CDX2	caudal type homeobox 2
cGMP	current good manufacturing principles
ChIP	chromatin immunoprecipitation
CLE	caudal lateral epiblast
CLYBL	citrate lyase beta-like
CNS	central nervous system
COL IV	collagen IV
CPG	central pattern generator
CRISPR	clustered regularly interspaced short palindromic repeats
CRISPRi	clustered regularly interspaced short palindromic repeats mediated inhibition
DAR	differentially accessible region
DEG	differentially expressed gene
DNA	deoxyribonucleic acid
DOX	doxycycline
DREADD	designer receptors exclusively activated by designer drugs
dSMADi	dual SMAD inhibition
EB	embryoid body
EdU	5-ethynyl-2'-deoxyuridine
FDR	false discovery rate

FGF	fibroblast growth factor
FOXN4	forkhead box n4
FP	floor plate
GABA	gamma-amino butyric acid
GFP	green fluorescent protein
GO	gene ontology
GREAT	genomic regions enrichment of annotations tool
GRN	gene regulatory network
GSEA	gene set enrichment analysis
H1	human embryonic stem cell line 1
H7	human embryonic stem cell line 7
H9	human embryonic stem cell line 9
hESC	human embryonic stem cell
hiPSC/iPSC	**(**human) induced pluripotent stem cell
HOX	homeobox
KD	knockdown
MEA	micro electrode array
miRNA	micro ribonucleic acid
MN	motor neuron
mRNA	messenger ribonucleic acid
NE	neuroectoderm
NGN2	neurogenin 2, also NEUROG2
NICD	notch intracellular domain
NMJ	neuromuscular junction
NMP	neuromesodermal progenitor
NPC	neural progenitor cell
OPC	oligodendrocyte precursor cell

p2	ventral progenitor domain 2
PG	paralogous group
pH3	phospho histone 3
PNS	peripheral nervous system
PSC	pluripotent stem cell
pSMAR/SMAR	(plasmid containing) scaffold / matrix attachment regions
PUR	purmorphamine
RA	retinoic acid
RISC	ribonucleic acid induced silencing complex
RFP	red fluorescent protein
RNP	ribonucleoprotein (complex)
ROI	region of interest
sgRNA	single guide ribonucleic acid
SHH	sonic hedgehog
shRNA	short hairpin ribonucleic acid
SMAD	mothers against decapentaplegic
SN	sensory neuron
snATAC-seq	single nucleus assay for transposase-accessible chromatin using sequencing
snRNAs-seq	single nucleus ribonucleic acid sequencing
SOX2	sorry box 2
TALEN	transcription activator-like effector nuclease
TBXT	T-box transcription factor T; Brachyury
TF	transcription factor
TGFb	transforming growth factor beta
TSS	transcriptional start site
UTR	untranslated region

V2a	ventral neuron population 2a
VSX2	visual system homeobox 2, also known as chx10
WNT/Wnt	wingless-related integration site
WTB	wild type B stem cell line
WTC11	wild type C 11 stem cell line, also WTC

CHAPTER 1

Introduction

Axial patterning of the embryo

The early stages of development up to and including the blastocyst stage are characterized by radial symmetry within the embryo. However, starting with the stage called gastrulation, the embryo not only begins to segregate pluripotent stem cells into the major germ lineages, but it also establishes the axes of orientation upon which the rest of the body plan and organs are built (Bénazéraf & Pourquié, 2013). At the time of gastrulation, the most anterior (head) identities are the default, while more posterior identities need to be specified by the action of caudalizing signals (Bénazéraf & Pourquié, 2013; Gouti et al., 2015; Metzis et al., 2018). The source of these signals is the node and primitive streak, which secrete FGF and WNT molecules (Gouti et al., 2014; Mathis et al., 2001; Takemoto et al., 2006, 2011). These signals produce a population of stem cells which divide and expand, building new tissue and 'pushing' the node and primitive streak down the embryo. Some of the tailbud progenitors turn into neural plate and then neural tube with a more epithelial SOX2+ identity, while others migrate into and through the primitive streak and adopt a mesodermal TBXT+ identity and form the paraxially located presomitic mesoderm and later somites (Takemoto et al., 2011). Originally, it was thought that the cells that formed the neural plate and the mesoderm were completely segregated from one another, but a study using sparse cell labeling in mouse embryos provided some of the first evidence that a shared population of 'axial stem cells' could contribute progeny to both the neural plate and neural tube as well as the presomitic and somitic mesoderm on either side of the midline (Tzouanacou et al., 2009). Around the node-streak border (NSB), in a region known as the caudal lateral epiblast or CLE, a population of dividing stem cells acquires an identity known as a neuromesodermal progenitor (NMP) (Cambray & Wilson, 2007; Henrique et al., 2015; Wymeersch et al., 2016, 2019). The NMPs express markers of both neural (SOX2) and mesodermal (TBXT) cells, hence their name. While these two germ layers are distinct from one another during anterior patterning, the NMP cells balance these two fates in the posterior embryo while exposed to the signals emanating from the NSB (Cambray & Wilson, 2007; Henrique et al., 2015).

The combination of FGF and WNT at the NSB and CLE further induces NMPs to express HOX genes. HOX genes are a family of evolutionarily conserved transcription factors (TFs) whose expression pattern and activity help to delineate distinct body segments and regions (Dasen & Jessell, 2009; Philippidou & Dasen, 2013). Therefore, these HOX genes can act as a type of 'zip code' for the body. The expression of different sets of HOX genes in NMPs can control how quickly and in what order they exit the primitive streak to become trunk tissue (Denans et al., 2015; Iimura & Pourquié, 2006). Humans have 33 hox genes, arranged in 4 clusters (HOXA-D) on separate chromosomes. Within each cluster, there are up to 13 distinct hox paralogs (i.e., HOXA1-A13) arranged in a linear order and with different groups missing individual members. When a HOX cluster is activated, HOX1 turns on before HOX2 and so on and so forth (Neijts & Deschamps, 2017; Philippidou & Dasen, 2013). This regulated pattern of activation has been termed co-temporal and co-linear, reflecting the time it takes for them to become expressed and their physical location on the chromosome. More posterior HOX genes also exhibit posterior dominance over more anterior HOX genes, meaning that the HOX identity of any cell can be represented by the largest HOX gene expressed. Work *in vitro* and *in vivo* has shown that FGF and RA are sufficient to turn on the first 5 HOX paralogous groups, representing mostly caudal hindbrain cell types in the CNS (Butts et al., 2017; Frank & Sela-Donenfeld, 2019; Gould et al., 1998; Gouti et al., 2014; Metzis et al., 2018). However, coordinated action of FGF and WNT, as well as a HOX regulator CDX is necessary to turn on trunk hox groups (HOX6-9), and yet another molecule GDF11 is needed to stimulate the most posterior HOX genes (HOX10-13) (Aires et al., 2019; Bulajić et al., 2020; Lippmann et al., 2015; Mazzoni et al., 2013; Neijts et al., 2017). These coordinated groupings are regulated by the chromatin accessibility of the HOX clusters, as shown with ATAC- and ChIP-seq (Mazzoni et al., 2013; Neijts et al., 2017; Rekaik et al., 2023).

In summary, the head-tail axis of the body is established during and following gastrulation by a process of posterior elongation. This elongation is achieved in part by NMPs, which are specified by signals originating from the receding structures of the node and primitive streak, and which can form tissues of the neural tube and somites. During posterior elongation, NMPs upregulate HOX genes which delineate regions of the body by their clustered sequential expression as well as influencing downstream mature cell fate.

Models of axial patterning *in vitro*

Well before the discovery of NMP's, scientists had noted the effects of WNT and retinoic acid (RA) signaling on promoting embryonic structures posterior to the head by studying their effect on model organisms (Cho & De Robertis, 1990; Maden, 2002). However, the discoveries of how to produce and culture human embryonic and induced pluripotent stem cells led to the very real prospect of studying developmental processes in a wholly human context *in vitro* (Takahashi et al., 2007; Takahashi & Yamanaka, 2006; Thomson et al., 1998). Classic approaches to differentiation, or the process by which a stem cell changes and refines its identity, typically involved a uniform treatment of cells grown in monolayer or allowing a short period of 3D aggregation into structures called 'embryoid bodies' or EBs (Carpenedo et al., 2007; Eiraku et al., 2008, 2011). Signaling within the embryoid body mimics some of the aspects of embryo development, leading to the generation of distinct germ layers after a few days (Carpenedo et al., 2007). After an early EB stage, the cells are plated back down to 2D adherent plates for further differentiation, selection, and expansion or maintained in 3D culture. Improved stem cell culture methods and small molecule agonists and antagonists for developmental signaling pathways have allowed researchers to access more posterior tissues than had been previously available. A starting point for much of this work is with the NMPs, where cells are posteriorized and HOX gene expression is induced (Cooper et al., 2020; Gouti et al., 2014; Lippmann et al., 2015; Verrier et al., 2018). Given the co-temporal regulation of HOX gene expression, the time that NMPs are cultured can directly relate to which HOX genes are activated, with more time spent as an NMP correlating with the expression of more and more posterior HOX genes (Cooper et al., 2020; Lippmann et al., 2015). Another approach has been to model a range of anterior-posterior fates in a single differentiation by using microfluidic devices to create a stable gradient of Wnt signaling across a population of cells, resulting in brain-like populations on one side, and hindbrain-like populations on the other (Rifes et al., 2020; Xue et al., 2024). This continuous approach contrasts with 'assembloids' where cells are specified to different brain regions separately and then physically joined together to create desired circuits (Andersen et al., 2020). However, the model axial patterning that has gained the most traction in recent years is that of the gastruloid.

The first gastruloid, so called for being a defined 'unit' of cells that produced germ-layer patterning, was created by plating hPSCs onto a surface that had been stamped with extracellular matrix, restricting hPSC attachment to the stamped regions, in this case uniform circles (Warmflash et al., 2014). Once cells reached confluency, a short pulse of BMP generated a radially patterned colony with extraembryonic tissue on the outside, followed by a mixed ring of mesoderm and endoderm, and an interior ectoderm. The ability to replicate such a robust pattern has led groups to use this to model and study gene networks controlling early gene regulation in the context of different morphogens and genetic perturbations (Bulger, McDevitt, et al., 2024; Bulger, Muncie-Vasic, et al., 2024; Kaul et al., 2023; Martyn et al., 2018, 2019). However, these radial 2D gastruloids lack distinct body axes as we know them, limiting their utility in describing the processes which occur in a specifically posterior population of cells. Following these early 2D models came 3D gastruloids. First shown using mouse cells, and later with human, these structures started as aggregates of pluripotent stem cells similar to embryoid bodies, but were given a short pulse of Wnt agonist. After a few days, not only had multiple germ layers emerged, but the ball of cells broke symmetry and elongated, with a population of TBXT+ progenitors found at the 'tail' of the gastruloid (Beccari et al., 2018; Moris et al., 2020; van den Brink et al., 2014). Further tinkering with the methods revealed that adding extra cellular matrix to the gastruloids can promote the formation of budded somite-like structures surrounding a putative neural tube (Veenvliet et al., 2020, 2021).

These models of axial patterning have advanced the fields of developmental biology and regenerative medicine in several ways. Frist, the period of gastrulation happens early in development, around 14 days in the human, right around the time when mammalian embryos implant in the uterine wall and well before most people know they are pregnant, making it difficult to access human tissue from elective abortions notwithstanding the legal and ethical hurdles which are also faced. While animal models are more easily accessible, they differ sufficiently in gastrula shape (mice) and genetic background (chicken) so as to complicate many findings (Sheng, 2015). Second, while many human stem cell differentiation protocols are able to recapitulate a series of developmental cues to achieve target cell types, they typically lack the physical interplay between multiple germ layers and mechanical and morphological changes that occur at a tissue scale. Gastruloids by contrast have the potential to display sustained and concerted cell movement and to contain discrete signaling compartments, allowing us to study the effects of mutations or teratogens at something approaching a tissue if not an organismal scale. Lastly, while the proponents of gastruloids admire that they contain multiple germ layers and form structures that are remarkably similar to those formed in the developing embryo, they also uniformly acknowledge that gastruloids are not themselves embryos and cannot sustain ‘life’ in a philosophical and ethical sense. Therefore, these models of axial elongation do not require the same ethical considerations that would be necessary to study the same developmental period in human tissue.

Neural tube patterning and neuron subtype specification

Following specification of the neural plate during gastrulation and elongation is the folding and closure of the neural tube. Neural tube closure progresses by the formation of several hinge points within the neural plate mediated by cell polarization, actomyosin contraction, and a folding of the epithelium where the neural plate meets the neural crest and non-neural ectoderm regions (Karzbrun et al., 2021; Nikolopoulou et al., 2017). When the two sides of the neural tube meet, they fuse, creating the neural tube which is overlaid with non-neural ectoderm and which has paraxial mesoderm on either side and the notochord underneath. The neural tube goes on to develop into the central nervous system (CNS), which includes the brain and spinal cord. The neural tube is an easily identifiable structure in early embryos and has turned out to be an excellent model system to study how patterns are imposed and interpreted during development.

Patterning within the neural tube occurs along a highly stereotyped dorsal-ventral axis formed by opposing signaling gradients (Andrews et al., 2019; Dessaud et al., 2008; Jessell, 2000; Lu et al., 2015; Ulloa et al., 2007). Ventral to the neural tube is the notochord, a mesoderm-derived structure that secretes high levels of SHH. The most ventral cells of the neural tube become the floor plate, and also secrete SHH in response (Cruz et al., 2010; Placzek & Briscoe, 2005). At the dorsal side of the neural tube, the surface ectoderm induces the generation of opposing roof plate cells which secrete WNT and BMP molecules (Lu et al., 2015; Rekler & Kalcheim, 2021). Differential strength or duration of these signaling molecules patterns the neural tube into 11 layered progenitor domains (Lu et al., 2015). Within the ventral spinal cord, the strength of the SHH signal from the notochord/floor plate is interpreted by the neural progenitors to induce expression of transcription factors which oppose the action of another set which are expressed independently of SHH. Less straightforward mechanisms appear to act in the dorsal spinal cord, where discrete combinations of BMP and WNT ligands may be necessary for subtype specification. The progenitors from each of the 11 developmentally defined regions go on to migrate, mature, and intermingle within the spinal cord, and further diversify into several subclasses of neurons which form the local circuits for sensory relay and locomotion.

V2a interneurons

One of the neuron populations arising from SHH signaling in the ventral spinal cord are called the V2a interneurons. The V2a population is developmentally defined as arising from the FOXN4-expressing p2 progenitor domain immediately dorsal to the pMN/motor neuron domain (Del Barrio et al., 2007; Li et al., 2005; Lu et al., 2015; Thaler et al., 2002). Note, I use the term 'developmentally defined' to distinguish from spinal neuron classes or identities which are defined by circuit or electrophysiological function, such as the Renshaw cell (Moore et al., 2015). The p2 domain subdivides into V2a, V2b, and V2c domains, each with unique markers. The generation of V2a and V2b neurons, which make up the majority of the V2 population, is dependent on Notch signaling, with V2a neurons requiring Notch inhibition and V2b cells requiring Notch activation (Del Barrio et al., 2007; Misra et al., 2014; Mizoguchi et al., 2020). Little is known about how the V2c population is specified, but it is thought to be more similar to the V2b lineage (Panayi et al., 2010). After Notch-dependent specification, the V2a go on to become glutamatergic excitatory neurons, while V2b become GABAergic inhibitory neurons. Committed V2a neurons canonically express the transcription factor VSX2 (also known as Chx10), though expression wanes in mature tissues (Clovis et al., 2016; Debrulle et al., 2019; Hayashi et al., 2018).

Broadly speaking, a V2a neuron is defined as an excitatory, ipsilateral interneuron with a descending (posteriorly) projecting axon and which expresses or has expressed VSX2. V2a neurons are found throughout the hindbrain and spinal cord at a relatively uniform density and have been implicated in phrenic and locomotor circuits (Ampatzis et al., 2014; Crone et al., 2009; Hayashi et al., 2018; McCreedy et al., 2021; Zholudeva et al., 2017). Of course, there is also heterogeneity within the V2a population. Studies in mice and zebrafish have identified an anterior subset of V2a neurons with ascending and descending projections, as well as V2a neurons with distinctive patterns of activity and recruitment order during locomotion or swimming (Hayashi et al., 2018; Menelaou et al., 2014; Menelaou & McLean, 2019). However, one of the most intriguing aspects of the V2a population is its potential for plasticity and circuit repair after spinal cord injury. The central nervous system has long been known to have little to no regenerative potential. Neurons lost to damage cannot be replaced and negligible regrowth of axons occurs across lesions. While V2a neurons do not divide to produce new V2a neurons, a growing body of evidence points to V2a neurons as having a somewhat unique degree of plasticity which allows them to form collateral axonal branches and establish new connections in a stressed or post-injury environment. Groundbreaking work on spinal cord injury has shown that mice, rats, and humans with injured spinal cords can regain some ability to walk and control limbs beneath the lesion site autonomously when rehabilitated with epidural electrical stimulation (Kathe et al., 2022; Matson et al., 2022; Squair et al., 2023). With rehabilitation and electric therapy, spared descending tracts of reticulospinal neurons make new connections onto VSX2-expressing V2a neurons in the lumbar spinal cord (Kathe et al., 2022). This is a specific effect, since silencing of the V2a population results in loss of the lower limb control. V2a neurons can also be recruited into phrenic circuits controlling diaphragm function after cervical spinal cord hemisection (Zholudeva et al., 2017). Beyond this endogenous ability to restore some function, V2a neurons also possess attractive qualities for cell-based therapies, being excitatory neurons that send descending connections onto motor neurons (Zholudeva, Qiang, et al., 2018; Zholudeva & Lane, 2019). These qualities make V2a neurons more likely to be able to bridge the loss of synaptic communication that results from injury and to be able to target the major cell type directly responsible for 'function' – the motor neurons. Transplantation of V2a neurons into a spinal cord lesion in rats has also yielded promising results, with transsynaptic tracing showing new connections being made through the neurons transplanted into the lesion site and a gain of function of target diaphragm muscle activity (Zholudeva et al., 2024; Zholudeva, Iyer, et al., 2018). Perhaps the use of transplantation and electrical therapy together could go even further to restore circuit function after spinal cord injury and drastically improve the quality of life for patients.

Transplantation studies require a source of V2a neurons. While some groups have isolated mixed fetal cell populations for such purposes, outcomes are better when populations are enriched for cells like V2a neurons with desirable qualities (Kadoya et al., 2016; Kumamaru et al., 2018; Zholudeva, Iyer, et al., 2018). To this end, robust protocols to derive V2a neurons from mouse and human stem cells have been published (Butts et al., 2017, 2019). These protocols focus on recapitulating three main signaling pathways to generate V2a neurons: SHH, Notch, and retinoic acid (RA). Not only are these protocols valuable resources which will aid in the production of V2a neurons for potential therapeutic studies, but they also allow for exploration of the biology of human V2a neurons. Other neuron types, such as motor neurons and V1 neurons, have been described to have numerous subclasses and physical arrangements within the spinal cord as a result of axial patterning and HOX genes (Hoang et al., 2018; Philippidou & Dasen, 2013; Sweeney et al., 2018). Why not the V2a neurons? V2a neurons are found along the entire length of the spinal cord and are therefore involved in all of the various functions that the spinal cord locally regulates, from breathing to walking to blood pressure control. Axial location is just as likely to regulate aspects of V2a development as any other interneuron population and perhaps one such axially specific population could be even more therapeutically beneficial. However, this cannot be tested until discrete populations can be generated using human cells.

Focus of this dissertation

This dissertation broadly focuses on using human pluripotent stem cells to model the process of axial patterning, to examine its effect on V2a neurons, and to lay a path forward for engineering neurons and neural circuits for advanced disease modeling and therapeutic use. Chapter 2 focuses on a stem-cell derived model of axial elongation, similar to that of gastruloids. This work is what led me to be fascinated with NMPs, the spinal cord, and the process of axial patterning generally. Chapter 3 focuses on how deriving V2a neurons from distinct populations of neural progenitors leaves a lasting impact on the genetic regulation and function of V2a neurons. While the populations under study here are quite specific, it contains a parable for all stem cell biologists, giving a discrete example of how the choice of protocol to get to a desired cell type can change the cell in ways that might not be captured using a handful of marker genes.

Chapter 4 contains a pivot in the direction of cell engineering. In this chapter I explore the ways that neurons are derived from stem cells, contrast existing methods, and propose ways that existing genetic tools and methods could be leveraged to make robust populations of neurons or glia for use in disease modeling and drug screening. Lastly, Chapter 5 contains some unfiltered reflection on the experiments described in Chapters 2-4 and proposes future avenues of study.

CHAPTER 2

Axial elongation of caudalized human organoids mimics aspects of neural tube development

Introduction

The development of multicellular organisms depends on the organized emergence of tissues and organs, which in turn relies on the specialization and regionalization of numerous cell types. In human spinal cord development, multiple neural subtypes that are crucial to motor control arise from distinct progenitor domains in the developing neural tube (Tanabe and Jessell, 1996). The neural tube itself arises in tandem with the initial establishment of the anterior-posterior embryonic axis in a process known as axial elongation (Steventon et al., 2016). Defects in early neural tube morphogenesis result in severe congenital abnormalities, such as spina bifida. Furthermore, defects in spinal interneuron development can ultimately impact motor control and locomotion (Azim et al., 2014; Zhong et al., 2010; Crone et al., 2008), highlighting the clinical importance of understanding human axial elongation and neural tube development. However, despite the advances gleaned from vertebrate models such as mouse and chicken, many of the molecular mechanisms and cellular behaviors that regulate spinal cord development in humans remain unknown due to the difficulty of studying these dynamic post-implantation processes.

Advances over the past decade have demonstrated that, unlike anterior neural populations, the posterior neural tube is partially generated from a unique pool of axial stem cells called neuromesodermal progenitors (NMPs) (Henrique et al., 2015). NMPs are bipotent progenitors that reside at the node-streak border within the caudal lateral epiblast and later in the chordoneural hinge of the tail bud (Wilson et al., 2009; Cambray and Wilson, 2002; Wymeersch et al., 2016; Beddington and Robertson, 1999). The lack of a model for human posterior neural tube development has hindered our understanding of how NMPs regulate and coordinate the emergence of the posterior spinal cord. However, studies in model systems and 2D differentiation models implicate Wnt and FGF as crucial posteriorizing factors that regulate this process (Briscoe and Ericson, 1999; Ericson et al., 1997; Liem et al., 1995; Diez del Corral and Storey, 2004)

Differentiation protocols based on embryonic development have enabled the robust production of neuronal subtypes *in vitro* (Butts et al., 2017; Wichterle et al., 2002; Li et al., 2005; Meinhardt et al., 2014). In parallel, high-throughput organoid platforms have been developed that are capable of recapitulating structures reminiscent of early embryonic tissues (Lancaster and Knoblich, 2014). More specifically, protocols have capitalized on NMP differentiation (Gouti et al., 2014) to generate neuromuscular junctions (Faustino Martins et al., 2020), mimic spinal cord dorsal-ventral patterning (Zheng et al., 2019), or recapitulate the complex spatiotemporal expression profiles of gastrulation (in structures termed ‘gastruloids’) (Beccari et al., 2018; van den Brink, 2020; Moris et al., 2020; Veenvliet et al., 2020). However, existing organoid models do not perfectly recapitulate the spatiotemporal dynamics of gene expression and differentiation that occur within embryos. Moreover, reproducibility within differentiations, between cell lines and experiments, and across labs remain a significant technical hurdle that has hindered widespread organoid adoption (Ortmann and Vallier, 2017). Despite these limitations, *in vitro* models offer the opportunity to deconvolve embryonic signaling pathways in ways that are not possible in a complex *in vivo* system, highlighting the complementary benefit of organoids relative to embryo-based research.

Expanding on the foundation of established ‘gastruloid’ models and our group's experience with hindbrain interneuron models (Butts et al., 2017), we have developed a human organoid model that recapitulates key morphological processes that generate axial elongation during human spinal cord development in a reproducible manner across multiple human induced and embryonic stem cell lines (i.e. hiPSCs and hESCs). These organoids demonstrate extensive self-driven unidirectional axial elongation, cell specification of NMP differentiation and neural tube morphogenesis, and regionalized gene expression profiles with distinct caudal identities. This robust model of neural tube morphogenesis and axial elongation enables direct examination of previously inaccessible aspects of early human spinal cord development and patterning.

Results

Wnt agonism induces axial extension of neuronal organoids

Exogenous canonical Wnt signaling induces morphogenesis resembling axial elongation in *in vitro* models of early gastrulation (Moris et al., 2020), where caudalization is crucially dependent on Wnt signaling (Wilson et al., 2009; Henrique et al., 2015; Yamaguchi, 2001). Therefore, to obtain a population of caudalized spinal neuron progenitors, we elaborated on a previously described 2D hindbrain interneuron differentiation protocol (Butts et al., 2017) that starts with promoting differentiation to the neuronal lineage by treating human PSCs with the small molecules SB43542 and LDN193189, which inhibit the TGFβ and BMP pathways, respectively (a process defined as dual SMAD inhibition). Small-molecule inhibition of these two pathways has been widely used to generate cranial (Shi et al., 2012; Chambers et al., 2009) and hindbrain (Butts et al., 2017) neuronal populations by mimicking the effects of morphogen gradients and their inhibitors within the embryo. *In vivo*, spinal progenitors emerge from regions of the epiblast exposed to high levels of Wnt/β-catenin signaling. Therefore, to generate a caudal neuronal population, we hypothesized that we would need to caudalize the progenitor population prior to neural commitment. We subsequently modified the original protocol by treating WTC-11 human induced pluripotent stem cells (hiPSCs) with 2 μM of the Wnt small-molecule agonist CHIR99021 (CHIR) starting 2 days prior to neuronal differentiation

(**Fig. 2.1A,B**). CHIR treatment was initiated in mTeSR1 medium, which contains both FGF and activin (TGFβ) to keep hPSCs in a self-rrenewing pluripotent state (Ludwig et al., 2006). However, the introduction of CHIR to mTeSR1 medium results in morphogen milieu that mimics the signaling environment of the gastrulating embryo. The combination of Wnt agonism with FGF and activin allows for the emergence of neuromesodermal lineages and is crucial to the generation of spinal cord neurons and caudalization within the embryo anterior-posterior axis (Wilson et al., 2009; Henrique et al., 2015). Subsequently, in order to allow for 3D morphogenesis to occur, we generated 3D organoids by aggregating dissociated, single cells pretreated with CHIR in non-adherent pyramidal inverted wells (3000 cells/well) and culturing the organoids in bulk rotary suspension (Hookway et al., 2016) (at about 270 aggregates per well) or in static cultures of single aggregates. Aggregation was considered the start of differentiation (day 0), and CHIR treatment continued through day 7 mimicking the continued presence of Wnt signaling in the posterior of the embryo (Wilson et al., 2009; Yamaguchi, 2001) (**Fig. 2.1A**). At day 5, aggregates were transitioned from the mTeSR media+CHIR+dual SMAD inhibition to a neural maturation media (Butts et al., 2017; Amoroso et al., 2013) to facilitate the differentiation and maturation of caudal neural progenitors generated in the first 5 days of the differentiation. Finally, as retinoic acid and sonic hedgehog signaling are crucial for neuronal development and maturation (Briscoe and Ericson, 1999; Kim et al., 2009; Okada et al., 2004), both retinoic acid (RA) and the sonic hedgehog agonist purmorphamine (Pur) were added to the culture to facilitate the emergence of caudalized cell fates and limit the emergence of sensory dorsal neurons. After 5 days in suspension culture, some, but not all, of the CHIR-pretreated organoids displayed pronounced singular extensions (**Fig. 2.1C**). Notably, extension occurred both in bulk rotary cultures and in static cultures of single aggregates in non-adherent 96 wells, confirming elongated organoids formed through extension rather than fusion of multiple aggregates. To quantify the occurrence of elongations, we defined three categories of aggregates – non-elongating (N), partially elongating (P) and elongating (E) – based on the ratio of their long to short axes (**Fig. 2.1D,E**). Using this classification system, over 50% of aggregates were elongating at day 7 of culture in both bulk and single organoid culture formats. Elongated organoids were continuous, with single tissue protrusions extending outwardly from individual radially symmetric aggregates. Histological analysis revealed multiple internal, elongated epithelial compartments within the protrusions separated by regions devoid of cells (**Fig. 2.1C**). Interestingly, extensions occurred in organoids of various sizes (**Fig. 2.3A**) and organoids extended more robustly when cultured at low density (**Fig. 2.3B**), suggesting that density-mediated signaling parameters, such as paracrine effects or nutrient availability, modulate the induction and maintenance of axial extensions, similar to the documented role of Warburg glycolysis in vertebrate axial elongation (Oginuma et al., 2020, 2017).

Elongating organoids consist of neural and mesodermal cells

To examine cell diversity in extended organoids, we performed single-cell transcriptomics on elongated day 10 organoids induced by 2 μM CHIR. Shared nearest-neighbor computation revealed four clusters at resolution 0.5 (**Fig. 2.2A,B**; **Fig. 2.4A-C**). Neural markers, such as SOX2, were expressed in all clusters (**Fig. 2.2C,E**), but clusters A, B and D had higher expression levels of genes associated with the neural tube (SOX2, IRX3, PAX6 and NEUROG2) and the caudal lateral epiblast (CDX2, NKX1.2 and FGF8) (**Fig. 2.2C,E; Fig. 2.4D**). The highest differentially expressed genes (**Fig. 2.4B,C**) in cluster A were associated with regulation of apoptosis (BAX), neural homeostasis (NPY) and protein regulation (MLEC). Cluster B had multiple upregulated genes involved in tumor metastasis (FABP7, PTTG1 and NMP3), cell division (CDC20, NASP) and FGF signaling (FGF8 and FGFBP3), indicating replicating neural progenitors. Cluster D expressed genes associated with chromatin regulation (HIST1H4C and H1FX) and growth factor response (ZFP36L1), possibly indicating more mature neurons. In contrast, MIXL1, MEOX1, CYP1B1, MEOX2 and PAX3 were almost exclusively expressed in cluster C, indicating that this distinct cluster contained mesodermal cells (**Fig. 2.2C,E**; **Fig. 2.4D**). We did not observe expression of endoderm-specific markers such as SOX17, and only very low expression of FOXA2 and PAX9 in fewer than 1% of cells, indicating that, in contrast to previously reported gastruloid models (Beccari et al., 2018; van den Brink, 2020; Moris et al., 2020; Veenvliet et al., 2020), these elongated organoids consisted entirely of neural and mesodermal cell types. In addition, transcriptomic profiles revealed expression of HOX1-HOX9, demonstrating robust posteriorization (**Fig. 2.2D**). The expression of mesodermal genes in a caudalized spinal cord neuron differentiation led us to investigate whether an NMP population, which is known to give rise to both lineages, was present in our organoids. Through immunofluorescence staining of day 6 sectioned organoids, we identified a small population of SOX2$^+$TBXT$^+$ double-positive cells, a defining characteristic of NMP identity (**Fig. 2.2F**). Overall, these data indicate that elongating organoids contain cell populations that appear to be exclusively associated with mesoderm and neural tube, similar to the caudal lateral epiblast during axial extension and suggestive of an NMP-like origin of posterior neural identity.

To obtain a more nuanced understanding of the caudalization of 2 μM CHIR-pretreated organoids, we examined HOX transcripts marking hindbrain (HOXB1), brachial (HOXC6) and thoracic (HOXB9) regions of the anterior-posterior axis via RNAscope at days 7 and 10 (**Fig. 2.2G**). Although non-elongating CHIR-pretreated organoids expressed both HOXB1 and HOXC6 HOX genes on day 7, their expression was equally distributed radially, and the expression of HOXB9 was not detected until day 10. By contrast, HOX expression was regionalized in the elongated organoids by day 7, with HOXB1 (hindbrain) enriched in the central aggregate mass and HOXC6 (brachial) and HOXB9 (thoracic) expressed in the elongated extension. Interestingly, HOXC6 expression was more pronounced at day 7 than at day 10 within elongating organoids, suggesting a transition to a more posterior fate over time (**Fig. 2.2G**). These data indicate that while organoid extension is not a requirement for posterior HOX gene expression, extension enables the stratification of distinct HOX domains.

Wnt signaling influences extension and differentiation across stem cell lines

Because we observed heterogeneity in the length and frequency of organoid elongation, we examined the robustness of Wnt signaling effects on axial elongation *in vitro* across multiple human stem cell lines of both sexes. We differentiated two hiPSC lines (WTC and WTB) and two hESC lines (H1 and H7) into caudal neural organoids in the presence of varying amounts of CHIR (2 μM, 4 μM, 6 μM). Across a 10-day differentiation, the threshold of CHIR required to reliably generate extensions varied between lines (**Fig. 2.5A**). Whereas the WTC line produced elongations most robustly at a 4 μM dose of CHIR, all other lines tested only began to elongate when the CHIR dose was increased to 6 μM. For each cell line, the critical CHIR dose increased both the frequency of $SOX2^{+}TBXT^{+}$ cells at the start of the differentiation (**Fig. 2.5Ci,Di**) and the degree of extension (**Fig. 2.5B,Cii,Dii**, $n \geq 3$ experiments at each timepoint). Curiously, the WTC line demonstrated an intermediate maximum concentration for CHIR-induced extension, as 6 μM CHIR treatment actually reduced the number extensions (**Fig. 2.5A,C**). Importantly, all cell lines displayed internal epithelialization and cystic formation within extensions at the CHIR concentration that permitted elongation (**Fig. 2.6A**).

To examine differences in cell populations induced by varying Wnt concentrations, we stained sections of WTC organoids treated with 2 μM, 4 μM or 6 μM of CHIR at day 10 of differentiation (**Fig. 2.6B**). Organoids exposed to 2 μM CHIR displayed SOX2 and PAX6 expression throughout the entire organoid, whereas organoids exposed to 4 μM or 6 μM CHIR showed regionalized expression of SOX2 and PAX6, suggesting that, as expected, non-neuronal cells ($SOX2^{-}$ $PAX6^{-}$) emerge in the presence of high Wnt signaling. All organoids displayed N-cadherin and β III-tubulin expression, indicating the emergence of maturing populations of neurons. The H1 ESC line displayed regionalized expression of neural progenitor markers when exposed to 4 μM CHIR, similar to the WTC line (**Fig. 2.6C**). Altogether, the level of Wnt pathway activation that allows for robust emergence of an NMP progenitor pool and organoid extension varied across human iPSC and ESC lines – a commonly reported phenomenon in most differentiation protocols (Ortmann and Vallier, 2017). In all subsequent studies, unless otherwise stated, we used the critical elongation dose of 4 μM CHIR with the WTC cell line that elongated most consistently, and referred to it as a 'high Wnt signaling' condition.

Organoid extension is correlated with NMP presence

Because we hypothesized that the extensions observed in CHIR-treated organoids were due to the presence of a NMP population, we next quantified the correlation between organoid elongation, CHIR treatment and NMP presence. Therefore, cells were exposed to 0 μM or 4 μM CHIR from day −2 through day 7 of differentiation, and examined immediately before and after aggregation (day 0-1), and then through day 5 of differentiation (**Fig. 2.7A,C**). Consistent with previous observations, $SOX2^{+}TBXT^{+}$ cells, which are indicative of NMP-like cells, were present in 4μM CHIR organoids at the time of aggregation (after 2 days of treatment, day 0 of differentiation). In the absence of CHIR treatment, organoids lacked $SOX2^{+}TBXT^{+}$ cells and did not extend. Interestingly, the organoids with 0 μM CHIR treatment developed rosette structures of $SOX2^{+}$ cells that were absent in the 4 μM CHIR-treated organoids (**Fig. 2.7A**). The 4 μM CHIR-treated organoids displayed high levels of TBXT expression at day 1 that then became progressively restricted to polarized crescents by day 3 and eventually to very small pockets of $TBXT^{+}$ cells by day 5. Additionally, the 4 μM CHIR treatment resulted in the emergence of the caudal marker CDX2 throughout aggregates at day 3 but restricted to the extending region by day 5 (**Fig. 2.7B**), indicating both organoid polarization and posteriorization in the presence of high-Wnt signaling. These observations confirm that the presence of NMPs within CHIR-treated organoids precedes and correlates with axial elongation.

At day 7 of differentiation, in most imaged organoids grown in 4 μM CHIR, the $TBXT^{+}$ population formed a streak along the protruding extension and accumulated at the end of the extension (**Fig. 2.8A-C**). The morphological arrangement of this population was reminiscent of primitive streak and notochord *in vivo* models and posterior $TBXT^{+}$ cells in gastruloid models

(Moris et al., 2020; Veenvliet et al., 2020). However, expression of the notochord marker homeobox protein notochord (NOTO) was not detectable by immunofluorescence at day 7 and 10 or in our single-cell RNA-sequencing dataset at day 10 of differentiation. The lack of NOTO expression is likely due to inhibition of TGFβ signaling (via the small molecule SB43542), which is known to influence NOTO expression during the initial neural-biased differentiation protocol (Zhang et al., 2020). In contrast to their distribution in 4 μM CHIR organoids, TBXT$^+$ cells in 2 μM CHIR organoids were sparsely distributed across the surface of the spherical organoid with rare regions of SOX2$^+$TBXT$^+$ co-expression (**Fig. 2.9A**). This observation, combined with the histology at earlier timepoints, suggests that the TBXT$^+$ population starts off stochastically distributed throughout the aggregate and then becomes spatially restricted, suggesting that NMPs specified early in differentiation cluster together post-aggregation in order to coordinate subsequent organoid elongation.

Elongating organoids display proliferating neuroepithelial compartments

To examine the kinetics and diversity of elongating organoids, single organoids from the same starting population were imaged continuously over 48 h, revealing robust elongation from a single point in the presence of 4 μM CHIR. At day 5, over 50% of 4 μM CHIR organoids were partially elongating (P) or elongating (E) (**Fig. 2.10A,B**). Furthermore, the 4 μM CHIR-treated organoids had a higher total area and perimeter by day 5 of the time-course (**Fig. 2.10Biii**; **Fig. 2.11**).

Because of the uni-directional extension of our organoids, we examined whether extensions resulted from localized populations of proliferating cells, similar to what is seen in the developing embryo. To this end, we measured the percentage of actively dividing cells along the long axis of sectioned organoids by EdU incorporation and phospho-histone 3 (pH3) staining on days 6, 7 and 9 of differentiation in 4 μM CHIR (**Fig. 2.10C,D**, $n \geq 4$). A 2 h EdU pulse labeled over 50% of the cells in elongating organoids, and EdU$^+$ cells were observed increasingly at the outer edges of day 6 and 7 elongating aggregates (quadratic model fit, $P<0.001$), with an ~15% increase in EdU labeling from center to edge of the organoids. pH3 staining revealed a similar, though less stark, trend of increased proliferation at organoid edges (1% or less change, quadratic model fit, $P=0.015$). Overall, cell division increased at both ends of the organoid surface, and we did not observe a pole-specific proliferation bias, indicating that cell division alone could not explain uniaxial extension.

To examine epithelial morphology, we stained for collagen IV (COL IV), a marker of the basement membrane, and zona occludens-1 (ZO-1), a marker of tight junctions at cellular apical domains in low CHIR (2 μM) and high CHIR (4 μM) conditions (**Fig. 2.10E**; **Fig. 2.12A**). Basement membrane deposition and apical-basal cell polarization, determined by apical location of tight junctions, was observed within the extension of organoids between days 7 and 10 of differentiation in high CHIR organoids (**Fig. 2.12B**), paralleling the lumen formation by polarized epithelia documented in existing organoid models (Faustino Martins et al., 2020). After 10 days, ZO-1 was apparent at the apical domain of cells in the outer epithelial layers of the extensions, as well as in cells facing the internal lumens. Distinct layers of basement membrane marked by collagen IV were observed basally to ZO1, forming a bilayer between lumens and organoid exterior. This organization occurred in all organoids, although to a lesser extent in low CHIR conditions (**Fig. 2.10E**; **Fig. 2.12A,Bi**). Furthermore, at day 10 of differentiation, these epithelial layers contained cells expressing the neuronal progenitor markers Nestin and β-III-tubulin, indicating that the majority of cells at the surface layers differentiated to a neural fate (**Fig. 2.10F**, **Fig. 2.12Bii**). These patterns of polarized apical basal proteins suggest that elongating organoids undergo tissue polarization via axial extensions that consist of sheets of proliferating neuroepithelial cells with neural tube progenitor identity surrounding organized basement lamina and internal lumens (Martins-Green and Erickson, 1986; O'Shea (1987; Hay and Meier, 1974).

Elongating organoids display developmental ontogeny of gene expression

To investigate the transcriptional differences resulting from Wnt agonism, we compared organoids with 0 μM or 4 μM CHIR treatment via bulk RNA-sequencing at different stages of differentiation. Analysis of the top divergent genes between the 0 μM CHIR (no extensions) and the 4 μM CHIR conditions (**Fig. 2.13A**, **Fig. 2.14**) revealed unique components of pattern specification. At day 1, 4 μM CHIR organoids were enriched for genes involved in pattern specification and embryonic morphogenesis (*WNT5B* and *CDH2*). 4 μM CHIR organoids then progressed through distinct developmental stages, beginning with increased expression of genes involved in gastrulation, such as *TBXT*, eomesodermin (*EOMES*), *NOTO* and goosecoid (*GSC*), which was paired with reduced expression of pluripotency markers such as Nanog. Beginning at day 3, 4 μM CHIR organoids transitioned through a caudal epiblast phenotype characterized by increased expression of caudal genes *CDX2*, *FGF8*, *WNT3A* and *WNT5A*. At this stage, 4 μM CHIR organoids also displayed a reduction in the forebrain marker OTX2, whereas its expression was maintained in 0 μM CHIR organoids, further indicating that the 4 μM CHIR signaling condition promotes the emergence of caudal fates (**Fig. 2.13A**). Finally, starting at day 3 and continuing throughout the rest of the 10 day differentiation, 4 μM CHIR organoids displayed an increase in neuronal markers associated with the developing neural tube (IRX3, NEUROG2, OLIG2, PAX6, SOX1 and SOX2). Overall, this analysis indicates that early stimulation of Wnt signaling induces pattern specification in organoids that mirrors the successive *in vivo* phases of gastrulation, caudal epiblast formation and neural tube development associated with caudal neurogenesis.

We next examined whether the spatial distribution of gene expression was analogous to anterior-posterior patterning in embryonic development. Polarized expression of the posterior marker CDX2 (Beck et al., 1995) was detected at day 5 and day 10 of differentiation in 4 μM CHIR organoids (Fig. 2.13B). By day 10, compartments of cells expressing the ventral spinal cord marker

OLIG2 were observed lining the epithelial cysts of 4 μM CHIR organoids (Fig. 2.13C). Combined with the expression of Nestin and β-III-tubulin at day 10 (Fig. 2.10F), this expression confirms that the later stages of the 4 μM CHIR differentiation shift toward neural fates. Interestingly, at day 10 some 4 μM CHIR organoids displayed clusters of NODAL- and LEFTY-positive cells, and polarized pSMAD1/5 expression was detected along the length of the organoid (Fig. 2.13B; Fig. 2.15A,B), suggesting the presence of an organizer-like population. Interestingly, multiple clusters of NODAL-positive cells were occasionally detected in 4 μM CHIR organoids with multiple extensions (Fig. 2.15A). These observations suggest that the 4 μM CHIR organoids exhibit spatiotemporal gene expression and morphogenic organization analogous to those observed during the establishment of the anterior-posterior axis of the embryo.

In addition to the emergence of genes associated with the caudal epiblast, we also examined the timing and extent of HOX gene expression in 0 μM CHIR (non-elongating) and the 4 μM CHIR (elongating) organoids. 0 μM CHIR organoids began to express detectable anterior HOX transcripts at day 7 and adopted a hindbrain identity after 10 days of differentiation (**Fig. 2.13C**). In contrast, 4 μM CHIR organoids expressed both hindbrain and cervical HOX transcripts as early as day 3, with a notable upregulation in thoracic HOX genes by day 10. This temporal change in HOX gene expression suggests that the onset of HOX gene expression in 4 μM CHIR organoids mimics aspects of the progression of anterior-to-posterior elongation of *in vivo* embryonic development.

Brachyury is required for the formation of singular extensions

In vivo, Wnt signaling directly upregulates the expression of the transcription factor TBXT, which in turn mediates both Wnt and FGF posterior-to-anterior gradients (Amin et al., 2016). The importance of TBXT for proper axial elongation has been demonstrated in mouse knockout models, which have severely disrupted trunk morphogenesis and fail to generate the notochord and posterior somites (Amin et al., 2016; Pennimpede et al., 2012; Wilson and Beddington, 1997; Wilson et al., 1993; Chesley, 1935; Guibentif et al., 2021). Thus, we interrogated the role of

TBXT in axial elongation in our organoids, using an inducible CRISPR interference (CRISPRi) system in human iPSCs to knock down TBXT expression (Larson et al., 2013).

First, we integrated RNA guides targeting TBXT into a Lamin-B::GFP WTC hiPSC line harboring a doxycycline (DOX)-inducible CRISPRi system (Libby et al., 2018; Mandegar et al., 2016). DOX induction for 5 days prior to cell aggregation (day 0) reduced the number of TBXT transcripts by 90% (**Fig. 2.16A,B**) and significantly reduced the frequency of $TBXT^+SOX2^+$ cells (**Fig. 2.16C**). Interestingly, by day 5 of differentiation under 4 μM CHIR conditions, the TBXT knockdown (TBXT KD) organoids displayed multiple protrusions rather than coordinated singular extensions (**Fig. 2.16D**). Histology revealed folded layers of epithelial sheets, indicating that increased epithelial tissue formation rather than coordinated morphogenesis was the likely cause of the multiple protrusions in the TBXT KD organoids (**Fig. 2.16E**). To quantify these folds, each organoid was segmented (**Fig. 2.16Fi**) and the number of convex indentations from the perimeter of each organoid was quantified (**Fig. 2.16ii**, arrows). This analysis showed that the TBXT KD organoids had an increased percentage of convex defects compared with the wild-type organoids, diverging as early as day 4 of the differentiation with the highest number of defects apparent at day 7 (*n*>14 per timepoint). The TBXT KD organoids also lost spherical morphology 2 days before wild-type organoids started extending (**Fig. 2.13Fiii**) and reduced levels of TBXT expression were maintained in KD organoids through day 10 (**Fig. 2.16G,H**). Interestingly, the KD organoids maintained a small proportion of $TBXT^+$ cells that escaped knockdown, but not enough to trigger elongation, suggesting a threshold of $TBXT^+$ cells is required for coordinated elongation. TBXT KD organoids and isogenic (non-silenced) controls expressed the neuronal marker Nestin, the caudal marker CDX2 and extracellular matrix protein fibronectin (Fb) (**Fig. 2.17**). However, there was a reduction in caudal HOX genes in the TBXT KD organoids at days 5 and 10 of differentiation, as well as a reduction in CDX2 and FGF8 expression (**Fig. 2.16I**), which are both highly expressed in the caudal lateral epiblast and reduced in TBXT knockout mice (Amin et al., 2016; Pennimpede et al., 2012). Interestingly, organoids maintained expression of Wnt signaling molecules, such as AXIN2 and WNT3, even after the termination of CHIR-induced Wnt agonism, suggesting that TBXT is necessary for unidirectional extension and caudal fate specification in organoids, but not essential for endogenous Wnt expression and signaling.

Discussion

Here, we have generated an organoid model of neural tube formation that mimics several aspects of early spinal cord development, including axial elongation, the maintenance of a population of SOX2$^+$TBXT$^+$ NMPs, and the generation of neural tube-like neuroepithelial cells. This model is based on aggregates of hPSCs that undergo robust unidirectional axial extension when exposed to a critical dose of Wnt signaling. In organoids that were exposed to the Wnt agonist, CHIR, the number of TBXT$^+$SOX2$^+$ NMP-like cells increased proportionally to CHIR dose as well as the presence of both mesoderm and neurectoderm during elongation of the organoid, similar to the embryonic body axis (Wymeersch et al., 2021). Single-cell RNA sequencing of elongating organoids confirmed the presence of caudal cell phenotypes, in addition to neural progenitors and paraxial mesoderm populations. Elongating organoids displayed anterior-posterior patterning and a more posterior HOX gene profile than non-elongating organoids in equivalent culture conditions. Finally, NMP generation, coordinated axial elongation and adoption of a caudal identity were all abrogated in organoids with TBXT silenced (Pennimpede et al., 2012; Guibentif et al., 2021). Overall, these elongating organoids provide a significant step towards reliable *in vitro* models that can be used to further interrogate the gene regulatory networks that contribute to morphogenetic elongation, the multicellular morphogenesis involved in extension organization, and the stratification of anterior and posterior populations that contribute to the development of the central nervous system in humans.

In this model, elongating organoids often developed multiple internal epithelial compartments rather than a single cohesive neural tube. We hypothesize that this multi-tube-like morphology is due to the absence of surrounding tissue(s) that are present *in vivo* and likely regulate proper neural tube formation via a combination of mechanical and biochemical cues. In support of this hypothesis, mis-regulated Wnt signaling has been shown to generate excessive neural tubes at the expense of mesoderm (Chapman and Papaioannou, 1998; Takemoto et al., 2011; Shum et al., 1999). The exogenous addition of the ventralizing sonic hedgehog agonist, purmorphamine, to the culture was carried out intentionally to limit the generation of sensory dorsal neural progenitors, but purmorphamine might also disrupt the ability of the organoid to form a single neural tube (Murdoch and Copp, 2010). Furthermore, the elongating spinal cord is physically situated between multiple tissues (gut, lateral plate mesoderm, etc.) that present different local tissue mechanics (Zhou et al., 2009), which may also contribute to the morphogenesis of a single neural tube. Finally, recent reports in chick have described the fusion of multiple lumens into a single neural tube during secondary neurulation, when the most caudal region of the embryo is formed (Gonzalez-Gobartt et al., 2021). Thus, it is possible that human PSC-derived elongating organoids emulate early stages of a similar lumen fusion process to form a single neural tube.

An important element of axial elongation is the progressive activation of HOX gene clusters both spatially and temporally. Although our elongating system recapitulates some of this pattern and initiates expression of relatively posterior HOX profiles, we did observe day-to-day fluctuations in HOX gene expression via bulk sequencing. Wnt and FGF signaling have been shown to specify brachial and thoracic HOX identity by upregulating expression of the transcription factor CDX2, which allows for HOX1-HOX9 expression, forming a posterior axial identity (Mazzoni et al., 2013; Metzis et al., 2018; van den Akker et al., 2002) In our system, high expression of FGF17, WNT5B and CDX2 were observed starting at day 1 through day 3 in the 4uM CHIR treated organoids, consistent with early expression of HOX genes (**Fig. 2.10**). However, HOX expression was then generally reduced at days 5 and 7 before increasing again at day 10. There could be several explanations for this phenomenon. As the gene expression is averaged across the entire tissue, bulk sequencing may not provide sufficient resolution to identify clear trends in expression, particularly as organoids grow and generate a greater diversity of more complex cell types. Additionally, recent studies have shown that the temporal regulation of HOX genes can be influenced by tissue culture conditions (Mouilleau et al., 2021). In particular, the regulation of FGF, RA and Wnt signaling influence HOX gene emergence, which may in part be the reason that fluctuations in HOX gene expression are observed as the organoids elongate over the course of differentiation. For example, high FGF signaling and Wnt agonism in stem cell media with CHIR early on (days −2 to 5) is transitioned to neural induction media that lacks those factors and is supplemented with RA from days 7 to 10. Even so, the induction of posterior HOX genes demonstrates caudalization of an *in vitro* model of neural development and is an important bridge for studying human neural tube formation.

Various *in vitro* techniques, from micropatterns to Matrigel embedding, have been shown to impact TBXT expression and tissue organization (Sagy et al., 2019; Blin et al., 2018; Muncie et al., 2020). In our organoids, reduction in TBXT expression resulted in loss of posterior HOX gene expression and uncoordinated folding of tissue, reminiscent of the loss of posterior somite formation in murine models. The appearance of multiple protrusions in the TBXT knockdown organoids likely reflects an excess of anterior neural tissue at the expense of NMPs and mesoderm. The confined spherical expansion of a proliferating neuroepithelial sheet would result in epithelial sheet buckling (Nelson et al., 2011; Trushko et al., 2020; Murisic et al., 2015) and the appearance of multiple protrusions. In particular, the proliferation analysis in the wild-type organoids showed actively dividing epithelial sheets in extending organoids (**Fig. 26C,D**); therefore, it is possible that the reduction of TBXT$^+$ cells in the TBXT KD organoids results in a loss of an organizer to drive polarized extension, leaving only epithelial proliferation that mechanically would result in tissue buckling. Another hypothesis is that TBXT expression is necessary for the coalescence of an organizer-like domain from the initial Wnt-stimulated population. Reduced levels of TBXT in the KD organoids would therefore cause tissue polarity to be lost, resulting in multiple asynchronous protrusions.

Overall, this work contributes to the growing body of knowledge showing that stem cell-derived organoid models that reflect multiple organ systems (Lancaster and Knoblich, 2014; Murisic et al., 2015; Lindborg et al., 2016) and stages of development (Faustino Martins et al., 2020; Zheng et al., 2019; Beccari et al., 2018; Eiraku et al., 2011; Broutier et al., 2016) can be used to investigate aspects of human embryogenesis that were previously elusive due to poor tissue quality, technical difficulties isolating and imaging embryonic tissues, and ethical concerns regarding tissue procurement. Although all organoids are imperfect models of embryogenesis, they are highly amenable to variations in culture conditions (Lindborg et al., 2016; Eiraku et al., 2011; Lancaster et al., 2013), to genetic modification (Broutier et al., 2016; Fujii et al., 2015) or to small-molecule drug screens (Zhou et al., 2017; Marikawa et al., 2020), enabling the systematic manipulation of experimental conditions on a larger scale and at a higher throughput than is possible in model organisms. As such, the organoid model described in this report enables future scientific inquiry that can address its current limitations. For example, this system can be used to interrogate the multicellular organization events underlying tissue extension decoupled from the influences of surrounding tissues that would be present in an embryo. The system can be adapted further to identify conditions that allow for the generation of a single continuous neural tube, which has yet to be shown in a human organoid model (Moris et al., 2020; Marikawa et al., 2020) but has been in murine gastruloids (Veenvliet et al., 2020) *in vitro*. Furthermore, although an anterior-posterior axis is clearly developed in our human elongated neural organoids, the emergence of a well-defined dorsal-ventral axis remains elusive, allowing for future elucidation of the independent and interdependent mechanisms that regulate these two axes. Overall, this system advances models of neural tube self-assembly beyond cell signaling toward coordinated multicellular organization and is a facultative stepping point to directly interrogate mechanisms of human morphogenesis and developmental paradigms.

Figures

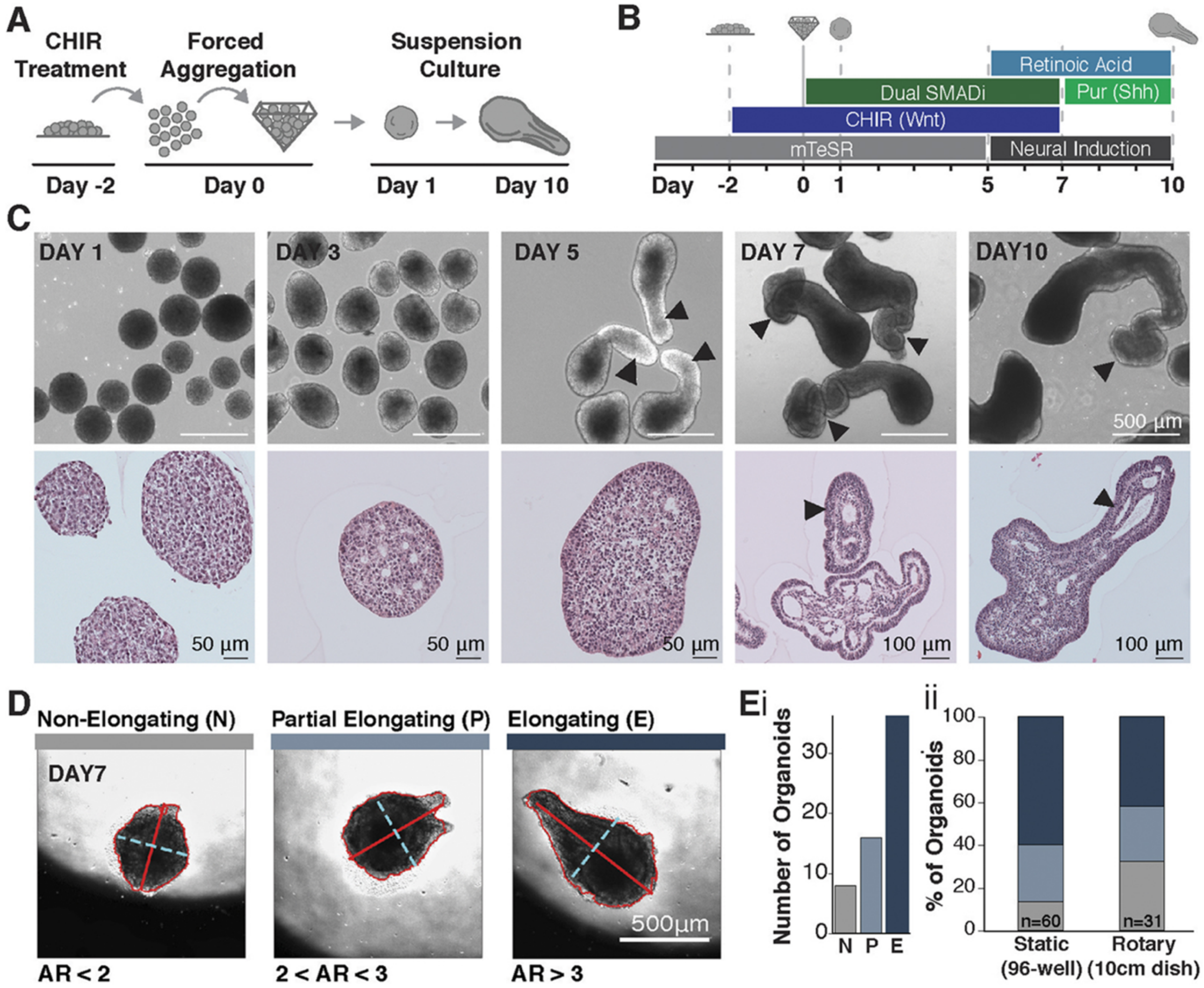

Figure 2.1 CHIR treatment of neural PSC aggregates results in axial extension.
(A,B) Schematic of experimental set-up and differentiation protocol using 2 µM CHIR. (C) Bright-field and histological images of elongating organoids (arrowheads indicate elongated structures). (D) Images from time-course of extension, displaying organoids that do not elongate (N), partially elongate (P) or fully elongate (E) with respective axis ratios (ARs) of AR<2, 2<AR<3 and AR>3 (minor axis dotted cyan line, major axis solid red line). (E,i) Elongation types detected during time lapse imaging (n=60 organoids). (E,ii) Quantification of elongating types across static (n=60 organoids) and rotary (n=31 organoids) cultures.

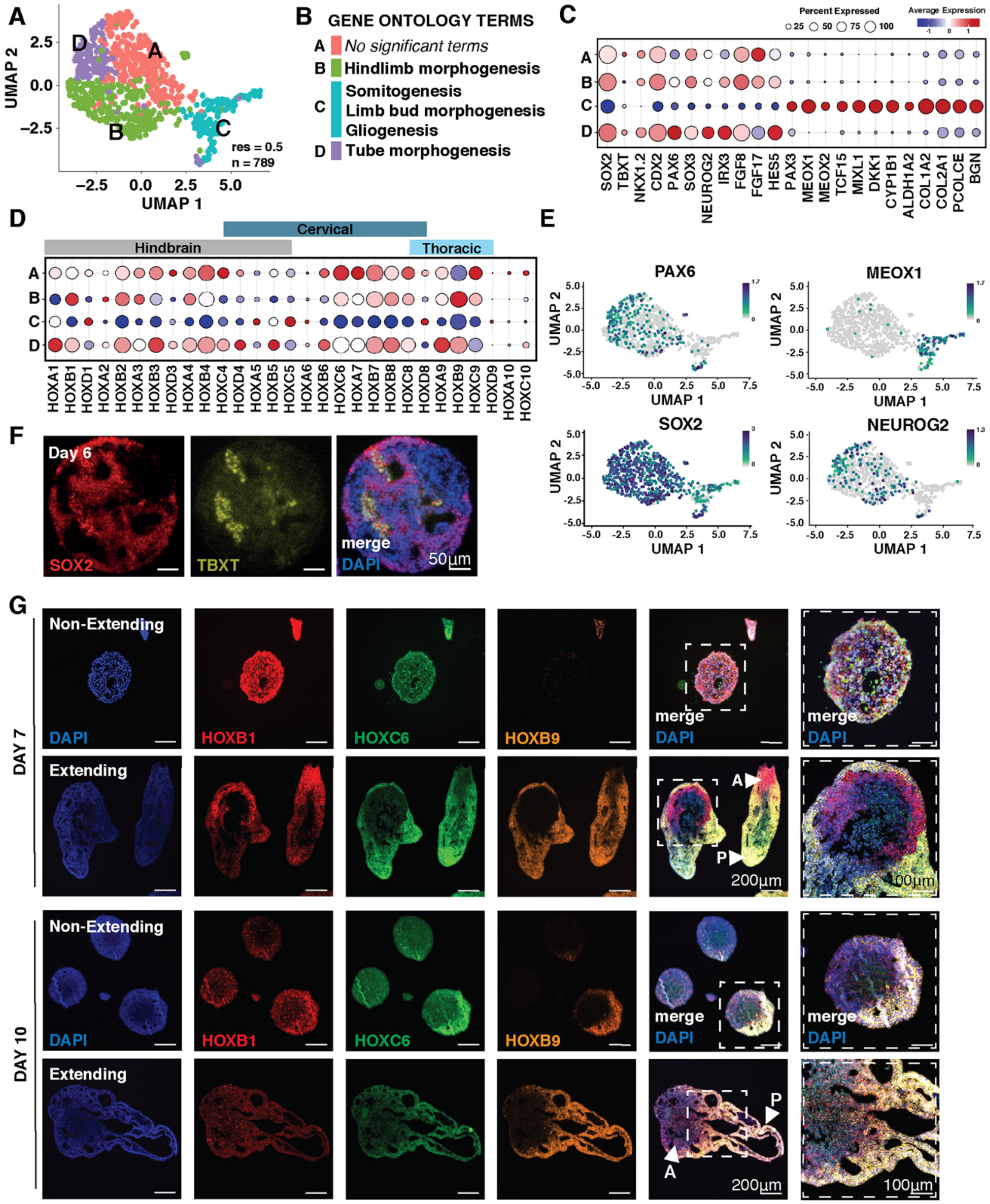

Figure 2.2 Gene expression within elongating organoids.
(A) UMAP of n=789 cells from elongating organoids exposed to CHIR (2 μM) at day 10 of differentiation from single-cell RNA-seq. (B) Significant ($P<0.05$) gene ontology classifications derived from the most differentially upregulated genes in elongating organoids from single-cell RNAseq. Gene ontology terms are assigned to identified clusters. (C) Dot plot displaying genes associated with neural and mesodermal lineages across clusters. (D) Dot-plot displaying HOX gene expression across clusters. (Figure caption continued on the next page.)

(Figure caption continued from the previous page.) (E) UMAPs showing cells expressing PAX6, MEOX1, SOX2 and NEUROG2. Color scale indicates a normalized increase in log2 fold change from min expression to max expression of the respective gene. (F) Immunofluorescence images of organoid paraffin sections stained for SOX2 and TBXT. (G) RNA-scope of sectioned elongating and non-elongating organoids cultured at low density and with 2 μM CHIR with probes for HOX genes marking different regions of the spine at day 7 and day 10 of differentiation [arrowheads mark anterior (A) and posterior (P) ends of organoids]. Scale bars: 200 μm; 100 μm (right-most column).

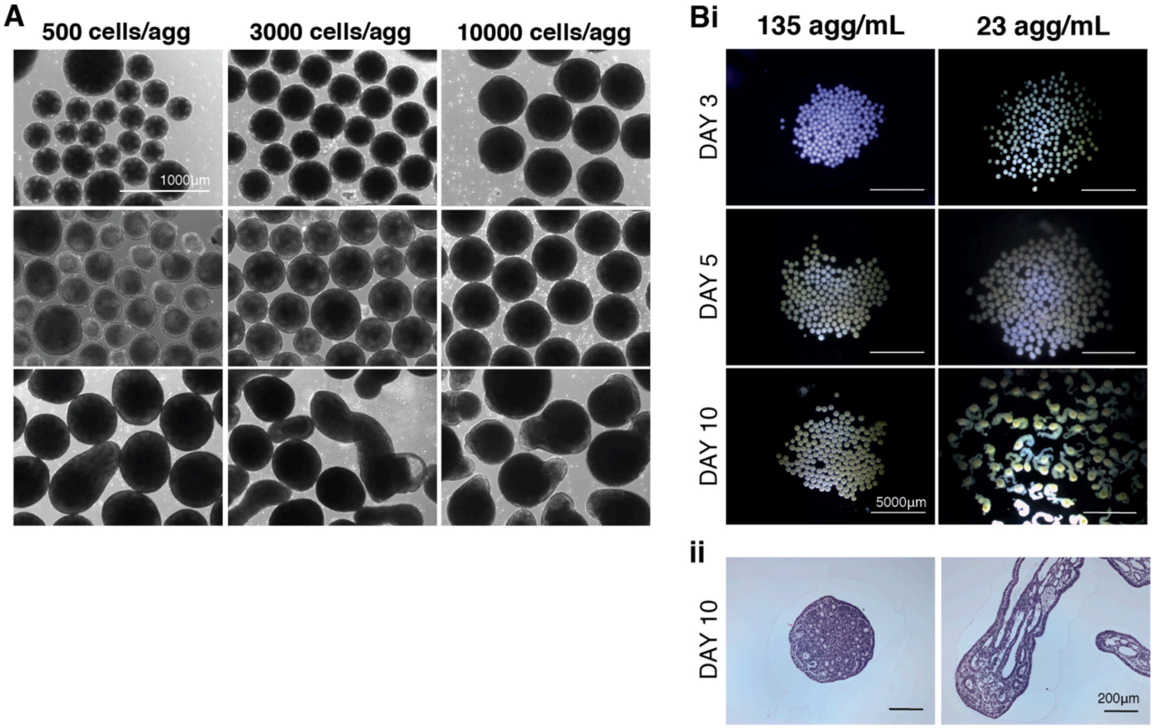

Figure 2.3 Organoid culture density changes morphology of extensions.
(A) Differentiations conducted at 2μM CHIR in the WTC hiPSC line starting with 500 cells/aggregate, 3000 cells/aggregate, or 10,000 cells/aggregate, respectively. Bi) Stereoscope images of 2μM CHIR organoids grown at high (135 aggregates/ml) or low (23 aggregates per ml) densities. ii) Histological stains on paraffin sections of organoids at day 10 of differentiation in high (left) vs low (right) density culture.

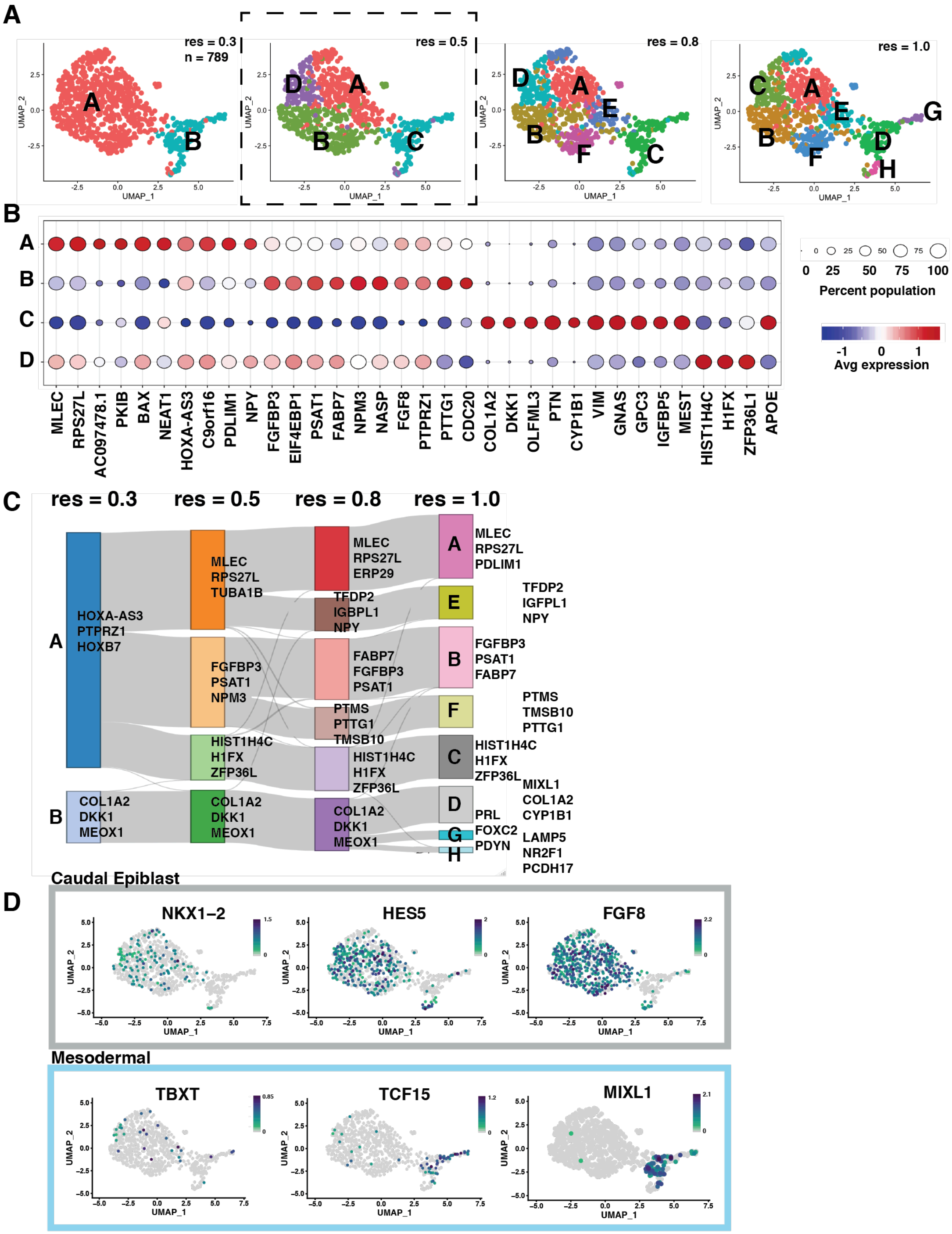

Figure 2.4 Single-cell gene expression within elongating 2µM CHIR organoids. A) Clustering of data set across resolutions. B) Dot plot of top differentially expressed genes at resolution 0.5. C) Sankey plot showing the top 4 expressed gene of every cluster at each tested cluster resolution. D) UMAPs showing cells expressing genes associated with the caudal epiblast or mesodermal lineage. Color scale indicates a normalized increase in log2 fold change from min expression to max expression of the respective gene.

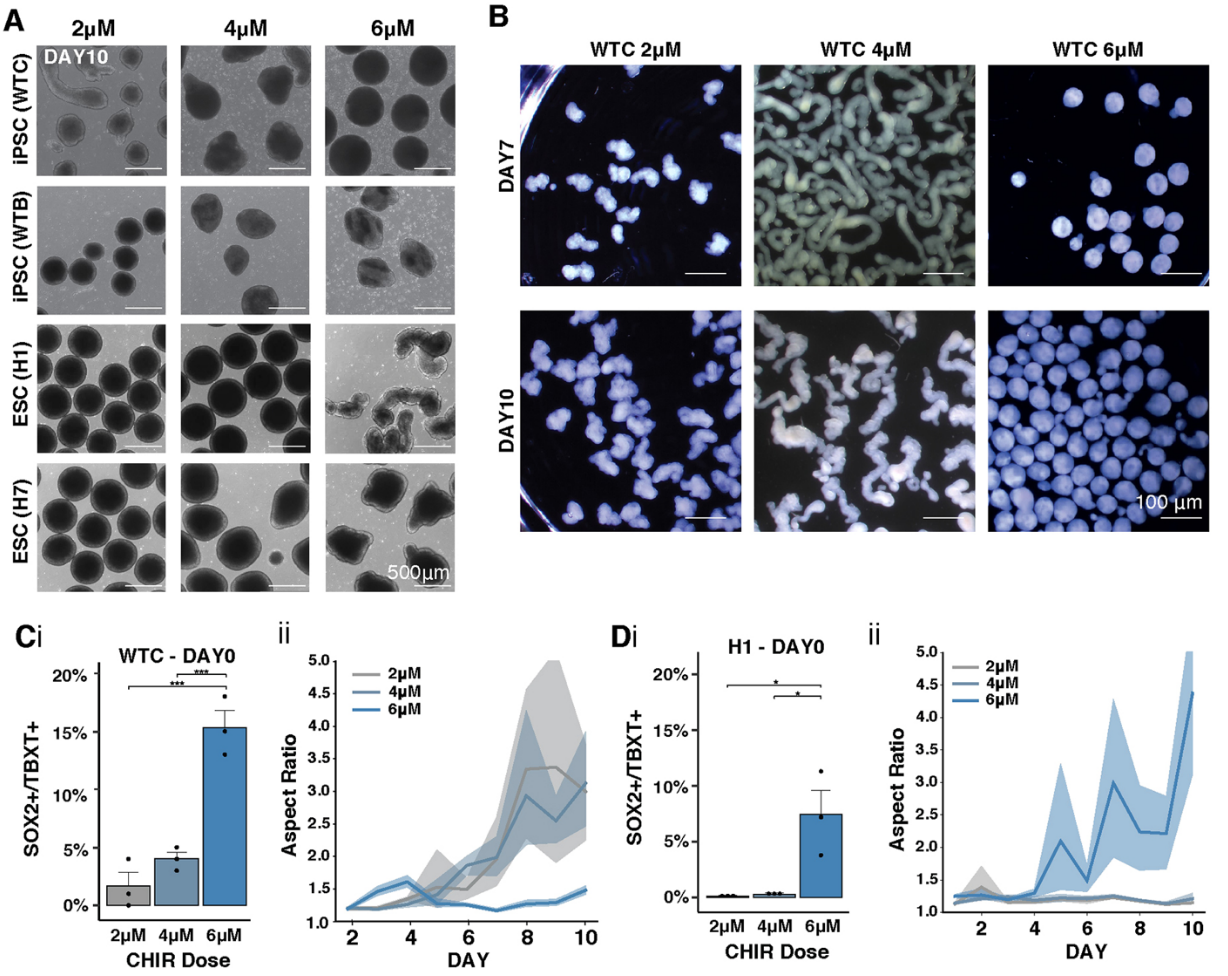

Figure 2.5 Wnt mediates organoid extension across human stem cell lines.
(A) Bright-field images of organoids derived from iPSC and ESC lines at day 7 of differentiation with increased CHIR doses. (B) Stereoscope images of WTC-derived organoids at day 7 or day 10 of differentiation given 2 μM, 4 μM or 6 μM CHIR treatment. (C,D) (i) Quantification of SOX2+TBXT+ cells by flow cytometry in day 0 WTC hiPSCs organoids (C) or H1 ESC organoids (D) as a function of CHIR doses. (ii) Quantification of the length of extensions in WTC (C) and H1 (D) organoids measured as aspect ratio (i.e. major to minor). Solid line indicates mean; shading represents 95% confidence bounds. Student's t-test;*P<0.05 and ***P<0.0005.

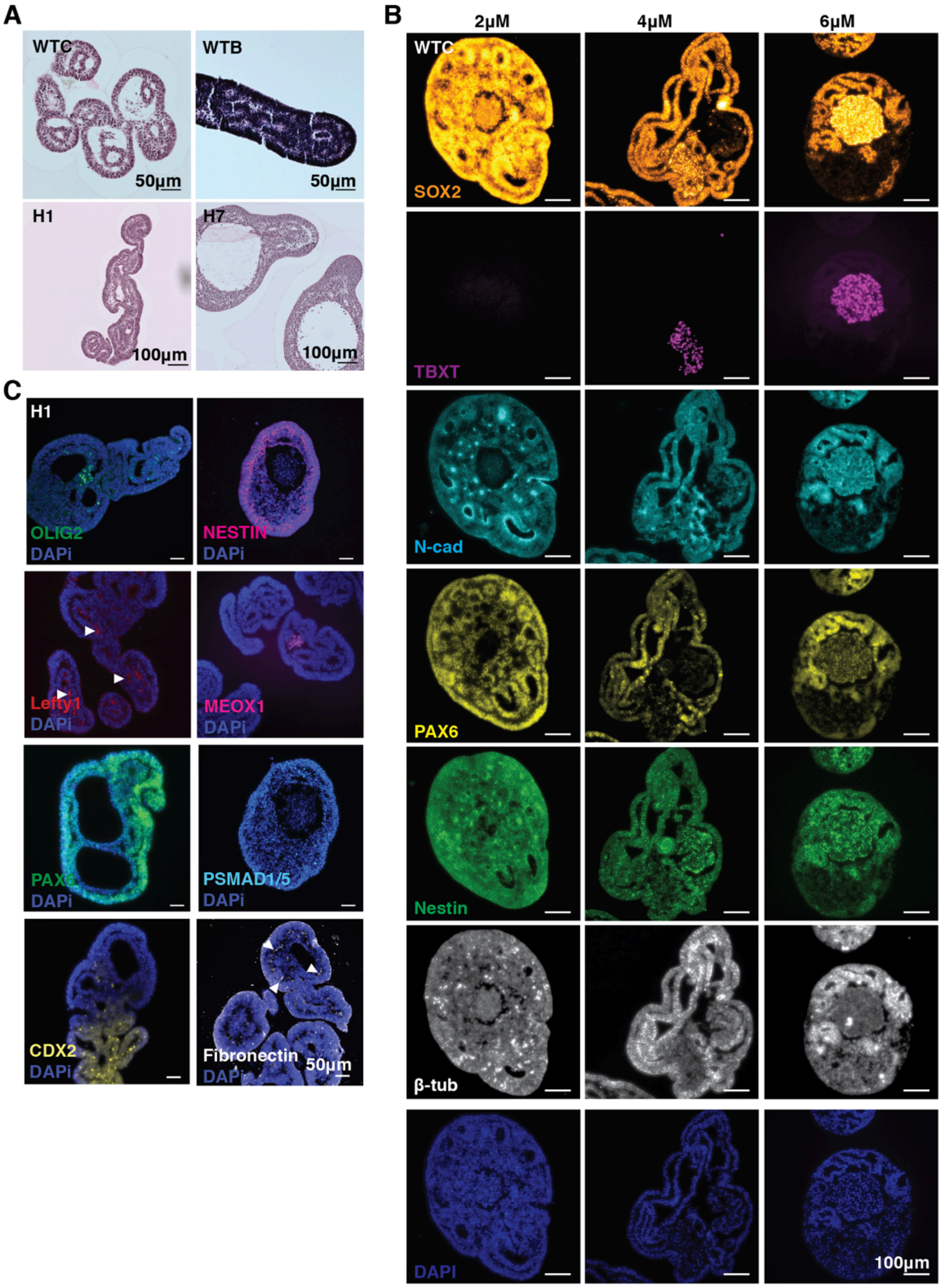

Figure 2.6 Extension reproducibility across hiPSC and hESC lines.
A) Histology of the WTC and WTB hiPSC lines and H1 and H7 ESC lines at elongating CHIR concentrations (4µM, 6µM, 6µM, 6µM: respectively) at day 10 of differentiation. B) Immunofluorescence of paraffin sectioned WTC hiPSC organoids at day 10 of differentiation from 2µM, 4µM, and 6µM CHIR concentrations. C) Immunofluorescence staining of paraffin sections for OLIG2, Nestin, PAX6, pSMAD1/5, LEFTY1, MEOX1, CDX2, and Fibronectin at day 10 in H1 6µM CHIR organoids (arrows indicate regions of positive staining).

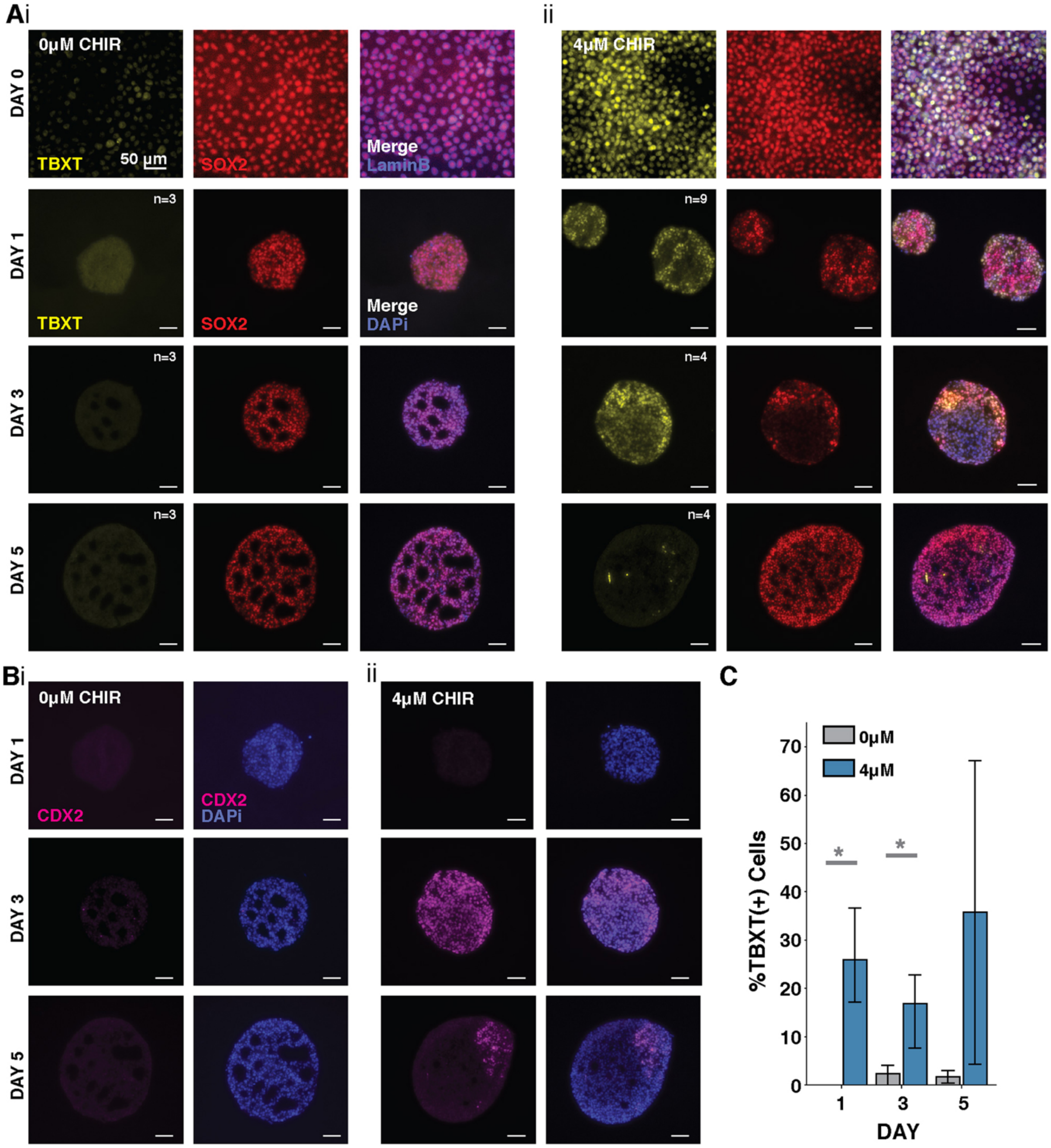

Figure 2.7 Emergence of TBXT, SOX2 and CDX2 over time in 4 μM CHIR organoids. (A) Fluorescence images of histological sections of cultures exposed to (i) 0 μM CHIR and (ii) 4 μM CHIR before and after aggregation showing increases in TBXT+SOX2+ cells with CHIR treatment. (B) Fluorescence images of histological sections of cultures exposed to (i) 0 and (ii) 4 μM CHIR showing CDX2 emergence and localization over time. (C) Quantification of TBXT loss in fluorescence images (n>3 per day, *P=0.04; data are mean ± s.e.m.).

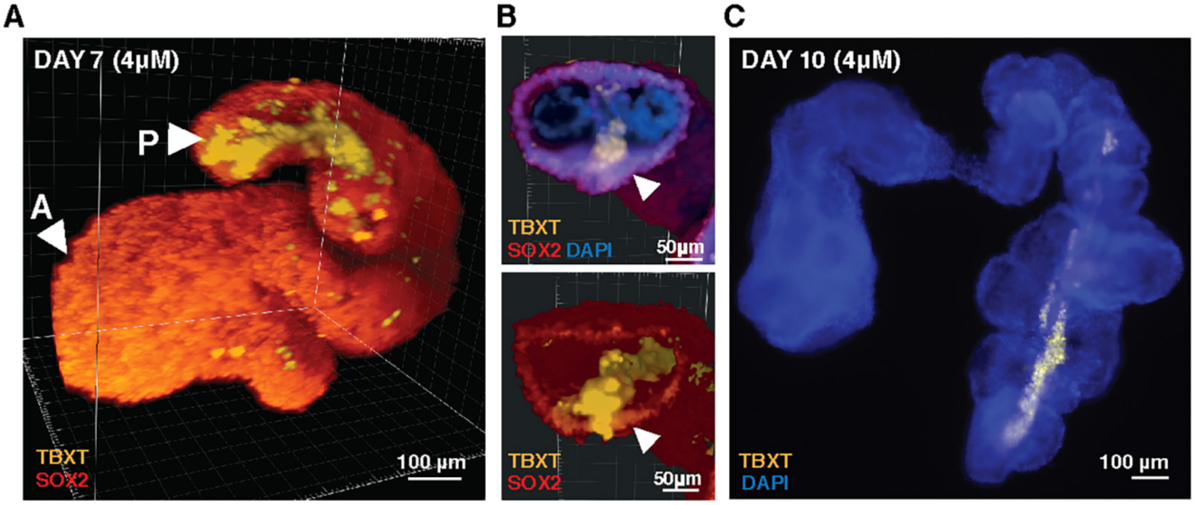

Figure 2.8 TBXT streak in CHIR-treated elongating organoids.
(A) 3D reconstruction based on light sheet fluorescence imaging of a day 7 4 μM elongating organoid showing a streak of TBXT traveling down its length. (B) Cross-section through the 3D reconstruction shown in A displaying a TBXT+ streak and TBXT+SOX2+ cells adjacent to the streak (arrowheads). (C) Fluorescence image of a representative day 10 organoid with a TBXT streak [all aggregates shown cultured in high CHIR condition (4 μM)].

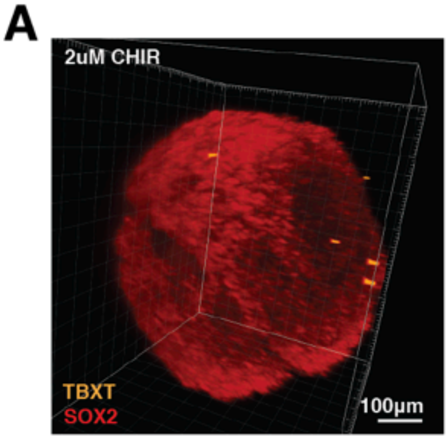

Figure 2.9 TBXT distribution in organoids treated with 2μM CHIR.
3D reconstruction of a light-sheet microscopy image of a day-7 organoid treated with 2μM CHIR stained for TBXT and SOX2.

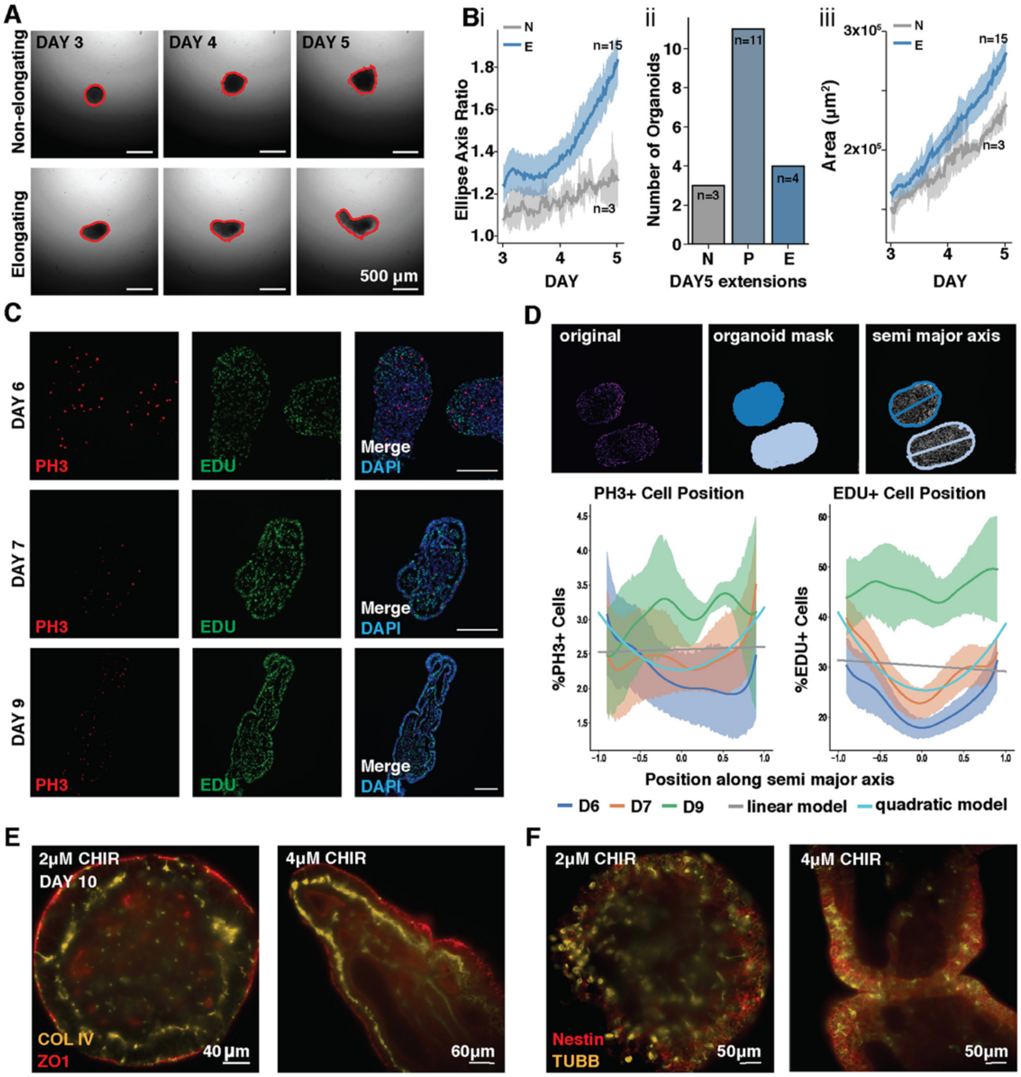

Figure 2.10 Organoids contain proliferative neuroepithelium.
(A) Frames from video time-course tracking the diversity of 4 µM CHIR-treated organoid extensions in static cultures. Red outline defines area measured. (Bi) Quantification of ellipse axis ratios from day 3 to day 5 in 4 µM CHIR organoids labeled as non-elongating (N; grey) or elongating (E; blue). (Bii) Quantification of non-elongating (N), partially elongating (P) and elongating organoids (E) with axis ratios (ARs) of AR<2, 2<AR<3 and AR>3, respectively. (iii) Quantification of the surface area of non-elongating (NE; gray) or elongating (E; blue) organoids treated 4 µM CHIR. Solid lines represent the mean ratio (dark color) with 95% confidence interval (light colored shading); n=18 organoids. (C) Immunofluorescence images of EdU incorporation and phospho-histone 3 (pH3) localization in 4 µM CHIR organoids taken from paraffin sections. (D) Top: segmentation of organoid sections showing pH3 staining (left), segmentation of nuclei by DAPI staining (middle) and a total least squares elliptical fit of the segmentation contour with the major axis superimposed (right). Bottom: line plots for pH3 or EdU expression along the normalized semi-major axis of 4 µM CHIR organoids at day 6, 7 and 9. Linear and quadratic least squares fits of pH3 and EdU expression along the normalized semi-major axis for all days; n>4 independent organoid sections at each timepoint. (E,F) Optical sections from light-sheet microscopy of low CHIR (2 µM) and high CHIR (4 µM) organoids stained for COL IV and ZO1 or Nestin and βIII-Tubulin (TUBB3).

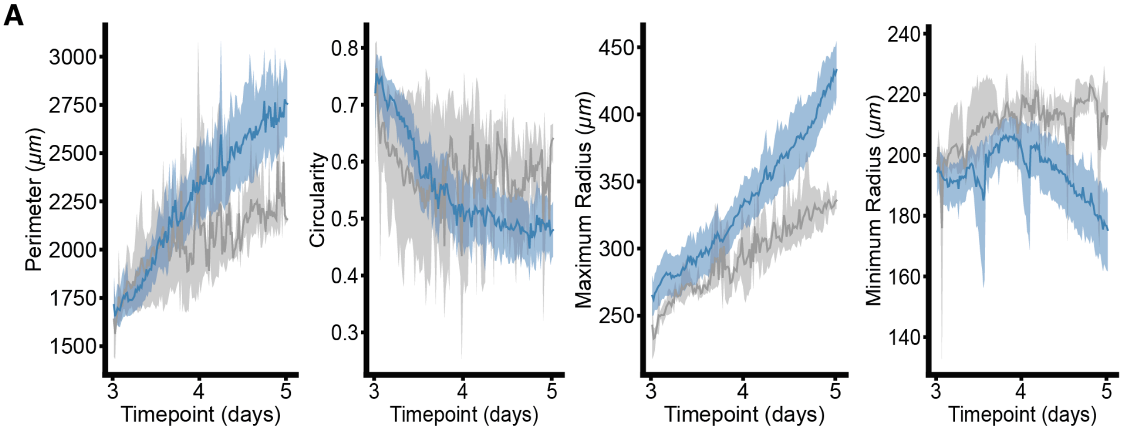

Figure 2.11 Time-lapse imaging of organoid elongation.
A) Quantification of perimeter, circularity, maximum, minimum, and average radius lengths of non-elongating (grey) and elongating (blue) 4μM CHIR organoids. Solid lines represent the mean ratio (dark color) with 95 percent confidence interval (light color); n= 18.

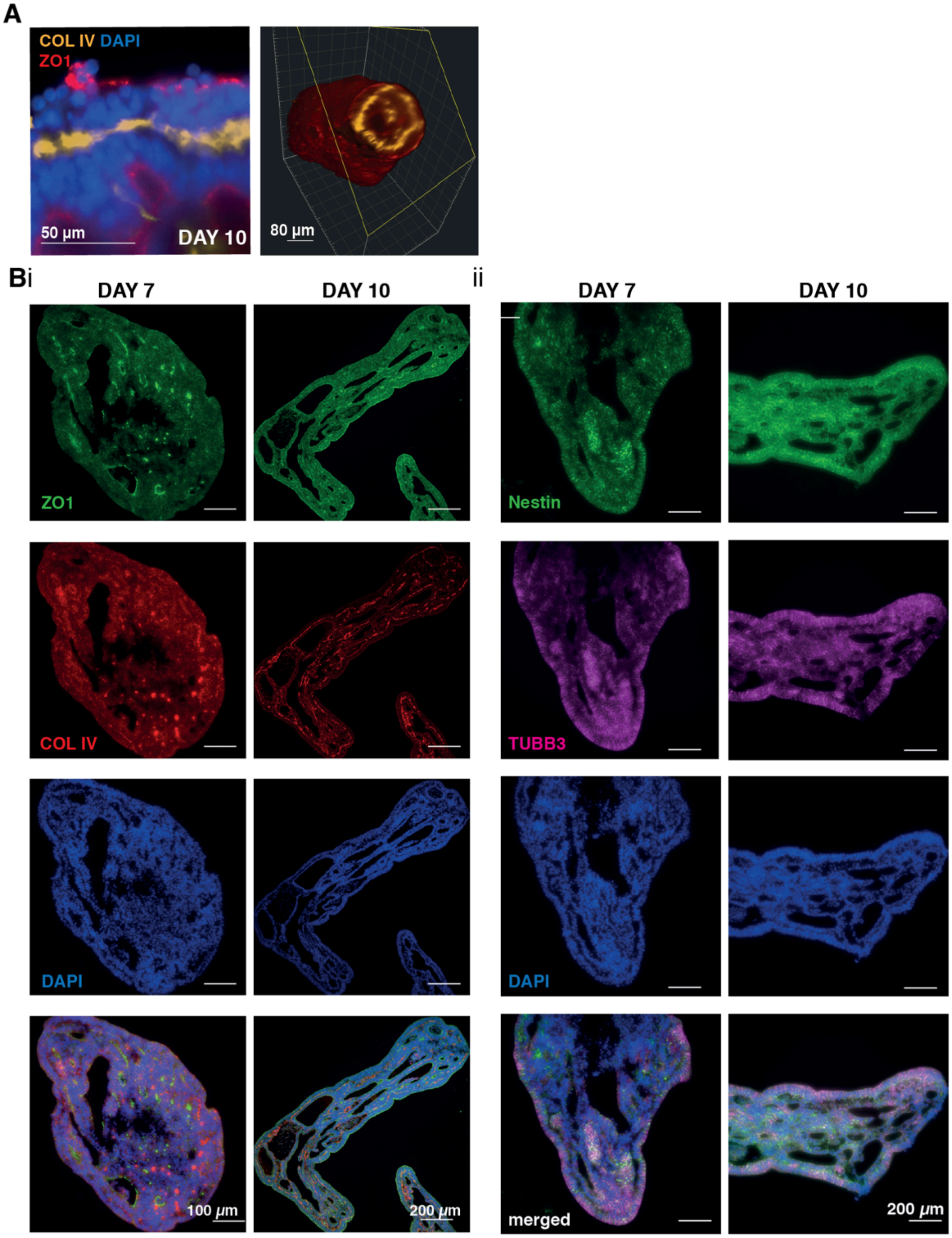

Figure 2.12 Apical-Basal polarity in elongating organoids over time.
A) Optical section from light-sheet imaging of elongating 4µM CHIR organoids stained for COL IV and ZO1 (left) at day 10. 3D reconstruction showing internal ring of basement membrane within the posterior extensions (right). Bi) Immunofluorescence of paraffin sections of 4µM CHIR elongating organoids at day 7 and day 10 of differentiation for markers of basement membrane (COL IV) and tight junctions (ZO1). Bii) Immunostaining of paraffin sections of elongating 4µM CHIR organoids at day 7 and 10 of differentiation for NESTIN and beta-III tubulin (TUBB3).).

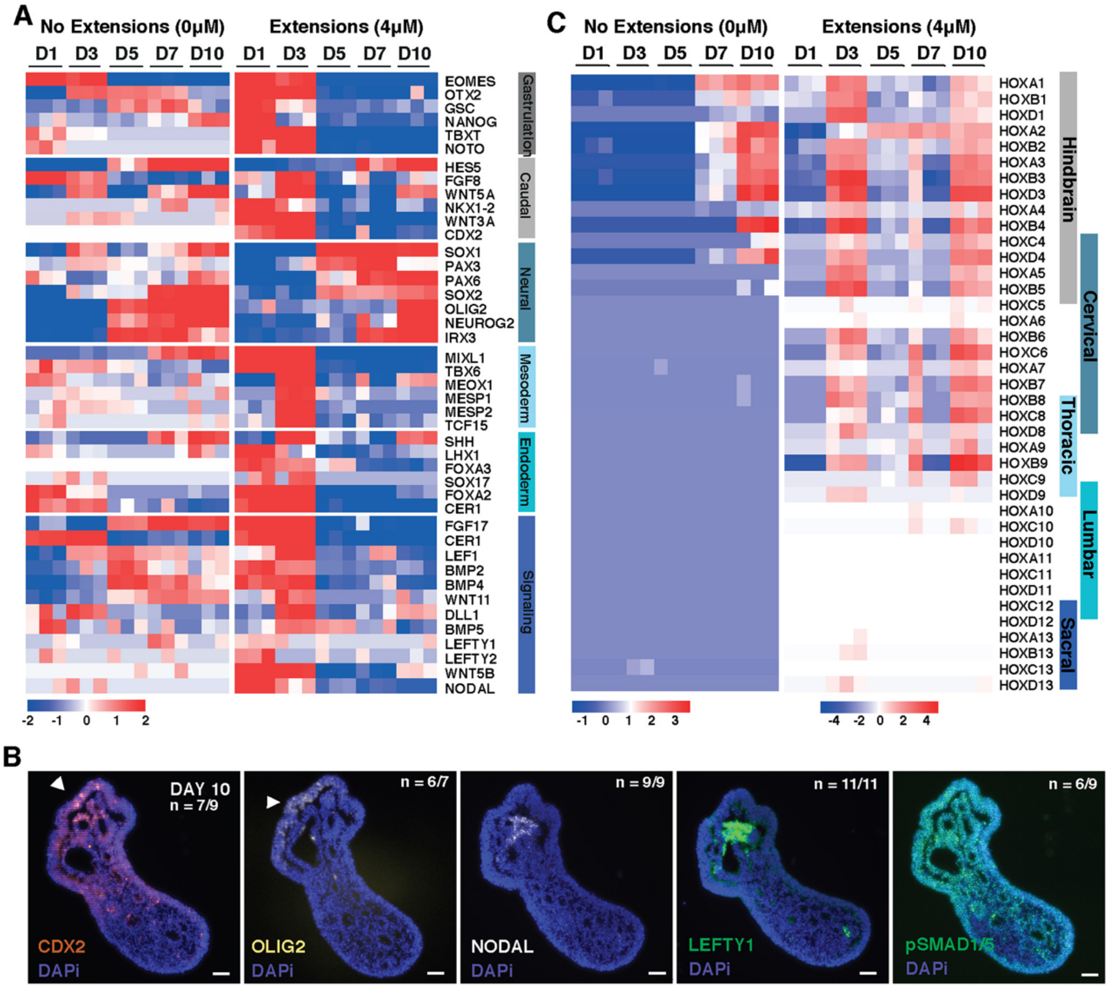

Figure 2.13 CHIR-treated organoids transition through multiple developmental stages. (A) Heat map of gene expression in 0 μM or 4 μM CHIR organoids over time displaying genes associated with gastrulation, caudal epiblast, neuroepithelium, mesoderm, endoderm and major signaling pathways, as determined by bulk RNAseq where the heat map displays the relative expression of a gene compared with the mean expression of all genes across all days. (B) Heat map of HOX gene relative expression compared with the mean expression across days in 0 μM or 4 μM CHIR organoids from bulk RNAseq. Scale bars: 50 μm. (C) Immunofluorescence images at day 10 of differentiation from paraffin sections in 4 μM CHIR organoids examining axis and developmental patterning markers (arrowheads indicate elongating region).

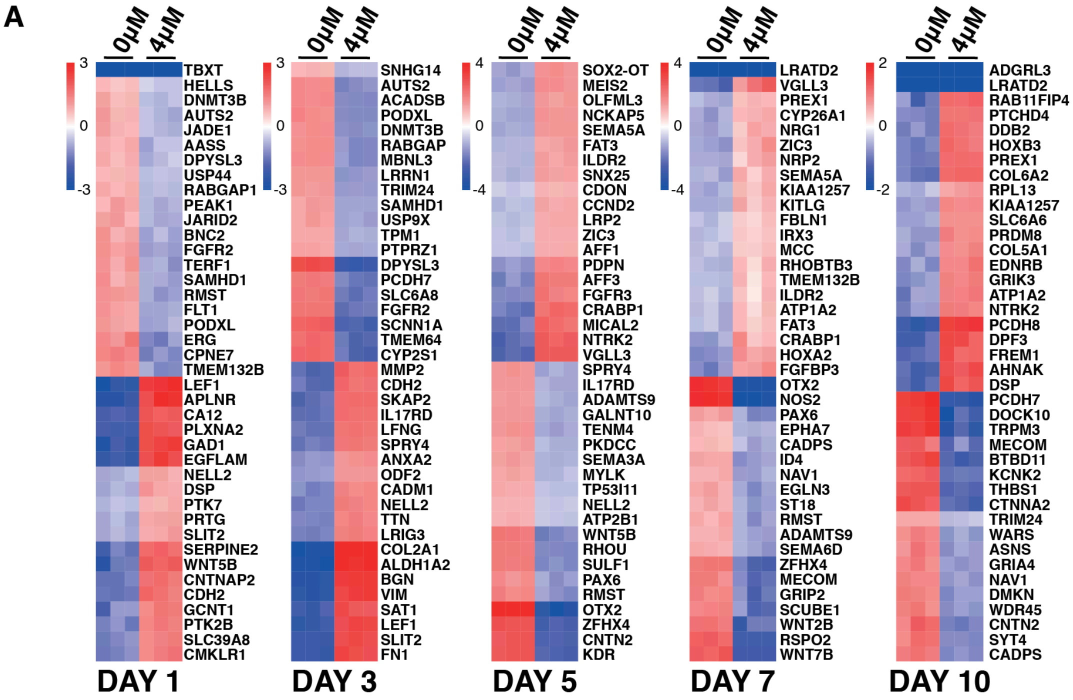

Figure 2.14 Bulk RNA sequencing of organoids with 0μM or 4μM CHIR treatment.
Top differentially expressed genes across time points in organoids treated with 0μM CHIR or 4μM CHIR.

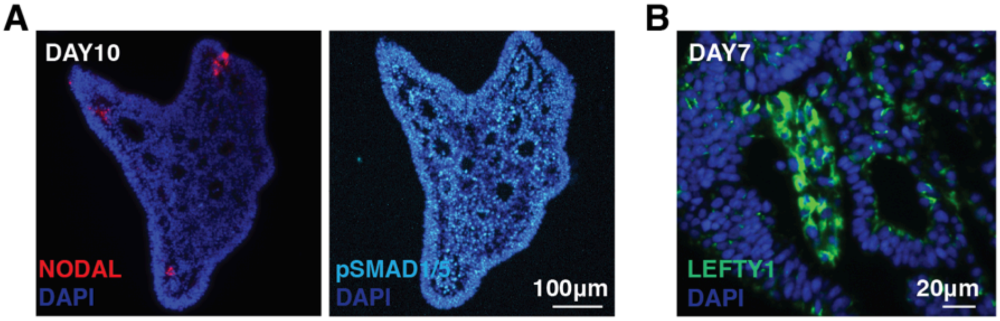

Figure 2.15 Gene expression distribution within extensions.
A) Immunofluorescence staining of an elongating 4μM CHIR organoid at day 10 of differentiation for NODAL and pSMAD1/5. B) Immunofluorescence staining of an elongating organoid at day 7 of differentiation for LEFTY1.

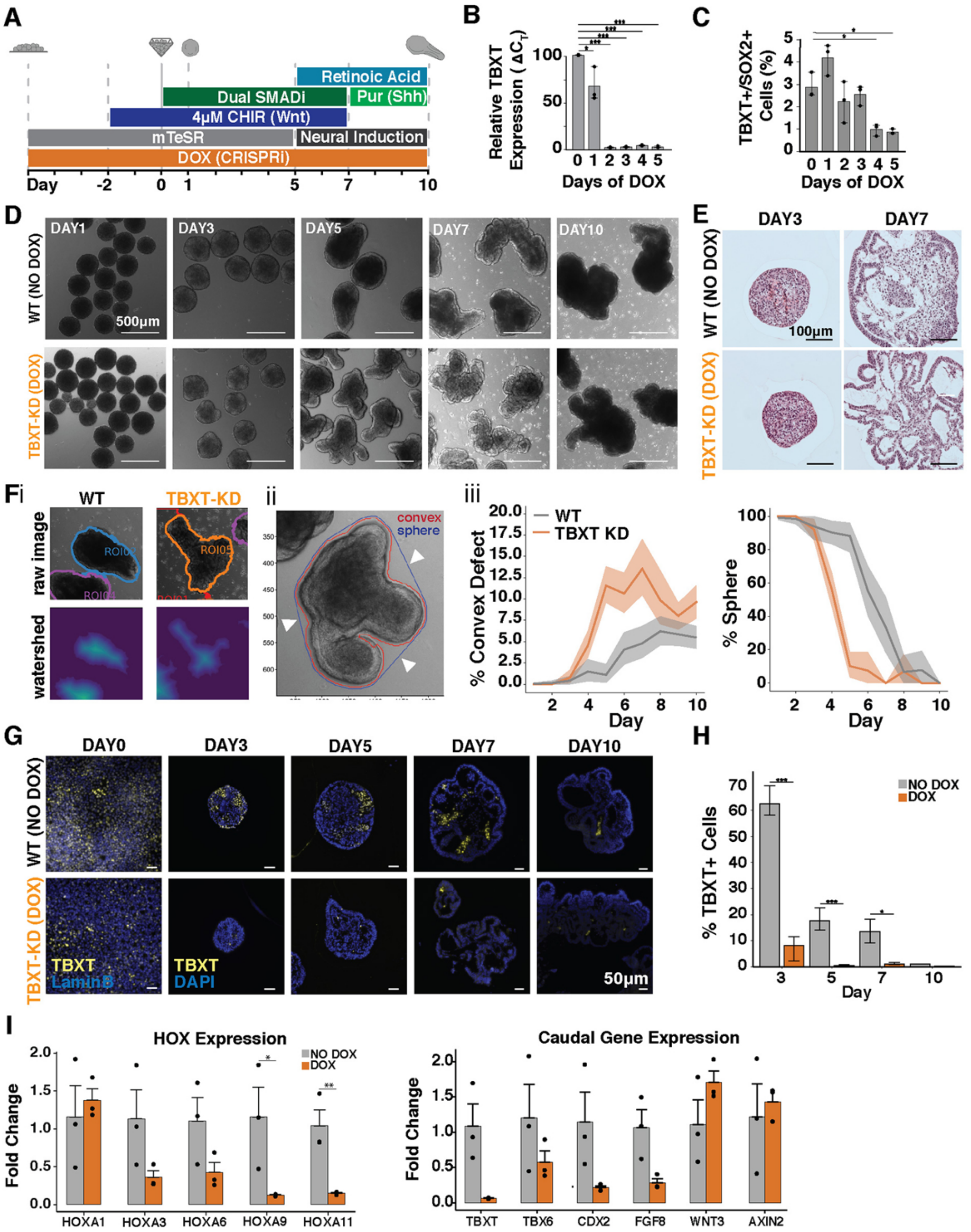

Figure 2.16 TBXT knockdown leads to increased epithelial folding.
(A) Schematic of differentiation protocol timeline with TBXT knockdown (KD) induction via doxycycline (DOX). (B) Quantification of TBXT-KD efficiency by qPCR showing reduction in mRNA expression levels on day 0 of differentiation (day 5 of DOX treatment). (C) Quantification by flow cytometry of TBXT+SOX2+ cells with DOX treatment over time. (D) Bright-field images of the differentiation of TBXT-KD hiPSC line with and without DOX treatment (wild type; WT) over time. (E) Histological sections of organoids with and without DOX treatment at day 3 and 7 of differentiation. (F,i) Example images of organoid segmentation; (ii) example image of convex indentations on organoids (arrowheads indicate convex defects); (iii) quantification of the percent of organoids with convex defects and quantification of the loss of sphere morphology in organoids over time (n>14 organoids at each timepoint). (Figure caption continued on the next page.)

(Figure caption continued from the previous page.) (G) TBXT immunofluorescence staining of fixed cells (day 0) or organoid paraffin sections (days 3-10) with and without DOX treatment. (H) Quantification of the immunofluorescence signal indicating loss of TBXT (Student's t-test;*P<0.05 and ***P<0.0005). (I) qPCR quantification of HOX genes and genes related to axial pattern specification from day 10 organoids with and without DOX treatment (Student's t-test; *P<0.05 and **P<0.005).

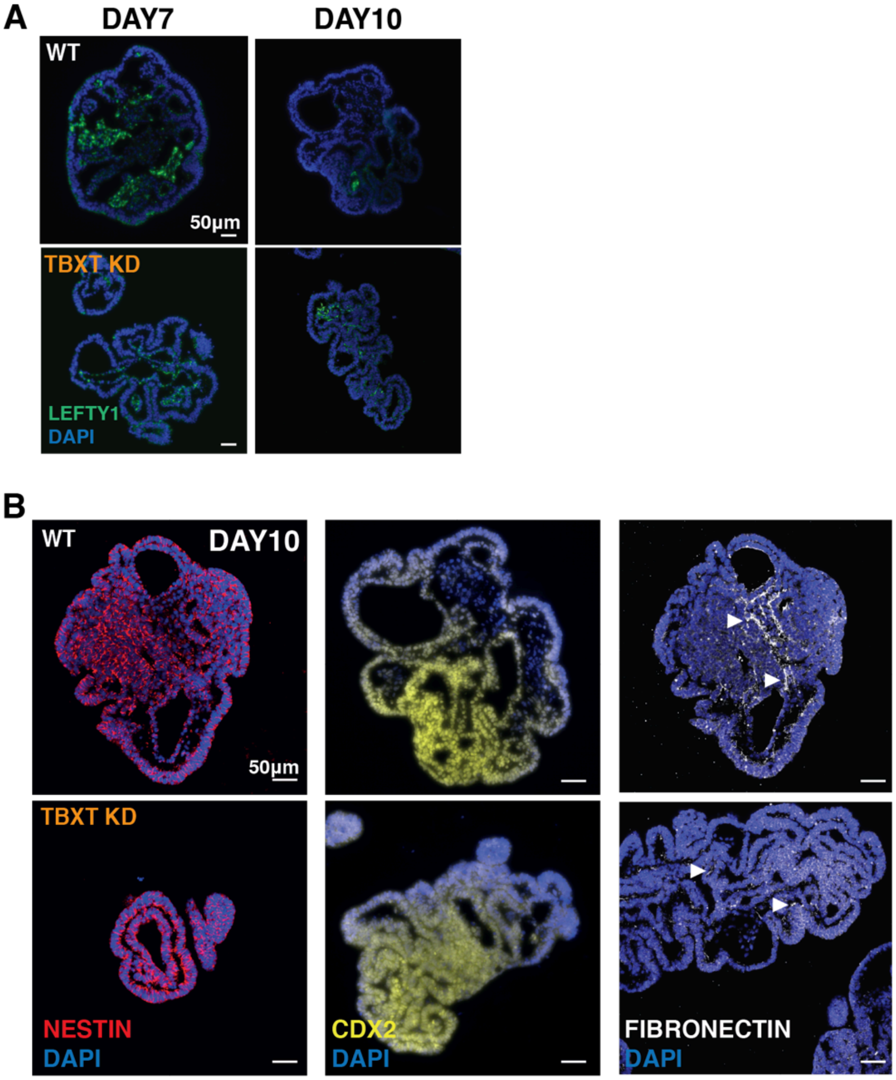

Figure 2.17: Marker expression after TBXT knockdown.
A) Immunofluorescence staining of paraffin sections for LEFTY at day 7 and 10 in 4µM CHIR organoids with and without DOX treatment. B) Immunofluorescence staining of paraffin sections for NESTIN, CDX2, and Fibronectin at day 10 in wildtype and KD organoids.

Materials and Methods

Human induced pluripotent stem cell line generation and culture

All work with human induced pluripotent stem cells (iPSCs) or human embryonic stem cells (ESCs) was approved by the University of California, San Francisco Human Gamete, Embryo, and Stem Cell Research (GESCR) Committee. Human iPSC lines were derived from the WTC11 line (Coriell, #GM25256), the WTB line (Conklin Lab) (Miyaoka et al., 2014) and the Allen Institute WTC11-LaminB cell line (AICS-0013 cl.210). The human ESCs were the H7 and H1 lines (WiCell). All cell lines were karyotyped by Cell Line Genetics and reported to be karyotypically normal. Additionally, all cell lines tested negative for mycoplasma using a MycoAlert Mycoplasma Detection Kit (Lonza).

Human iPSCs were cultured on growth factor reduced Matrigel (Corning Life Sciences) and fed daily with mTeSRTM-1 medium (STEMCELL Technologies) (Ludwig et al., 2006). Cells were passaged by dissociation with Accutase (STEM CELL Technologies) and re-seeded in mTeSRTM-1 medium supplemented with the small molecule Rho-associated coiled-coil kinase (ROCK) inhibitor Y276932 (10 μM; Selleckchem) (Park et al., 2015) at a seeding density of 12,000 cells per cm^2.

The generation of the TBXT CRISPRi line first involved TALEN-mediated insertion of the CRIPSRi cassette pAAVS1-NDi-CRISPRi (Gen2) (Addgene) to the AAVS1 locus of the Allen Institute WTC11-LaminB cell line. Following antibiotic selection of clones that received the CRIPSRi cassette, CRISPRi gRNAs were generated targeting TBXT (Table S2) using the Broad Institute GPP Web Portal and cloned into the gRNA-CKB (Addgene) following the previously described protocol (Libby et al., 2018). Guide RNA vectors were nucleofected into the LaminB CRISPRi iPSC line using a P3 Primary Cell 96-well Nucleofector Kit (Lonza) and the 4D Nucleofector×Unit (Lonza) following the manufacturer's instructions. Nucleofected cells were allowed to recover in mTeSR-1 medium supplemented with Y276932 (10 μM) and then underwent antibiotic selection with blasticidin (ThermoFisher Scientific; 10 μg/ml) following the previously published protocol (Beck et al., 1995; Amin et al., 2016). Knockdown efficiency was evaluated by addition of doxycycline to the daily feeding media over the course of 5 days, collection of mRNA and subsequent quantification of gene expression by qPCR.

Organoid differentiation

Organoid differentiation was performed according to a modified version of a previously published spinal cord interneuron differentiation protocol (Butts et al., 2017). Human iPSCs or ESCs were seeded at 125 000 cells/cm^2 in mTeSR-1 medium supplemented with the small-molecule Rho-associated coiled-coil kinase (ROCK) inhibitor Y276932 (10 μM; Selleckchem) and small-molecule GSK inhibitor CHIR99021 (2 μM, 4 μM or 6 μM; Selleckchem). Two days later, cells were singularized with Accutase (STEMCELL Technologies), counted using a Countess II FL (Life Technologies) and seeded into 800 μm×800 μm PDMS microwell inserts in a 24-well plate (~270 wells/insert) (Hookway et al., 2016). After ~18 h, condensed organoids were transferred to rotary culture in six-well plates in mTeSR-1 medium supplemented with Y276932 (10 μM; Selleckchem), CHIR99021 (2 μM, 4 μM, or 6 μM; Selleckchem), ALK5 small-molecule inhibitor SB431542 (10 μM, Selleckchem) and small-molecule BMP inhibitor LDN193189 (0.2 μM, Selleckchem) at an approximate density of 270 aggregates per well unless otherwise mentioned in the figure legend. Organoids were fed every other day for up to 17 days. Y276932 was removed from the media on day 3. At day 5, organoids were transferred to Neural Induction Media [DMEM F:12 (Corning), N2 supplement (Life Technologies), L-Glutamine (VWR), 2 μg/ml heparin (Sigma Aldrich), non-essential amino acids (Mediatech), penicillin-streptomycin (VWR), supplemented with fresh 0.4 μg/ml ascorbic acid (Sigma Aldrich) and 10 ng/ml brain derived neurotrophin factor (BDNF, R&D Systems)] supplemented with CHIR99021 (2 μM, 4 μM, or 6 μM; Selleckchem), SB431542 (10 μM, Selleckchem) and LDN193189 (0.2 μM, Selleckchem). From day 7 onwards, organoids were fed with Neural Induction Media supplemented with retinoic acid (10 nM, Sigma Aldrich), purmorphamine (300 nM, EMD Millipore) and N-[N-(3,5-

difluorophenacetyl)-L-alanyl]-S-phenylglycine t-butyl ester (DAPT D5942, 1 μM, Sigma-Aldrich).

Organoid elongation imaging and quantification

Day 5 organoids from a single 10 cm dish were individually transferred using wide-bore pipette tips into the center 60 wells of an uncoated ultra-low attachment 96-well plate (Corning), seeding exactly one organoid per well, with the remaining organoids maintained in rotary culture through day 7. Using an inverted Axio Observer Z1 (Zeiss) microscope with incubation (Zeiss Heating Unit XL S, maintained at 37°C, 5% CO_2), all 60 wells were imaged using an AxioCam MRm (Zeiss) digital CMOS camera at 5× magnification (NA 0.16, 2.6 μm×2.6 μm per pixel). Each well was imaged in TL Brightfield every 20 min for 48 h giving a total of 145 frames. At the end of imaging (day 7), 31 organoids from the parallel rotary culture were imaged at 5× magnification to generate a comparison image set.

To segment the organoids, all well images were first aligned by fitting a truncated quadratic curve to the average image intensity, then solving for the peak of maximum intensity, which was assumed to be the well center. Next, the average lighting inhomogeneity was calculated as the pixel-wise median of all 60 aligned well images, which was then subtracted from the individual aligned frames. After background correction, individual organoids were isolated by finding objects brighter than 0.83% of maximum intensity, but less than 3.0% of maximum intensity, with object size greater than 2000 pixels, eccentricity greater than 0.1 and solidity greater than 40%. A bounding box 2 mm×2 mm around the center of each of these objects was calculated and all frames of the time series cropped to this bounding box to reduce memory usage. To detect the region of maximum motion in the time series, the difference between each pair of sequential images was calculated and then the pixel wise standard deviation was calculated over all these differences in a given region. This standard deviation image was then thresholded at between 0.01 and 0.03 (AU) depending on the remaining lighting inhomogeneity in the image, producing a ring-shaped mask around the periphery of each organoid. Finally, using the interior of the mask as the organoid seed and the exterior as the background seed for the first frame, organoids were segmented using anisotropic diffusion (Grady, 2006), evolving the foreground and background seeds using the contour calculated from the previous frame for subsequent segmentations. Segmentation, labeling and metrology were all performed using the python package sckit-image (van den Walt et al., 2014).

Segmentations were manually inspected for accuracy, with 45 out of 60 determined as having no or only minor flaws, with the remaining 15 excluded from automated analysis. Using the high-quality segmentations only, each organoid time series was then analyzed to examine geometry change over time. For each contour at each time point, we calculated contour area, contour perimeter, minimum, maximum and mean distance from contour center of mass to the perimeter. As additional non-dimensional measures of shape, we calculated the ratio of maximum to minimum radius and organoid circularity. Organoids were also manually classified as 'elongating', 'partially elongating' or 'non-elongating' by examining each video. Organoids assigned to 'elongating' exhibited at least one, and at most two large protuberances that extended at least 100 μm from the main body. Partially elongating organoids exhibited at least one, but often many, protuberances, all of which failed to extend robustly past the 100 μm demarcation. Non-elongating organoids were any organoids that failed to generate any extensions over the observation period.

To estimate the number of extensions, TBXT-KD organoids were segmented in bright field as described above. The number of organoid extensions was assessed by analyzing deviation from convex planform area. Specifically, the convex hull of each organoid contour was calculated from organoid perimeter contour, then the organoid planform area was subtracted from the organoid convex area. Resulting regions of at least 30 μm^2 were classified as convexity 'defects' and further analyzed. Organoids with zero defects were classified as 'round'. Organoids with one or two defects were classified as 'single extensions'. Organoids with more than three defects were classified as containing multiple extensions. Furthermore, a ratio of defect area to convex area for each organoid was calculated, to estimate how perpendicular each extension was from the main organoid body. Finally, organoid perimeter tortuosity was assessed as the ratio of convex perimeter to segmented perimeter, with ratios of 1.0 approaching perfect smoothness, and ratios of zero approaching levels of convolution.

Real time quantitative polymerase chain reaction

Total RNA was isolated from organoid samples using an RNAeasy Mini Kit (QIAGEN) according to manufacturer's instructions. Subsequently, cDNA was generated using an iScript cDNA Synthesis kit (BIORAD) and the reaction was run on a SimpliAmp thermal cycler (Life Technologies). A quantitative PCR reaction using Fast SYBR Green Master Mix (ThermoFisher Scientific) was run on a StepOnePlus Real-Time PCR system (Applied Biosciences). Relative gene expression was determined by normalizing to the housekeeping gene 18S rRNA, using the comparative threshold (CT) method. Gene expression was displayed as fold change of each sample versus control. The primer sequences were obtained from the Harvard Primer bank or designed using the NCBI Primer-BLAST website (Table S1).

Owing to low RNA abundance in the dissected organoids, PreAmp Master Mix (FLUIDIGM) was used to amplify cDNA. Briefly, 20 ng of cDNA were amplified per 5 µl reaction volume for 15 cycles on a SimpliAmp thermal cycler (Life Technologies). Amplified cDNA was diluted fivefold using nuclease-free water. 1 µl of amplified diluted cDNA was used for each 20 µl quantitative PCR reaction using Fast SYBR Green Master Mix (ThermoFisher Scientific) and run on a StepOnePlus Real-Time PCR system (Applied Biosciences), following normal qPCR methods described above.

Histology, immunocytochemistry and imaging

Organoids were fixed with 4% paraformaldehyde (VWR) for 40 min and washed three times with PBS. Organoids to be used for histology were embedded in HistoGel Specimen Processing Gel (Thermo Fisher) prior to paraffin processing. Paraffin-embedded samples were sectioned at 5 µm, and subsequently stained using Hematoxylin and Eosin. For immunofluorescent staining, slides were deparaffinized as for Hematoxylin and Eosin staining. Epitope retrieval was performed by submerging slides in citrate buffer (pH 6.0; Vector Laboratories) in a 95°C water bath for 35 min. Samples were permeabilized in 0.2% Triton X-100 (Sigma-Aldrich) for 5 min, blocked in 1.5% normal donkey serum (Jackson Immunoresearch) for 1 h, and probed with primary antibodies against SOX2, PAX6, TBXT, NES, TUBB3 and CDH2 (Table S3) overnight at 4°C and with secondary antibodies (Alexa Fluor-488/555/647, ThermoFisher Scientific) for 1 h at room temperature. Nuclei were stained with a 1:10,000 dilution of Hoechst 33342 (Thermo Fisher) included with secondary antibodies. Coverslips were mounted with anti-fade mounting medium (ProlongGold, Life Technologies) and samples were imaged on a Zeiss Axio Observer Z1 inverted microscope equipped with a Hamamatsu ORCA-Flash 4.0 camera.

Whole-mount light sheet imaging

4% paraformaldehyde-fixed paraffin-embedded samples (see 'Histology, immunocytochemistry and imaging' section) were permeabilized with 1.5% Triton X-100 (Sigma Aldrich) for 1 h, blocked in 5% normal donkey serum (Jackson Immunoresearch) for 1 h, and probed with primary and secondary antibodies (Table S3) overnight. Nuclei were stained with a 1:10,000 dilution of Hoechst 33342 (Thermo Fisher) included with secondary antibodies. Samples were then embedded in 1.5% low melt agarose (BioReagent) and drawn up into ~1 mm imaging capillaries and subsequently imaged on the Zeiss Z.1 light sheet microscope equipped with two PCO.edge SCMOS cameras at 5× and 20× (NA 1.34, aqueous objective).

Flow cytometry

WTC and H1 cells were pretreated with either 2, 4 or 6 μM CHIR for 2 days, then dissociated from tissue culture plates with Accutase (STEMCELL Technologies) and washed with PBS. Similarly, the LBC-TBXT knockdown cells were pretreated with between 0 and 5 days of doxycycline concurrent with a final 2 days of 4 μM CHIR treatment, then dissociated and washed as described above. Cells were fixed for 20 min with 4% paraformaldehyde and washed three times for 3 min with PBS. Samples were permeabilized in 0.5% Triton-X-100 (Sigma Aldrich) for 30 min, then blocked in 1% normal donkey serum (Jackson Immunoresearch) for 1 h, and probed with primary and secondary antibodies (Table S3) overnight. Samples were run on a LSR-II analyzer (BD Biosciences). Singlets were first identified by gating on forward-scatter to side-scatter ratio, then samples were gated into SOX2$^+$ and TBXT$^+$ using single-stained controls for each cell line, then finally samples were assessed for percent SOX2$^+$/TBXT$^+$ cells. Analysis was conducted with a minimum of 20,000 events per sample.

Bulk RNA-sequencing sample and library preparation

Whole organoids differentiated in either 0 μM CHIR or 4 μM CHIR at days 1, 3, 5, 7 and 10 of the differentiation protocol (*n*=3 per condition per day) were lysed with RPE buffer with 5 mM 2-mercaptoethanol, and RNA was extracted using the RNeasy Mini Kit (Qiagen) and quantified using the NanoDrop 2000c (ThermoFisher Scientific). RNA-seq libraries were generated using the SMARTer Stranded Total RNA Sample Prep Kit (Takara Bio) and sequenced using NextSeq500/550 High Output v2.5 kit to a minimum depth of 25 million reads per sample. The sequences were aligned to GRCh37 using HiSat2 (Kim, et al., 2015), reads were quantified using the featureCounts tool in the subread package (Liao et al., 2014), and differential expression between 0 μM and 4 μM CHIR-treated organoids was assessed at each day using the edgeR differential expression pipeline with limma/voom normalization (Law et al., 2014). Longitudinal differential expression was assessed for each CHIR condition using the 'l' normalization algorithm (Zhang et al., 2019). Raw data have been deposited in GEO under the accession number GSE155382.

Single cell RNA-sequencing sample and library preparation

Multiple organoid samples were combined and processed together using the MULTI-Seq technology (McGinnis et al., 2019). Organoids were singularized using Accutase (STEMCELL

Technologies) and washed with ice-cold PBS. Cells were resuspended in PBS with lipid-modified Anchor and Barcode oligonucleotides (gifts from Zev Gartner, UCSF, USA) and incubated on ice for 5 min. A co-Anchor oligo was then added in order to stabilize membrane retention of the barcodes incubated for an additional 5 min on ice. Excess lipid-modified oligos were quenched with 1% BSA in PBS, washed with ice-cold 1% BSA solution, and counted using a Countess II FL (Life Technologies). Single cell GEMs and subsequent libraries were then prepared using the 10× Genomics Single Cell V2 protocol with an additional anchor-specific primer during cDNA amplification to enrich barcode sequences. Short barcode sequences (~65-100 bp determined by Bioanalyzer) were purified from cDNA libraries with two sequential SPRI bead cleanups. Barcode library preparation was performed according to the KAPA HiFi Hotstart (Kapa Biosystems) protocol to functionalize with the P5 sequencing adapter and library-specific RPIX barcode. Purified ~173 bp barcode fragments were isolated with another SPRI bead cleanup and validation by Bioanalyzer. Raw data are have been deposited in GEO under accession number GSE155383.

The sample library was sequenced on an Illumina NovaSeq yielding an average of 41,112 reads per cell and 6444 cells. The MULTI-Seq barcode library was sequenced on an Illumina NextSeq yielding an average of 9882 reads per barcode and enabling sample assignment for 4681 of 6124 unique UMIs detected (76.4% recovery), using the demultiplexing code provided by the MULTI-Seq protocol (McGinnis et al., 2019).

Genome annotation, RNA-seq read mapping, and estimation of gene and isoform expression

The sample library was aligned to the human GRCh38 reference genome using Cell Ranger v1.2.0 (10× Genomics). Gene expression levels were assessed using the Seurat v3.0.0 analysis pipeline (Butler et al., 2018). First cells were removed with fewer than 200 detected genes, with fewer than 1000 total detected transcripts or with more than 10% mitochondrial gene expression. Next, expression levels were log normalized, and the top 2000 variable genes calculated using the VST algorithm. The top 20 principal components were used to group cells into two clusters using a resolution of 0.3. Finally, top markers were detected for each cluster by detecting the top differentially expressed genes between both clusters, where at least 25% of cells in the cluster expressed the gene and expression of the gene was at least a 0.25 log2 fold-change different from the remaining population. Clusters and gene expression were visualized on a two-dimensional UMAP projection of the first 15 principal components.

Cluster analysis

To assign cluster identity, the top markers for each cluster were tested for GO term enrichment using the biological process 'enrichGO' function in the R package 'clusterProfiler' v3.12 (Yu et al., 2012). In addition, differentiation maturity in each cluster was assessed by examining expression level of panels of early neuroectoderm markers, proliferation markers, markers of neuron fate commitment, and markers of cell types present in neural tube formation and axial extension (Tanabe and Jessell, 1996). Finally, to assess anterior-posterior position of each, panels of HOX genes were examined to assign rough position of each cluster along the head-tail axis (Bel-Vialar et al., 2002; Carpenter, 2002).

Quantification of EdU and PH3 localization

Sections stained for DAPI, EdU and pH3 were segmented by detecting the peaks of DAPI staining for each section using non-maximum suppression. The exterior of each section was then segmented by grouping DAPI$^+$ cells into spatially contiguous clusters consisting of at least 5000 pixels that touch the image border in less than 1% of their total area. The exterior contour was then calculated for each region and fit to an elliptical model by total least squares (Halir and Flusser, 2020). All detected cells were projected onto the ellipse major axis, which was then normalized by total length. Where more detections fell on the left half of the major axis, the coordinates were reversed such that the right half of each projected section always contained the majority of detections. Detected cells that corresponded to pH3 or EdU fluorescence at 20% or more above the background level outside of any section were counted as positive detections. A

15-bin histogram was then used to calculate the percentage of projected cells for each day at each point along the semi-major axis, and then gaussian kernel density estimation was used to produce the empirical distribution. Linear and quadratic models were fit using ordinary least squares over the total population.

RNAScope

In situ hybridization for HOXB1, HOXC6 and HOXB9 (probe information in Table S4) was performed on sections of 4% paraformaldehyde-fixed paraffin-embedded samples (see 'Histology, immunocytochemistry and imaging' section) using the RNAscope Multiplex Fluorescent Reagent Kit v2 (Advanced Cell Diagnostics) and following the protocol outlined in User Manual 323100-USM. Sections were imaged on a Zeiss Axio Observer Z1 inverted microscope equipped with a Hamamatsu ORCA-Flash 4.0 camera.

Statistical analysis

Each experiment was performed with at least three biological replicates. Multiple comparisons were used to compare multiple groups followed by unpaired *t*-tests (two tailed) between two groups subject to a post-hoc Bonferroni correction. In gene expression analysis, three replicates were used for each condition, and all gene expression was normalized to control wild-type populations followed by unpaired *t*-tests (two-tailed). Significance was specified as $P<0.05$, unless otherwise specified in figure legends. All error bars represent standard error of the mean (s.e.m.) unless otherwise noted in the figure legend.

Acknowledgements

We thank the Gladstone Light Microscopy and Histology Core, the Gladstone Stem Cell Core, the Gladstone Flow Cytometry Core and the Gladstone Graphics Team for their support and experimental expertise. Additionally, we specifically thank Dr. Vaishaali Natarajan for her expertise and assistance with flow cytometry.

CHAPTER 3

Distinct differentiation trajectories leave lasting impacts on gene regulation and function of V2a neurons

Introduction

Human pluripotent stem cell (hPSC)-derived tissues offer immense potential for disease modeling and novel therapeutic interventions. A major question in the field has been how to best transition pluripotent stem cells into desired cell lineages. This endeavor has led to methods that either mimic developmental processes through 'directed differentiations' or rely on transcription factor overexpression in 'induced differentiations'. During development, temporally distinct and spatially separated progenitor populations may give rise to seemingly analogous cell types with common morphological features and expression of hallmark genes. However, these lineally separated populations often differ tissue localization or functional capacity. Some examples of this include cardiomyocytes arising from the first or second heart fields, melanocytes differentiated from neural crest or Schwann cell-derived precursors (Samuel et al., 2023), and neurons of the central and peripheral nervous systems (Alshawaf et al., 2018; Fattahi et al., 2016).

The molecular and functional differences that exist between such analogous cell types can be even larger when comparing cells generated using developmentally relevant strategies to those generated through induced differentiation via transcription factor over expression in stem cells (Elder et al., 2022; Fernandopulle et al., 2018; Zhang et al., 2013). Induced cells can express key marker genes and morphologically resemble the target population, but by nature of having skipped developmental stages, can also misregulate transcription and chromatin marks. These differences necessitate the use of -omics level approaches to deeply characterize the transcriptional and chromatin landscape of cell populations and to facilitate in-depth comparisons between primary cell populations and those generated *in vitro*.

In this study, we investigate how differentiation trajectories influence the properties of V2a neurons—ventral, excitatory, ipsilaterally-projecting interneurons that emerge along the anteroposterior axis and play key roles in phrenic and locomotor circuits (Ampatzis et al., 2014; Azim et al., 2014; Bubnys et al., 2019; Crone et al., 2012; Hayashi et al., 2018). V2a neurons exhibit plasticity in restoring diaphragm function and are a key target population for the recovery of locomotion via electrical stimulation after spinal cord injury (Kathe et al., 2022; Squair et al., 2023; Zholudeva et al., 2017). Transplantation of V2a neurons also has potential as a cell therapy to enhance functional recovery after spinal cord injury, making this cell type of high therapeutic interest (Bonner & Steward, 2015; Zholudeva et al., 2018; Zholudeva & Lane, 2019).

V2a neurons develop over the entire axial range of the neural tube, and understanding how axial positioning intersects with their identity as a V2a neuron is critical for deriving therapeutically relevant cell types *in vitro* (Hayashi et al., 2018; Menelaou et al., 2014; Menelaou & McLean, 2019). *In vivo* and *in vitro*, axial patterning is one of the first steps of development, preceding much of differentiation (Metzis et al., 2018). Anterior V2a neurons primarily arise from neurectoderm progenitors (NEPs), which are induced by the inhibition of BMP and TGF signaling in pluripotent stem cells. By contrast, posterior V2a neurons are formed from a distinct population termed neuromesodermal progenitors (NMPs) which contribute to the posterior elongation of the embryo as they differentiate into the neural tube and adjacent somites (Cambray & Wilson, 2007; Henrique et al., 2015; Tzouanacou et al., 2009; Wymeersch et al., 2019). Despite differences in early development, subsequent dorsoventral patterning of the neural tube is remarkably conserved along the anteroposterior axis, producing V2a neurons that express the canonical marker VSX2 (also known as CHX10) (Clovis et al., 2016; Debrulle et al., 2019). However, the anteroposterior origin of V2a neurons could lead to molecular differences with potential functional implications. Indeed, V2a neurons exhibit different patterns of axon extension as well as long-term expression of the V2a marker VSX2 as a function of their location within the spinal cord in model organisms (Hayashi et al., 2018; Menelaou et al., 2014).

Here, we interrogate how early differences in developmental patterning and progenitor identity impact the resulting V2a phenotype using three distinct models of hPSC differentiation. We first established a novel system to generate V2a neurons from NMPs to compare their molecular and functional features with their NEP-derived counterparts. We then used multiomic single nucleus RNA and ATAC-seq approaches to examine how differences in the early developmental lineage are imprinted into the chromatin landscape and transcriptional signature of these neurons. We found that while both NEP-derived and NMP-derived V2a populations were similar to human tissue derived V2a neurons, the two *in vitro*-derived populations exhibited notable differences in gene expression and regions of open chromatin stemming from their distinct progenitor origins. Functional profiling of the neurons supported the differences observed in multiomics data, showing NMP-derived populations established network-wide activity more rapidly and consistently than NEP-derived neurons.

To further define the impact of differentiation trajectories on V2a neurons, we also established a protocol for induced differentiation which skips normal developmental patterning and rapidly transitions stem cells to post-mitotic neurons. We find that induced VSX2-expressing neurons greatly differ from both of our NEP and NMP-derived V2a populations, express genes not typically associated with V2a neurons, and shift their identity even after progressing to a post-mitotic state. Lastly, leveraging our multiomics dataset, we employed *in silico* gene regulatory network (GRN) modeling and perturbation to show how different transcription factors regulate lineage-specific differences between NEP and NMP-derived V2a populations. Our results highlight the significance of developmentally accurate directed differentiation strategies to generate relevant and authentic cell types for developmental and disease modeling and therapeutic application.

Results

Distinct neural progenitor populations can be differentiated to V2a neurons

To better understand how the axial identity influences mature V2a cell identity, we began by deriving NEPs and NMPs using previously established protocols before maturing these progenitor populations to V2a neurons under identical conditions (Butts et al., 2017, 2019; Lippmann et al., 2015). Mirroring the conditions of *in vivo* development, hPSCs are converted into NEPs via dual SMAD inhibition in FGF-containing stem cell media for the first 5 days (**Figure 3.1A**; top method). NMPs are induced *in vivo* and *in vitro* by balanced FGF and WNT signaling and are identified by co-expression of SOX2 and TBXT (also known as Brachyury), as well as the caudal homeodomain protein CDX2. We performed an NMP induction protocol (**Figure 3.1A**; bottom method) (Lippmann et al., 2015) that resulted in high levels of SOX2 and TBXT coexpression and >90% CDX2 expression at day 5 (**Figure 3.1B-D**). Notably, TBXT and CDX2 were completely absent in the NEP condition at a matched time point (**Figure 3.1B-D**).

Following NEP or NMP induction over the first 5 days of differentiation, the progenitor populations were subsequently differentiated toward V2a interneurons under identical media formulations (**Figure 3.1E**). Since the neural tube patterning is highly conserved between anterior and posterior regions *in vivo*, identical treatment from day 5 onward allowed us to specifically investigate the impact of early progenitor origins on the resulting neurons. We compared the differentiated populations at day 7 following 48 hours of dual SMAD inhibition in the presence of 100 nM RA, a potent neuralizing morphogen. At this time-point, both populations began to co-express canonical neural progenitor markers SOX2 and PAX6, while TBXT levels in the NMP-derived population dropped significantly (**Figure 3.1C,F**). CDX2 remained highly expressed in the NMP-derived progenitors (**Figure 3.1D**). These data show the efficient generation of neural progenitors via two different differentiation routes that converge on a SOX2+ PAX6+ neural phenotype.

Prior studies have generated V2a neurons from neural progenitors via balanced control over three developmental signaling pathways: retinoic acid, Sonic hedgehog (SHH), and Notch (Butts et al., 2017, 2019). Retinoic acid generated by the paraxial somites and SHH secreted by the floor plate serve to pattern the neural tube, while the Notch pathway controls the balanced acquisition of excitatory V2a and inhibitory V2b fates from p2 progenitors. *In vitro*, the small molecule agonist purmorphamine (PUR) is substituted for SHH while the gamma-secretase inhibitor DAPT potently inhibits Notch signaling and biases p2 progenitors toward the V2a fate at the expense of the V2b fate. To further optimize the timing and concentration of PUR and DAPT to yield increased V2a neurons in our differentiations, we generated a Cre lineage reporter under the control of the transcription factor FOXN4, which is expressed solely in p2 progenitors. This lineage reporter (called FOXN4:Cre or abbreviated FC) allowed us to observe the efficiency of p2/V2a differentiation in live cultures through the readout of a GFP reporter. We used the FOXN4:Cre line to test 16 iterations of the differentiation protocol where we varied the timing or concentration of PUR and DAPT (**Figure 3.1G**). We found that 300 nM PUR added from day 7 onward significantly increased the GFP+ area over our control condition with 100 nM PUR (**Figure 3.1G**). Therefore, this modification was used throughout the rest of this study.

On day 19 of V2a differentiation, cells were dissociated and assessed for the canonical V2a marker VSX2 via flow cytometry (**Figure 3.1H**). While VSX2+ V2a neurons were detected in all differentiations across four independent cell lines, the NMP condition consistently produced higher percentages of V2a neurons under our experimental conditions (**Figure 3.1H**). We further validated V2a identity by flow cytometry for secondary markers SOX14 and SOX21 and observed significant enrichment of each marker in the VSX2+ population (**Figure 3.1I**). Finally, cells that were replated and allowed to grow for an additional two days generated extensive networks of neurites, supporting neural identity (**Figure 3.1J**). These results confirm the V2a neuron identity in both the NEP- and NMP-derived cultures.

Differentiated neurons from distinct progenitor lineages recapitulate the identities of the ventral neural tube

Having established neural populations with a canonical V2a identity (VSX2+/SOX14+/SOX21+) via both differentiation methods and across multiple cell lines, we examined whether epigenetic and gene regulatory patterns differed based on early progenitor lineage. To address these questions, we performed single nucleus multiome sequencing after 19 days of differentiation (**Figure 3.2A**).

We first used the snRNA-seq data to cluster and annotate cell types according to known markers (**Figure 3.2B, Figure 3.S1**). V2a neurons expressed VSX2, LHX3, LHX4, SOX21, and SOX14. Motor neurons (MN) were identified by PHOX2A, PHOX2B, and ISL1 expression or MNX1 (also known as HB9) and ISL1 expression, representing cranial or spinal identities, respectively. Overlap of PHOX2B and POU4F1, detected in one NMP-derived sample, was suggestive of a sensory neuron population (SN), possibly arising from a small population of neural crest cells arising during NMP differentiation (**Figure 3.S1G,H, Figure 3.S2A**). Non-V2a ventral interneurons, such as V3, V1, and V0 neurons clustered together as seen by expression of a mix of ventral markers, including SIM1, LHX1, and PAX2 were labeled ‘interneurons’. We also identified a large population of p2 progenitors that expressed PAX6, IRX3, FOXN4, and VSX1. Other cells expressed primarily SOX2 and NKX6.2 which are widely expressed across the ventral progenitor domains and were therefore broadly termed ‘progenitors’. Similarly, a population that expressed neural genes STMN2, NEFL, and MAPT but lacked specific population markers were called ‘early neurons’. Lastly, highly specific expression of SHH, FOXA2, and ARX indicated the presence of floor plate (FP) cells.

When comparing the relative proportions of each cell type in each sample, we again noted that the NMP condition produced a higher proportion of V2a neurons (**Figure 3.S2A**). Only the

NEP condition, however, contained floor plate populations. There was also a noticeable shift in the proportion of motor neurons and interneurons between the NEP and NMP conditions. Although both conditions were treated with the same concentration and duration of PUR to produce ventral identities, there is a stronger ventral bias in the identities in the NEP-derived samples compared to those of the NMP condition. This ventral shift is seen in the presence of the floor plate and proportionally larger motor neuron populations, which are ventral to the p2/V2 domain *in vivo* (**Figure 3.S2A**).

We also examined which anteroposterior markers were expressed in our NEP and NMP conditions (**Figure 3.S2B**). We observed low expression of off-target forebrain, midbrain, and eye markers such as FOXG1, OTX2, and CRX (**Figure 3.S2B**). In the NEP-condition, HOX expression primarily ranged from HOX 1-5 paralogs, analogous to a hindbrain identity. NMP-derived samples also expressed these relatively anterior paralogs in addition to more caudal HOX genes such as HOXC5, HOXC6, and HOXB9, consistent with a cervical spinal cord identity (**Figure 3.S2B**). This assessment of axial markers supports a model where the NEP-derived V2a neurons more closely resemble hindbrain populations while NMP-derived neurons resemble spinal populations.

To further confirm our assigned cell identities, we performed an unbiased single cell label transfer between our cells and the ventral spinal cell types annotated in an *in vivo* human fetal dataset (Rayon et al., 2021). Label transfer results largely agreed with our annotations, with the exception of the *in vitro* p2 progenitors which mapped more strongly onto *in vivo* V2a neurons than *in vivo* p2 progenitors (**Figure 3.2C**). Further, the majority of our cells were identified as more mature neurons instead of progenitors, consistent with a largely post-mitotic neuronal state. Harmony integration of our RNAseq datasets clustered analogous cell types closely to one another, but did not entirely intermingle the NEP and NMP conditions (**Figure 3.2D**). Altogether, this analysis affirms our ability to identify regionally relevant cell types across all samples, including V2a neurons, correlate them with *in vivo* samples, and highlights the axial differences between populations derived from NEP or NMP conditions.

Early developmental differences leave epigenetic and transcriptional marks in lineally distinct V2a neurons

Early developmental patterning events play a crucial role in molding the chromatin to position cells for subsequent stages of development. Therefore, we leveraged our snATAC-seq data to examine whether the NEP and NMP differentiation stages left long-term marks on the chromatin landscape in ways that could influence transcriptional output and neuronal function (**Figure 3.3A**). To focus on the V2a population, we subset all V2a cells (2672 cells) and performed differential peak analysis. This identified 1996 regions ($\log2FC > 1$ and $FDR < 0.05$) that were differentially accessible between NEP and NMP V2a populations (**Figure 3.3B**). Examination of top differential peaks showed that peak sets included mutually exclusive regions with highly differential accessibility, not only peaks with differences in relative accessibility (**Figure 3.3B,C**).

Analysis of differentially accessible regions (DARs) did not identify differences in the relative location of peaks within genes, the distance from the nearest transcriptional start site, or the gene type annotation (protein coding, miRNA, etc.) of the nearest transcription start site (TSS) between NEP and NMP conditions (**Figure 3.S3**). However, motif enrichment analysis of the DARs between NEP and NMP V2a neurons did identify dozens of significantly enriched transcription factor binding motifs (**Figure 3.3E**). In order to identify broad patterns, we annotated transcription factor (TF) motifs by class, since many related TFs bind similar motifs. In the NEP condition, motifs of Rel homology region class were the most highly enriched (EBF1/2/3), followed by basic helix-loop-helix (bHLH) class motifs, and a mix of homeodomain and zinc-finger class motifs (**Figure 3.3E**). In the NMP condition, homeodomain class motifs were most strongly enriched, followed by C2H2 zinc-finger and nuclear receptor classes (**Figure 3.3F**). The nuclear receptor class contains retinoid-related transcription factors (e.g. RXRA, RXRB, RARA) which suggests a differential action of retinoic acid in the NMP condition. While both conditions have enriched homeodomain class TFs, CDX and ONECUT family motifs are more prevalent in the NMP condition while POU and TALE family motifs are more highly enriched in the NEP condition. The bHLH family of transcription factors are known to be key regulators of neurodevelopment and several of these factors are specifically expressed during V2a development (NEUROD1, NEUROG2, ASCL1, BHLHE22; Li et al., 2005; Lu et al., 2015). However, this TF class was specifically enriched in the NEP condition (**Figure 3.3D**). We also tested for gene ontology enrichment using the Genomic Regions Enrichment of Annotations Tool (GREAT) to see whether nearby genes were associated with specific functions. NEP V2a neurons possessed a modest enrichment for terms such as 'regulation of glutamatergic synaptic transmission' and 'regulation of voltage-gated calcium channel activity', while NMP V2a neurons had strong enrichment for broad terms related to regionalization, anterior/posterior patterning, and nerve development (**Figure 3.3D, Figure 3.S4**). These results show that the progenitor lineage of V2a neurons leaves lasting marks in the chromatin landscape even after two weeks of identical treatment. Further, these differentially accessible regions are likely to be acted upon by distinct families of transcription factors, suggesting the presence of distinct gene regulatory networks between these two conditions.

We next analyzed differences in the transcriptional networks between NEP and NMP-derived V2a neurons. Using the same set of V2a neurons, we identified 742 differentially expressed genes (**Figure 3.3F**; $\log2FC > 0.25$ and Bonferroni adjusted $p\text{-value} < 0.05$). Consistent with our earlier findings, HOX genes were differentially expressed, reflecting distinct axial identities. Notably, differences include transcription factors, ion channels, and axon guidance molecules related to GO terms such as axon development, synapse organization, and embryonic skeletal system morphogenesis (**Figure 3.3H-J**). GO analysis of the differentially expressed genes identified 22 significantly enriched GO terms that are shared between the NEP and NMP conditions, yet these enrichments are driven by mutually exclusive gene sets (**Figure 3.3K**). These findings suggest that NEP and NMP V2a neurons use distinct gene modules to achieve similar processes, such as axonogenesis, potentially leading to different circuit architecture of neurons residing at different axial levels of the hindbrain and spinal cord. When taken with the snATAC-seq analysis, these data point to systematic chromatin changes underlying distinct transcriptional networks of V2a populations derived from NEP or NMP progenitor pools.

We next asked whether the observed differences in motif enrichment were also present in the progenitors to the V2a neurons, the p2 cells, or whether it only manifested with terminal differentiation. We therefore subset the p2 cells (781 cells) from our dataset and performed similar analyses as above. Motif enrichment in NEP p2 compared to NMP p2 DARs closely mirrored the trends observed in the V2a neurons (**Figure 3.S5A,B**). DARs in NEP p2 cells were enriched in bHLH and homeodomain motifs, while NMP p2 regions were enriched in C2H2 zinc finger motifs and a non-overlapping set of homeodomain motifs, including CDX family genes. When we compared the DARS specific to the NEP or NMP lineage in both p2 and V2a populations, only 4.7% of NEP-specific DARs were shared between p2 and V2a neurons, while 10.7% of the NMP-specific DARs were conserved from p2 progenitors to V2a neurons (**Figure 3.S5C,D**). Comparing the global ATAC profile of p2 and V2a populations with a Pearson correlation showed the highest degree of similarly within cell identity, not progenitor lineage (**Figure 3.S5E**). These data highlight that distinct progenitor lineages impart lasting differences in the regulatory network which influences chromatin accessibility to transcription factors and that these differences persist across dynamic changes in chromatin accessibility that occur over developmental time.

Differences in population-wide synchronous activity in maturing neuron cultures

We next used calcium imaging to examine potential functional differences between NEP and NMP-derived V2a neurons. Dissociated cultures were replated at day 19 to a uniform density and allowed to form new networks for 4 days. The cell permeable dye Fluo4-AM was used to observe activity in cultures on an incubated microscope. At the day 23 timepoint, spontaneous neuronal activity was observed in both conditions, with the NMP-derived cultures eliciting a higher average number of fluorescence peaks per ROI (**Figure 3.4A**). However, at day 34 and day 43, the average number of peaks per ROI had equalized and became non-significant (**Figure 3.4A**).

These results show that when ROI are assessed individually, cells in both conditions have approximately the same amount of activity as measured by peaks in Fluo4 fluorescence.

However, examination of the average activity across all ROI also revealed synchronous bursts of activity across the whole culture that occurred simultaneously or in rapidly propagating waves. There was no significant difference in these bursts between NEP and NMP-derived neurons at day 23. However, we observed significantly more synchronous bursts in NMP-derived cultures at later time points compared to NEP cultures (**Figure 3.4B,C, Figure 3.S6**). These observations of differential bursting activity are unlikely to be due to differences in maturation given that the NEP and NMP cultures were day-matched for differentiation and we would not expect small relative differences in maturity to exhibit such strong effects over a three-week period of continued culture. However, we do note that differentially expressed genes between the NEP and NMP V2a neurons at day 19 include genes related to synapse organization and synaptic transmission (**Figure 3.3K**). Also, among the most highly differentially expressed genes were subunits of cation channels and which could impact synaptic transmission (CACNA2D1 and RYR2 in the NEP condition; CACNA2D3 and KNCD2 in the NEP condition).

Induced VSX2-expressing neurons do not resemble NEP or NMP-derived V2a neurons

Recently, the use of transcription factor overexpression to rapidly produce induced neurons has gained widespread popularity in the field (Elder et al., 2022; Fernandopulle et al., 2018; Wang et al., 2017; Zhang et al., 2013). This approach is highly efficient, scalable, and allows for the generation of neuron-like cells in just a few days, bypassing much of the complex developmental patterning typically required. Our data suggest that the developmental trajectories of the V2a precursors influence their epigenetic and transcriptional landscapes. We asked whether induced neurons that passed through minimal developmental patterning could share characteristics with either the NEP or NMP-derived populations. Based on the developmental similarities between V2a and lower motor neurons (MN), we hypothesized that removing ISL1 from the tripartite induced motor neuron cassette including NGN2, LHX3, and ISL1 could induce V2a neurons, since ectopic expression of LHX3 alone induces V2a neurons *in vivo* (**Figure 3.5A**) (Clovis et al., 2016; Mazzoni et al., 2013; Thaler et al., 2002).

Thus, we generated a plasmid containing a doxycycline-inducible NGN2::P2A::LHX3 cassette and inserted it into stem cells via piggybac transposon-mediated integration. Following 4 days of induction, we performed flow cytometry for VSX2. However, <1% of cells were positive for VSX2, despite achieving the expected neural morphology (**Figure 3.5B, Figure 3.S7A**). Since PSCs default to an anterior fate, we hypothesized that our induced neurons may need an additional caudalizing signal, such as retinoic acid (RA) (Gouti et al., 2014; Metzis et al., 2018; Ozair et al., 2012). When we added graded concentrations of RA to our induced neuron differentiation protocol, we found a proportional and significant increase in the percentage of VSX2+ cells after 4 days of induction, with a maximum efficiency of ~40% VSX2+ neurons at 1 uM RA (**Figure 3.5B, Figure 3.S7A).** Notably, when we tested identical conditions on the NGN2 induced neurons and the induced motor neurons, the number of VSX2+ neurons remained <1%.

We characterized day 4 and day 10 induced V2a neurons with multiome sequencing to assess their identity. While we detected VSX2+ clusters at day 4, these cells lacked expression of other V2a markers, such as SOX21, SOX14, and endogenous LHX3 (**Figure 3.5C, Figure 3.S7B,C**). The VSX2- clusters were largely positive for the motor neuron marker MNX1 (**Figure 3.5C, Figure 3.S7B,C**). While this was not the target population, the shared LHX3+ lineage of both cell types *in vivo* supports the idea that there could be a balance between these populations produced by overexpression of LHX3 in stem cells. More unexpected was the observation of PHOX2B and POU4F1 overlapping VSX2 and MNX1 populations, respectively, as well as the presence of other interneuron markers SIM1 and LHX1 (**Figure 3.5C, Figure 3.S7C,E**). Expression of PHOX2B and POU4F1 have been described in studies of NGN2-induced neurons and may be a product of the induced method (Lin et al. 2021). It is unclear if SIM1 and LHX1 are expressed under the same conditions. Nevertheless, these markers persist through day 10 and overlap remaining VSX2+ and MNX1+ clusters. To define the global similarities between induced and directed NEP and

NMP neurons generated *in vitro*, as well as to *in vivo* spinal neurons, we psuedobulked the RNA data from neuron clusters and embedded them in PCA space (**Figure 3.5D**). The PCA showed that both of the induced time points clustered distantly from the NEP, NMP, and *in vivo* clusters along PC1, as well as distantly from each other along PC2. By contrast, both NEP and NMP samples were close to *in vivo* clusters.

The motifs enriched in the differentially accessible peaks between day 4 induced neurons and combined NEP and NMP V2a neurons showed an enrichment of anterior homeodomain motifs such as GSC, CRX, and OTX2 in addition to the expected bHLH motifs from NGN2 overexpression (**Figure 3.5E**). At day 4, we noticed significant expression of the anterior gene OTX2 along with lower levels of eye-related factors CRX and RAX while HOX gene expression mostly stopped at HOXB2 (**Figure 3.5C,F**). However, day 10 induced neurons downregulated OTX2, CRX, and RAX and increased expression of HOXB5 and HOXB8, suggesting that they adopted a more caudal identity following an additional 6 days in culture in the presence of retinoic acid (**Figure 3.5C,F**). This caudal shift in identity from day 4 to day 10 was further supported by module scoring using the significantly differentially expressed genes between the NEP and NMP V2a neurons (**Figure 3.5G**).

These data show that induced neurons possess a superficial similarity to V2a neurons. Upon close inspection, these cells lack co-expression of secondary marker genes (SOX14 and SOX21) and express transcription factors that mark other cell populations (PHOX2B and POU4F1; **Figure 3.5C**). Further, the axial identity of these neurons appears to be labile after achieving a morphologically ‘neuron-like’ post-mitotic state (**Figure 3.5G**). This contrasts with normal developmental progression, where neural progenitors fail to acquire more caudal identities after an early signaling window (Metzis et al., 2018). While we did not exhaustively test transcription factor and small molecule combinations that could produce more robust V2a-like neurons, these experiments highlight that the most common V2a marker, VSX2, induced by LHX3 in a developmentally relevant progression is not sufficient to establish an underlying gene regulatory network that resembles that of a V2a neuron and that induced neurons are still susceptible to external cues. These findings prompted us to identify additional factors that govern the acquisition of lineally distinct V2a identity.

In silico GRN modeling predicts novel regulators of lineally distinct V2a neuron signatures

Having observed that different progenitor lineages conferred hundreds of differentially expressed genes and access to context-specific transcription factor motifs in post-mitotic neurons, we next sought to identify the gene regulatory network (GRN) responsible for these differences. For this, we turned to CellOracle, a computational tool which takes snRNA-seq and snATAC-seq data to construct population-specific GRNs based on correlating RNA expression and chromatin peak co-accessibility (Kamimoto et al., 2023). After building GRNs, individual TFs can be 'knocked out' *in silico* in order to predict changes in cell state or differentiation trajectory (**Figure 3.6A**).

Focusing on the V2a populations, we used CellOracle to produce separate GRNs for the NEP and NMP V2a populations using the top 3000 most variably expressed genes. We then examined which transcription factors contained the highest centrality scores in the predicted network, with higher scores correlating with larger numbers of total regulatory connections (**Figure 3.6B,C**). Both of the V2a populations contained largely overlapping lists of highly central TFs, likely a result of their shared identity. To investigate which of these TFs may explain the observed condition-specific differentially expressed genes, we knocked down each of the top 25 most central genes in NEP or NMP V2a populations *in silico*. We then performed Gene Set Enrichment Analysis (GSEA) on the perturbed conditions to identify what biological processes were up or down-regulated upon knockout (**Figure 3.6D, Figure 3.S8**). Several GSEA terms related to neural function were enriched in either the NEP or NMP condition by single gene knockout (**Figure 3.6D, Figure 3.S8**). In order to experimentally validate these computational predictions, we narrowed down the list of potential targets using several criteria including expression level, whether or not the gene was differentially expressed in the RNA-seq data, whether the TF or similar TF motifs were enriched in the ATAC-seq data, and centrality in both conditions. We selected PAX5, CREB5, KLF12, ONECUT2, and TCF7L2 for further validation (highlighted in **Figure 3.6B-D**). We knocked down these factors using short hairpin RNAs (shRNA) integrated into hPSCs using lentiviral vectors. hPSCs were then differentiated along the NEP or NMP routs toward V2a neurons (**Figure 3.6E**) and bulk RNA was collected for sequencing on day 19.

Next, we examined the genes that were differentially expressed in NEP or NMP knockdown conditions (**Figure 3.6F,G, Figure 3.S9**). Contrasting with the NEP condition where the majority of differentially expressed genes (DEG) were specific to knockdown of one gene (**Figure 6F**), we noticed that knockdown of either CREB5 or TCF7L2 in the NMP condition resulted in the largest total numbers of DEG, many of which were overlapping (**Figure 3.6G**). A heatmap of the DEG in the NEP and NMP CREB5 knockdown conditions showed that the NEP-specific DEG exhibited similar trends in the NMP conditions, although not statistically significant (**Figure 3.6H**). The NMP-specific DEG, however, had highly specific effects, and were also enriched for the DEG identified in our multiome data (**Figure 3.6H**). Similar observations were made for the TCF7L2 knockdown (**Figure 3.S9A**). While neither the NEP or NMP module was significantly altered in the NEP differentiations, both CREB5 and TCF7L2 knockdowns significantly reduced the NMP module in NMP differentiations (**Figure 3.6I,J**). Thus, it appears that CREB5 and TCF7L2 play key regulatory roles specific to the NMP lineage and that they contain largely overlapping regulons.

Lastly, we examined the list of differentially accessible regions between NEP and NMP V2a neurons and filtered it for peaks that were annotated in or nearest to the DEG in the NMP CREB5 knockdown samples. This identified 25 NMP-enriched peaks within or near 15 unique genes downregulated by CREB5 KD, including PLXNA2, a semaphorin receptor which plays a role in axon guidance, and PBX3, a transcription factor which can form complexes with HOX genes and is thought to play a wide role in early development (**Figure 3.6K,L**). These findings suggest that CREB5 and TCF7L2 could regulate some of their DEG by either opening unique regions of chromatin or by binding to these peaks to regulate transcription.

Discussion

Our study demonstrates that distinct developmental trajectories in the differentiation of V2a neurons result in lasting, lineage-specific transcriptional and functional differences. Using two distinct progenitor differentiation methods—one generating NEP and the other NMP—we observed that these lineages exhibit differential gene expression, chromatin accessibility, and network activity, even under identical culture conditions during the later stages of differentiation.

Our multiomic analysis revealed that early lineage differences imprint unique chromatin landscapes that persist into the mature neuron stage, suggesting that early developmental events impart structural changes in chromatin that influence long-term gene regulatory networks. The NMP-derived V2a neurons, for example, displayed enrichment in transcription factor motifs associated with homeodomain-containing transcription factors, which are critical for regionalization and spinal cord identity. Conversely, NEP-derived neurons showed a broader distribution of bHLH and Rel homology motifs, consistent with a hindbrain-like identity. This discovery underscores the impact of progenitor origin on the epigenetic landscape, potentially guiding functional differentiation even within seemingly similar neuronal subtypes.

Functional assessments showed that NMP-derived V2a neurons displayed more rapid establishment of synchronous network activity compared to their NEP counterparts. This increased network activity may reflect differences in axonal connectivity or intrinsic excitability, which could influence their suitability in regenerative therapies targeting motor or sensory circuits. These functional differences highlight the importance of considering progenitor origin in therapeutic applications, where specific activity profiles may be desirable.

Future functional studies should explore *in vivo* validation of NEP and NMP-derived neurons to assess circuit integration and functional synaptic integration post-transplantation.

Additionally, our computational analysis identified CREB5 and TCF7L2 as potential regulators of NMP-specific gene networks in V2a neurons, warranting further investigation into their role in modulating neurodevelopmental pathways. These insights may aid in the development of improved differentiation protocols for generating functionally specialized V2a neurons.

Our experiments with induced VSX2-expressing neurons, which bypassed key developmental patterning stages, yielded cells that displayed some superficial characteristics of V2a neurons but differed significantly in transcriptional identity. The axial identity of these induced neurons remained labile, indicating that essential developmental cues are necessary to establish and maintain regional specificity. These findings are consistent with previous studies showing that induced neurons often lack the stable chromatin modifications characteristic of lineage-specific differentiation. Our results suggest that induced neurons may not fully replicate the gene regulatory networks of authentic V2a neurons, raising concerns about their applicability in disease modeling and therapeutic discovery where functional specificity is critical. Future studies using *in silico* GRN modeling and perturbation could identify additional transcription factors that can be overexpressed to enhance the fidelity of induced V2a neurons. By pinpointing key regulators that drive lineage-specific traits, this approach could provide insights into constructing more stable and functionally accurate V2a neuron populations, ultimately improving their utility in disease models and therapeutic applications.

In summary, our study establishes a foundational framework that extends beyond the specific context of V2a neurons, underscoring the importance of refining hPSC differentiation strategies. Our findings emphasize the necessity of generating cells that not only express key lineage markers but also faithfully replicate the developmental stages and processes encountered during fetal development. Enhancing the specificity and accuracy of differentiations will enable more precise and diverse basic and translational applications.

Limitations of the study

Our study design enables us to isolate the effects of NEP and NMP progenitor lineages on V2a neurons; however, our multiomic analysis captures only a single time point. While we observe population heterogeneity and can separate p2 populations for pseudotemporal analysis, we cannot conclusively determine whether lineage identity is retained over time. snATAC-seq reveals enriched motifs in specific populations, but experiments such as ChIP-seq are needed to pinpoint TF binding at specific loci. Although we observed distinct activity patterns between maturing NEP and NMP cultures, these findings are confounded by mixed populations. Variations in motor and interneuron proportions may influence burst activity, necessitating targeted drug perturbations or sorted cultures to resolve these effects.

Figures

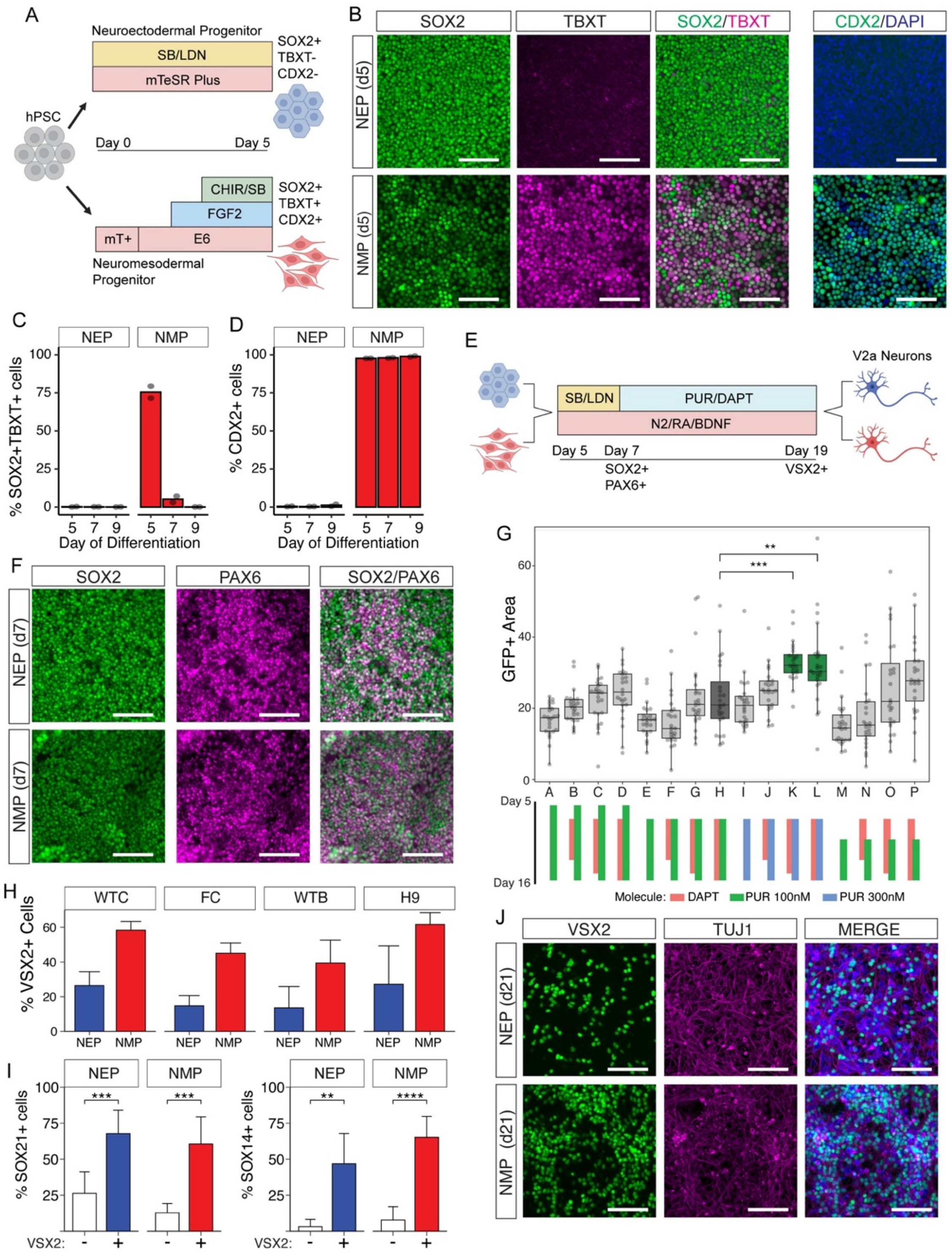

Figure 3.1. Generation of V2a neurons from distinct progenitor lineages.
(Figure caption continued on the next page.)

(Figure caption continued from the previous page.)
A. Schematic of the first five days of differentiation from human pluripotent stem cells toward neural progenitors under defined media conditions with expected marker gene expression. Abbreviations: SB = SB431542, LDN = LDN193189, CHIR = CHIR99021, E6= Essential 6, mT+ = mTeSR Plus.
B. Representative expression of neuromesodermal progenitor population markers SOX2, TBXT, and CDX2 at day 5 of differentiation in the neuroectodermal and neuromesodermal routes (top and bottom rows, respectively). Note the overlap of SOX2 and TBXT expression in the NMP condition. Scale bars represent 100 um.
C. Flow cytometry quantification of the percent of cells coexpressing NMP markers SOX2 and TBXT in both progenitor populations at days 5, 7, and 9 of differentiation. n = 2 biological replicates.
D. Flow cytometry quantification of the percent of cells expressing NMP marker CDX2 in both progenitor populations at days 5, 7 and 9 of differentiation. n = 2 biological replicates.
E. Schematic of the differentiation of distinct progenitor lineages toward V2a neurons under identical defined media conditions from day 5 to day 19 of differentiation with expected marker gene expression. Abbreviations: SB = SB431542, LDN = LDN193189, PUR = purmorphamine, RA = retinoic acid.
F. Representative expression of SOX2 and PAX6 in the NEP and NMP conditions (top and bottom rows, respectively) at day 7 of differentiation. Scale bars represent 100 um.
G. Differentiation optimization using the FOXN4:Cre reporter line. Boxplots show the percent of the GFP+ area, as reported by FOXN4:Cre expression, under modified addition of PUR and DAPT between days 5 and 16 of differentiation as indicated by the colored bars (bottom). H (dark gray) represents prior published conditions. K,L (green) show significantly increased GFP+ area with 300 nM PUR. Condition L was selected for further experiments. Abbreviations: PUR = purmorphamine.
H. Flow cytometry quantification of the percent of VSX2+ cells in dissociated cultures at day 19 of differentiation from either NEP or NMP lineages in four human stem cell lines. Abbreviations: WTC = WTC11, FC = FOXN4:Cre. n >=2 biological replicates. Error bars represent standard deviation.
I. Flow cytometry quantification of the percent of SOX21+ or SOX14+ cells in both VSX2 positive and negative populations at day 19 of differentiation. n = 7 biological replicates. ** is $p<0.01$, *** is $p<0.001$, **** is $p<0.0001$, error bars represent standard deviation.
J. Representative expression of VSX2 and TUJ1 in NEP and NMP-derived neurons at day 21, two days after replating. Scale bars represent 100 um.

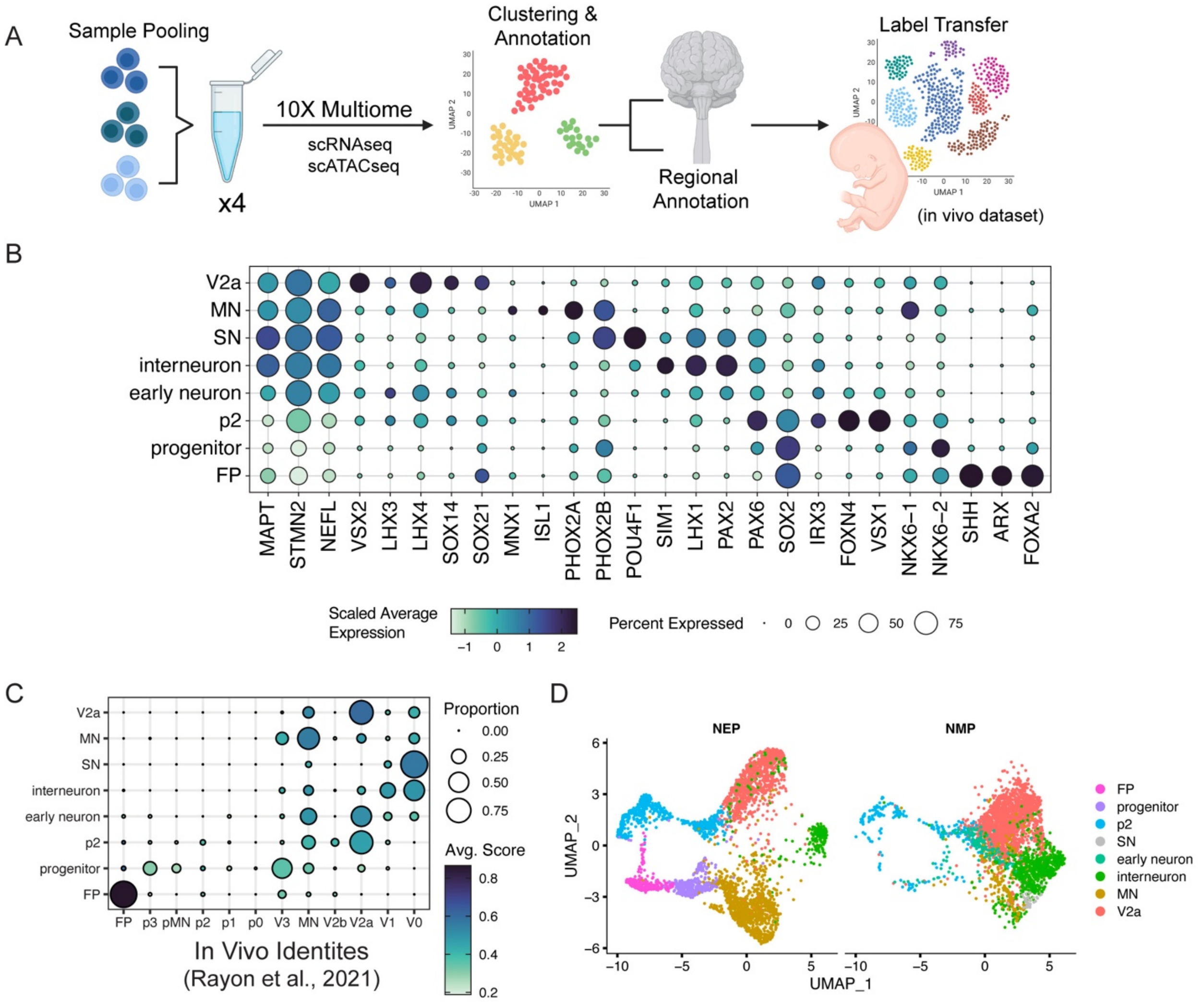

Figure 3.2. Distinct progenitor lineages recapitulate the cellular diversity of primary human neural tube.
A. Schematic of sample pooling for multiome and cell annotation steps.
B. Expression of selected marker genes for the 8 annotated cell types in a merged object of all of multiome samples.
C. Results of an unbiased label transfer of multiome samples onto ventral human fetal spinal cord cells.
D. UMAP of annotated multiome samples after Harmony integration.

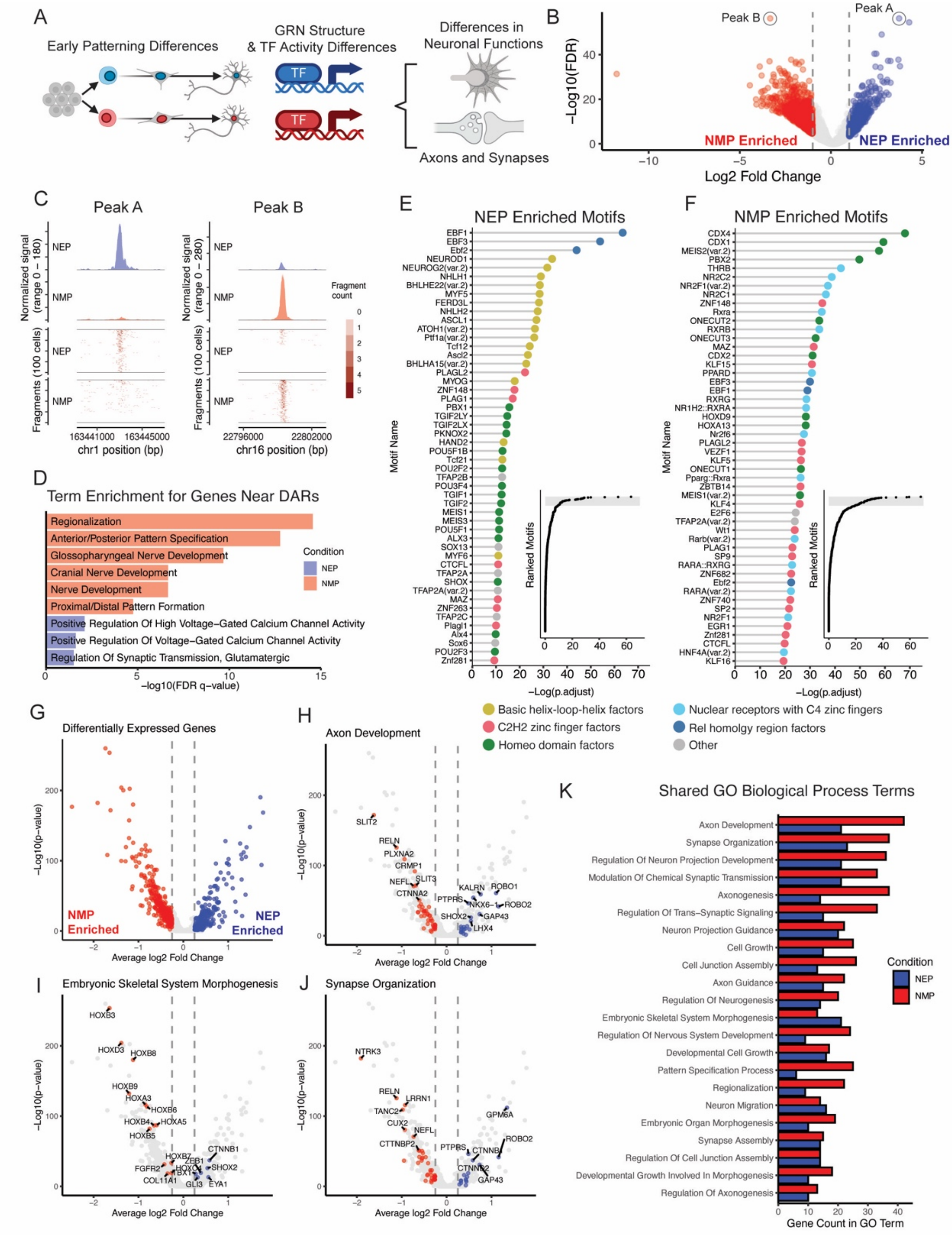

Figure 3.3. Progenitor lineage confers distinct transcription factor binding motifs and gene expression.
(Figure caption continued on the next page.)

(Figure caption continued from the previous page.)
A. Simplified schematic of the V2a differentiation and differences that could be identified using multiomic data.
B. Volcano plot showing differentially accessible regions of chromatin (DAR) between NEP- and NMP-derived V2a neurons in snATAC-seq data. Blue points (positive log2 fold change) are peaks enriched in NEP samples. Red points (negative log2 fold change) are peaks enriched in NMP samples.
C. Coverage plot depicting example peaks specific to either NEP or NMP conditions (left and right, respectively). Regions are represented as either normalized histograms or fragment count heatmaps per 100 cells (top and bottom, respectively). Shown peaks are also highlighted in B.
D. Selected significantly upregulated gene ontology terms for NEP or NMP-specific DARs using Genomic Regions Enrichment of Annotations Tool (GREAT).
E,F. Top 50 most enriched transcription factor motifs in NEP (left) or NMP-specific (right) DARs as identified in B. Each transcription factor motif is colored according to the class of transcription factor to which it belongs. Inset: ranked enrichment scores for all tested motifs, shaded gray region represents top 50 shown in the main figure.
G. Volcano plot showing differentially expressed genes between NEP and NMP-derived V2a neurons in snRNA-seq data. Blue points (positive log2 fold change) are enriched in NE samples. Red points (negative log2 fold change) are enriched in NMP samples.
H-J. Differentially expressed genes which belong to the indicated gene ontology (GO) term. In all cases, the GO term is significantly enriched in both NEP and NMP conditions.
K. Shared significantly enriched GO Biological Process terms identified in the differentially expressed genes between NEP and NMP-derived V2a neurons. Bars represent the number of genes annotated to each respective GOBP term in each gene set.

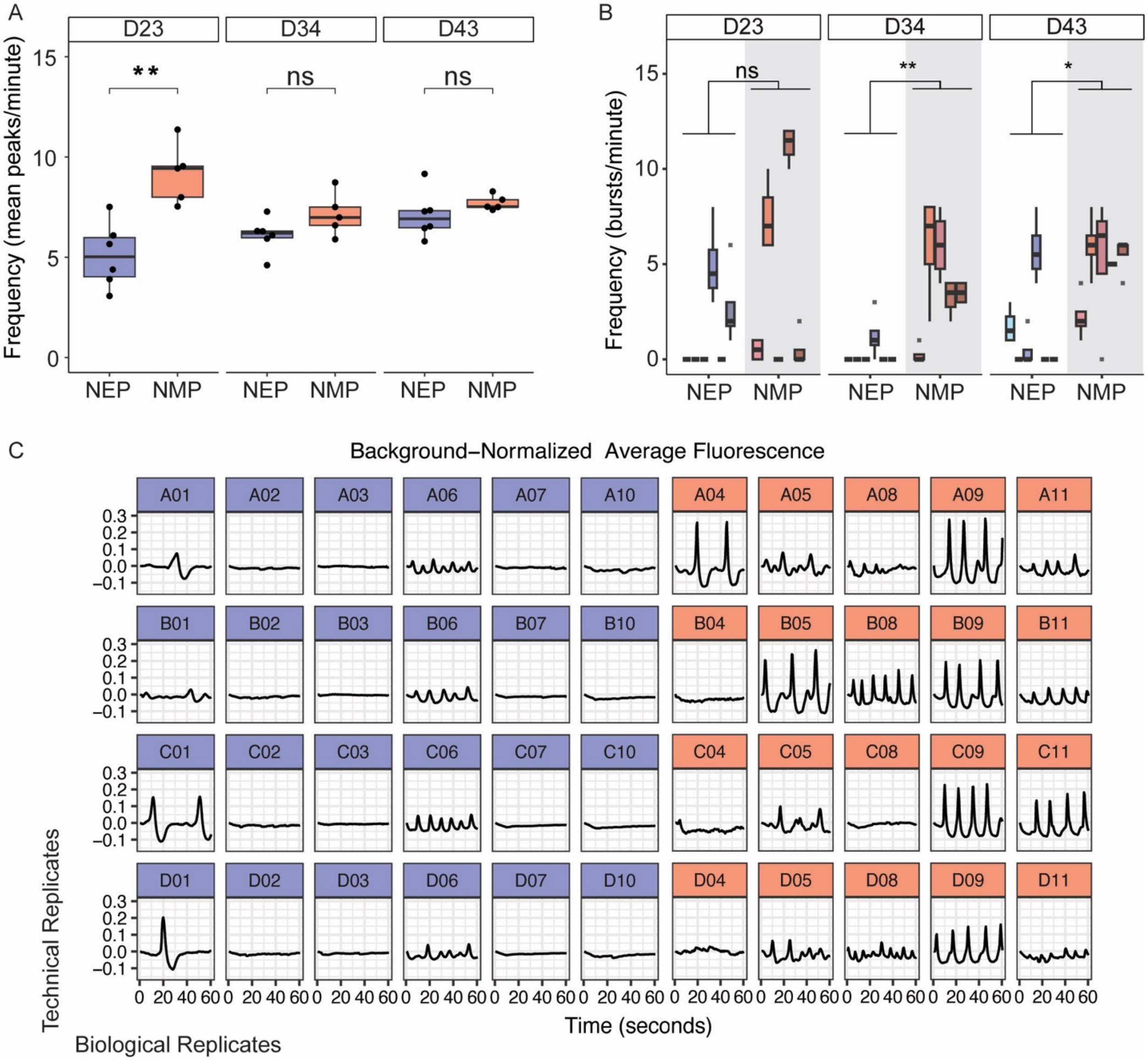

Figure 3.4. NMP-derived neurons generate robust synchronous activity in maturing cultures.
A. Mean number of peaks per region of interest (ROI) captured by Fluo4-AM calcium imaging in replated V2a cultures at indicated time points. Each point represents the average of 4 technical replicates with n >= 5 biological replicates. ** is $p<0.01$ by Student's t-test.
B. The number of synchronous bursts per well captured by Fluo4-AM calcium imaging in replated V2a cultures at indicated time points. n >= 5 biological replicates with 4 technical replicates, each. For statistical comparison, technical replicates were collapsed to their means and compared by the Mann-Whitney U test. * is $p<0.05$, ** is $p<0.01$.
C. Line graphs of background-normalized average fluorescence in each well of the data represented in Figure 4B day 43. NEP samples in blue, NMP samples in red. Columns and rows are biological and technical replicates, respectively.

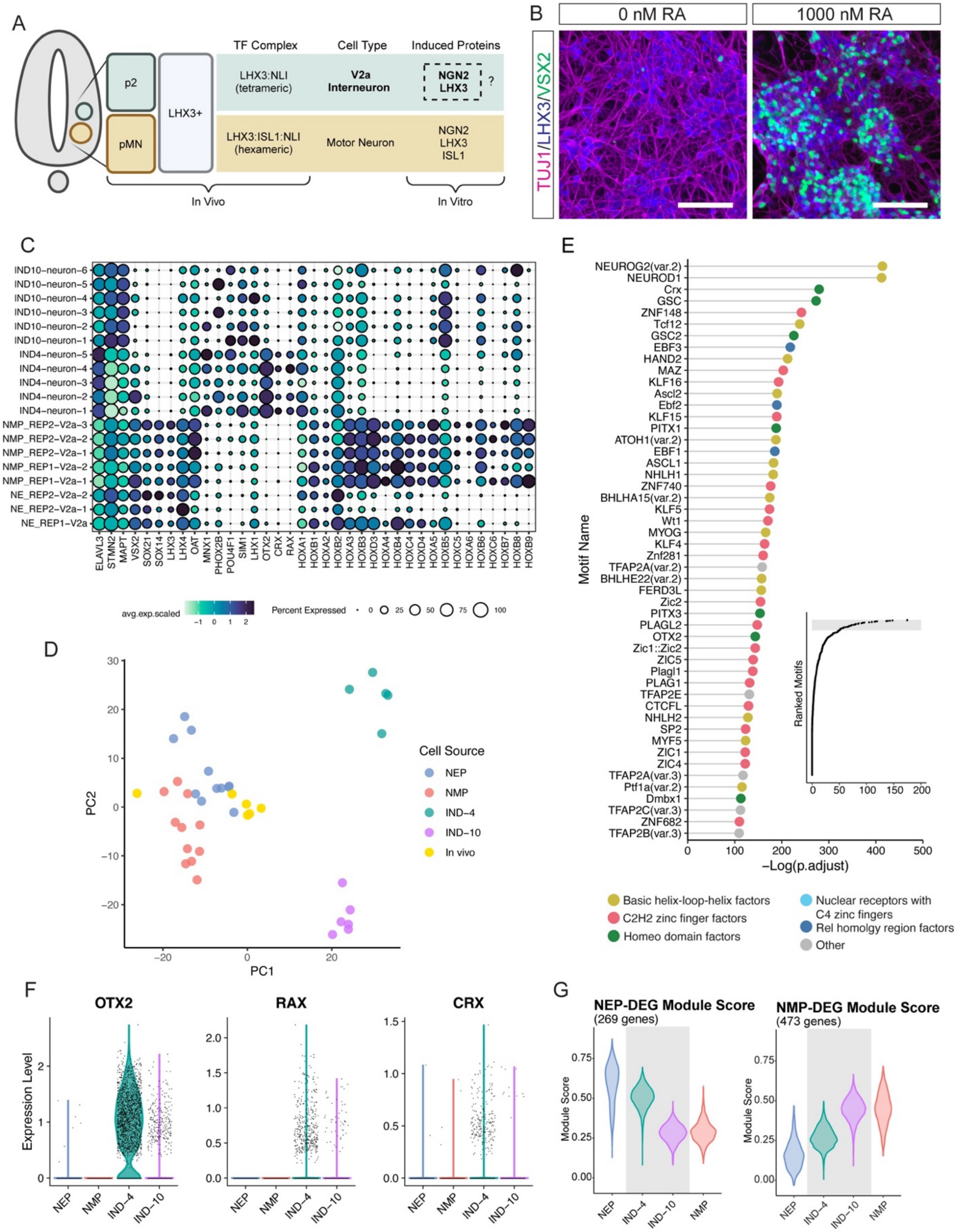

Figure 3.5. Induced neurons express anterior CNS markers and fail to recapitulate *in vivo* neural identities.
(Figure caption continued on the next page.)

(Figure caption continued from the previous page.)
A. Schematic of developing neural tube and the transcription factor complexes that refine V2a and motor neuron fates *in vivo*, as well as the existing and proposed transcription factor combinations to be used *in vitro*.
B. Representative staining of NGN2::LHX3 induced neurons after 4 days of dox addition with either 0 nM or 1000 nM RA. LHX3 (blue) shows induced protein expression, TUJ1 (magenta) shows neural morphology, VSX2 (green) is a marker of V2a neurons. Scale bar represents 100 um.
C. Comparison of NEP and NMP V2a clusters with day 4 and day 10 induced neurons. Marker genes include pan neural genes, V2a genes, off-target genes, and axial markers.
D. PCA of pseudubulked clusters of NEP, NMP, *in vivo*, and day 4 and day 10 induced neurons.
E. Top most significantly enriched motifs in differentially accessible regions of chromatin specific to day 4 induced neurons compared to NE and NMP V2a neurons. Each transcription factor motif is colored according to the class of transcription factor to which it belongs. Inset: ranked enrichment scores for all tested motifs, shaded gray region represents top 50 shown in the main figure.
F. Expression of anterior markers OTX2, RAX, and CRX across differentiation conditions.
G. Module scores of indicated populations of neurons using modules composed of the differentially expressed genes specific to either the NEP or NMP V2a populations as in Figure 3G.

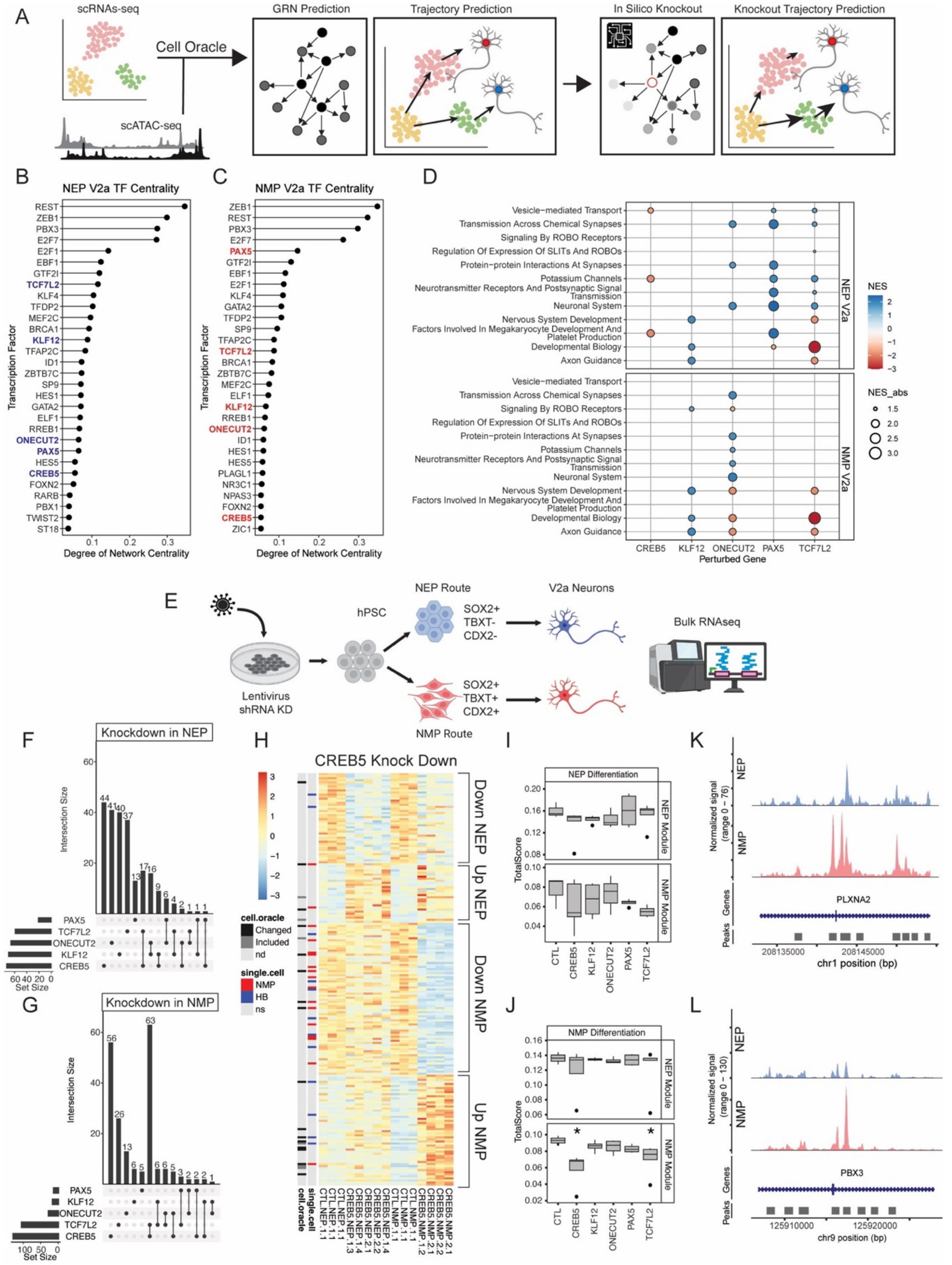

Figure 3.6. CREB5 and TCF7L2 regulate an NMP-enriched V2a gene signature.
(Figure caption continued on the next page.)

(Figure caption continued from the previous page.)
A. Schematic of the CellOracle pipeline. Single nucleus RNA- and ATAC-seq datasets are incorporated to generate predicted gene regulatory network (GRN) and map default trajectories. Specific nodes of the GRN can then be computationally ‘knocked-out’ and the effects propagated throughout the regulatory network. These effects can also be visualized as differences in the vectorized trajectory of cell populations.
B,C. Top 30 transcription factors ranked by network centrality score in the predicted GRNs for both NEP and NMP V2a neurons, respectively. Highlighted genes were selected for further validation.
D. Gene set enrichment analysis (GSEA) in NEP and NMP V2a neurons after *in silico* gene perturbation (knockout). Shown are the normalized enrichment scores (NES) for selected gene sets.
E. Schematic showing validation experiments using lentiviral knockdown of selected targets.
F. Upset plot depicting the number and overlap of differentially expressed genes between control and knockdown of the indicated gene under NEP differentiation conditions.
G. Upset plot depicting the number and overlap of differentially expressed genes between control and knockdown of the indicated gene under NMP differentiation conditions.
H. Heatmap depicting the significantly differentially expressed genes in the CREB5 KD condition across both NEP and NMP differentiations.
I. Boxplots of single sample GSEA scored only on NEP condition knockdown samples using the differentially expressed genes between NEP and NMP V2a neurons as indicated modules. No sample is significantly different from the control condition by Student’s t-test.
J. Boxplots of single sample GSEA scored only on NMP condition knockdown samples using the differentially expressed genes between NEP and NMP V2a neurons as indicated modules. The NE module is not significantly changed in any knockdown sample, but both CREB5 and TCF7L2 knockdown samples score significantly lower in the NMP module than controls. * is $p < 0.05$ by Student’s t-test.
K,L. Coverage plots centered on differentially accessible regions enriched in the NMP condition which are located within genes (PLXNA2 and PBX3, respectively) which are significantly downregulated with NMP CREB5 KD samples.

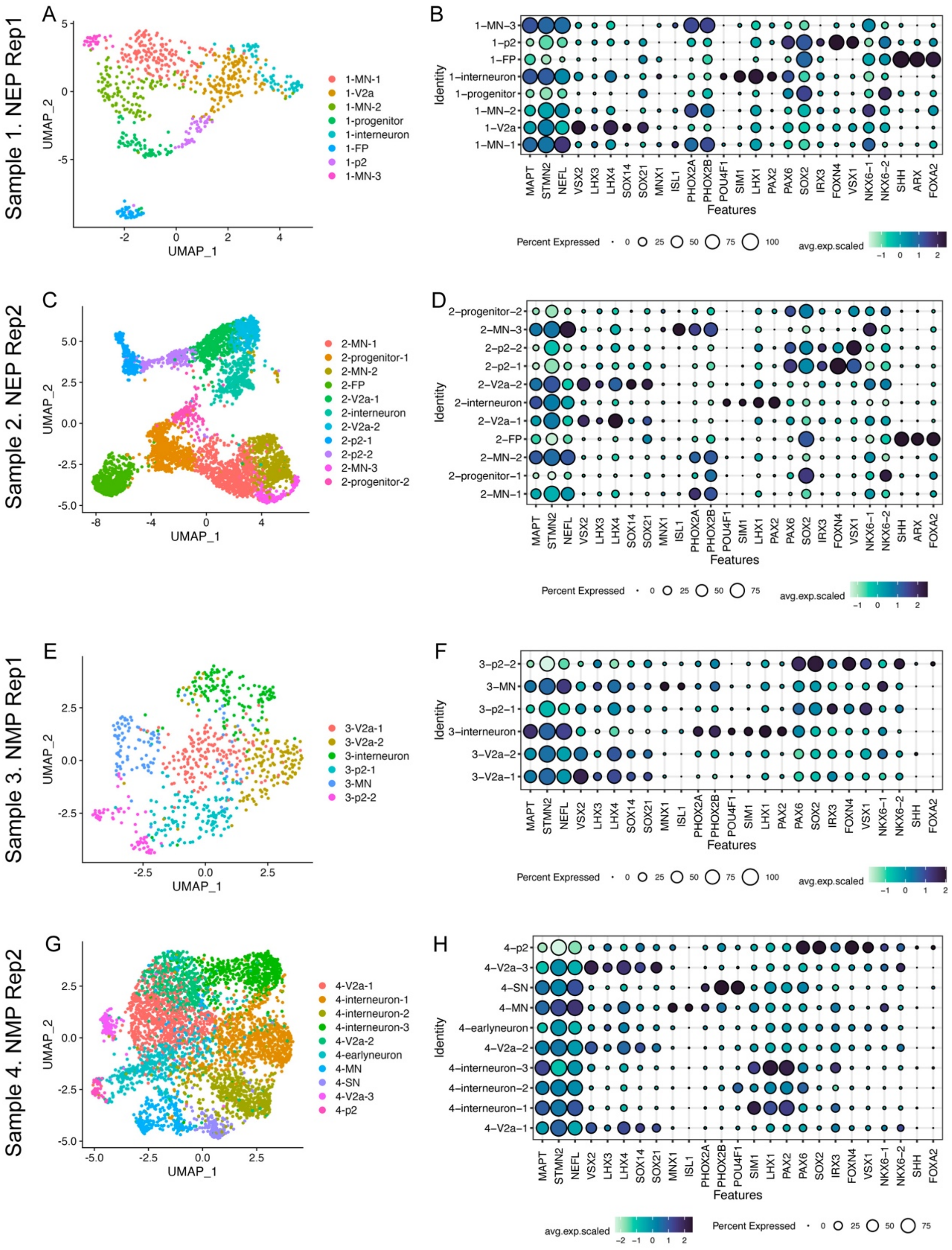

Figure 3.S1. Individual sample clustering and cell annotation by marker gene sets.
A, C, E, G. UMAP plots of the indicated sample with clusters identified using resolution = 0.8.
B, D, F, H. Dot plots showing the expression of marker gene sets used to classify cell types within the indicated sample.

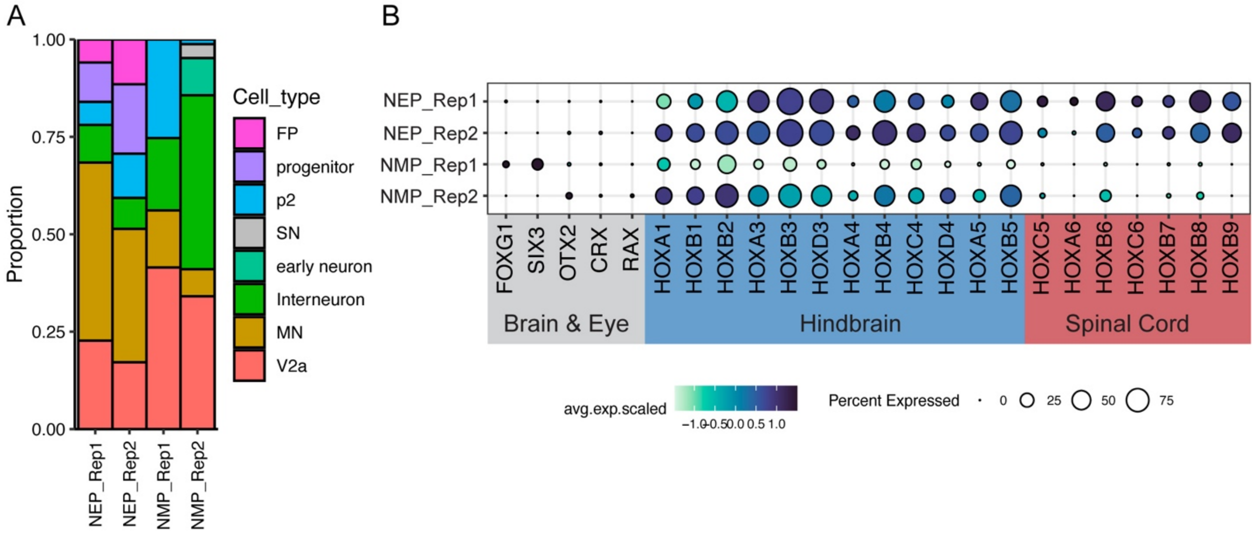

Figure 3.S2. Characterization of population proportion and axial identity in multiome samples.
A. Expression of anterior-posterior axial markers in each multiome sample. Colored groups of genes indicate approximate anatomical boundaries.
B. Bar plot showing the proportion of each annotated cell type for each multiome sample.

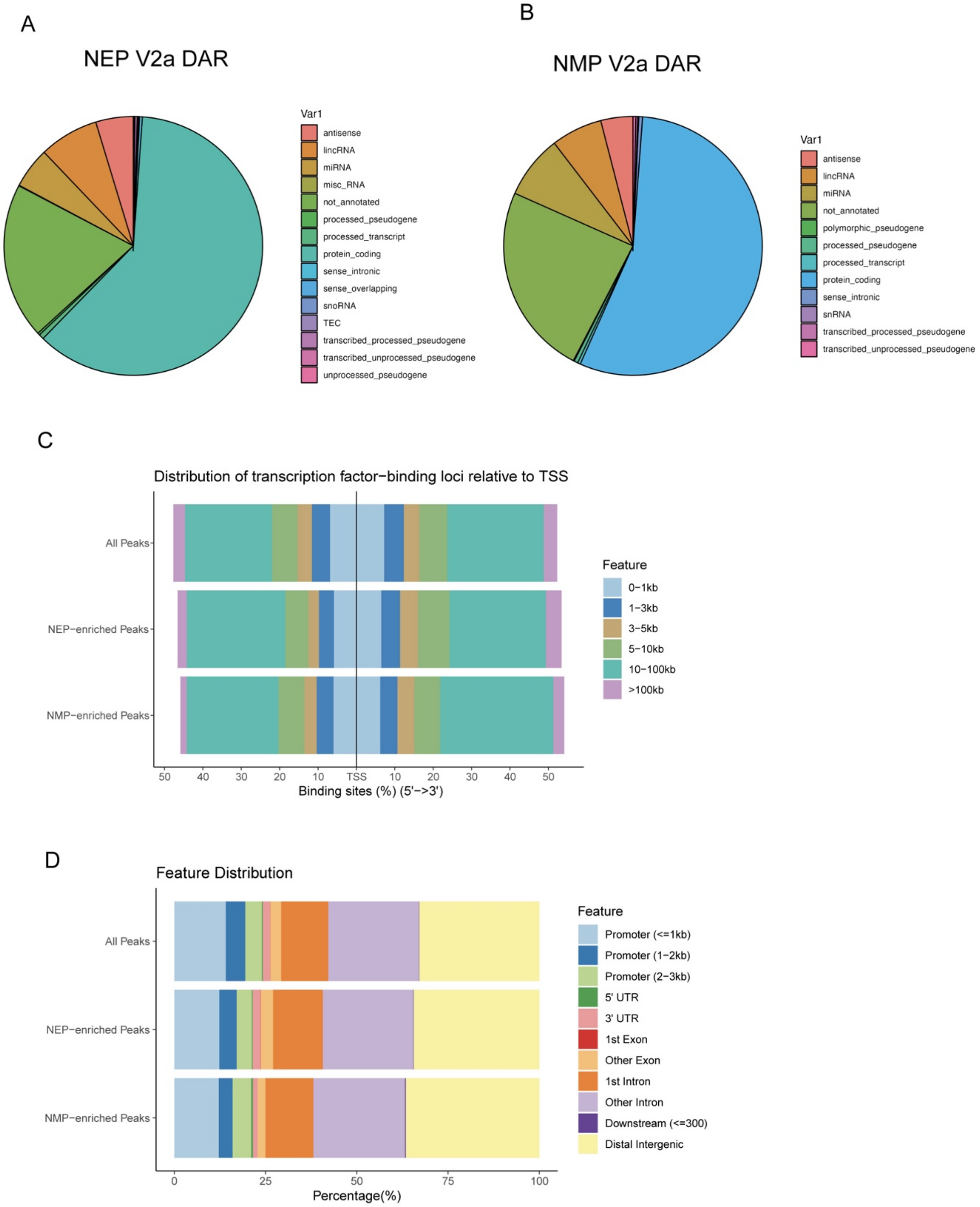

Figure 3.S3. Similarities in the annotation and relative location of differentially accessible ATAC peaks between NEP and NMP V2a neurons.

A, B. Pie chart of the gene type annotation for the gene with the nearest TSS to differentially accessible chromatin peaks between NEP and NMP-derived V2a neurons.

C. Bar plot showing the distribution of differentially accessible peaks between NEP and NMP V2a neurons.

D. Bar plot showing the relative location of differentially accessible peaks within genes between NEP and NMP V2a neurons

A. GREAT analysis, NEP V2a over background peaks, GO Biological Process (all)

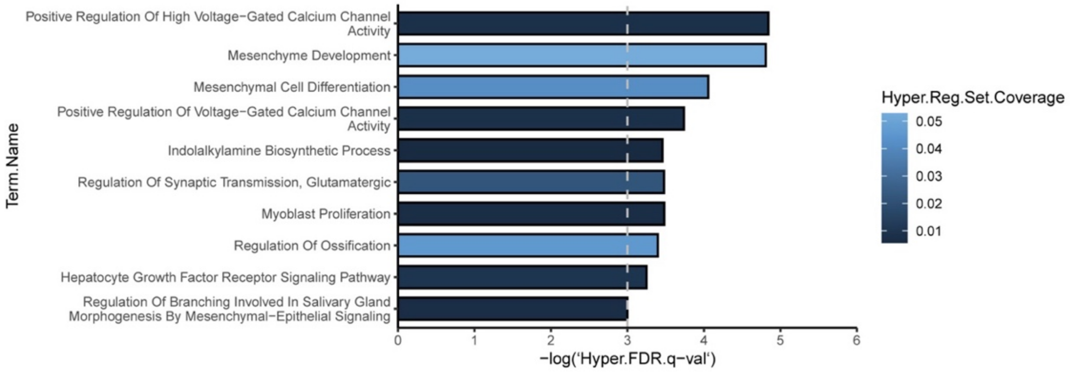

B. GREAT analysis, NMP V2a over background peaks, GO Biological Process (top 10)

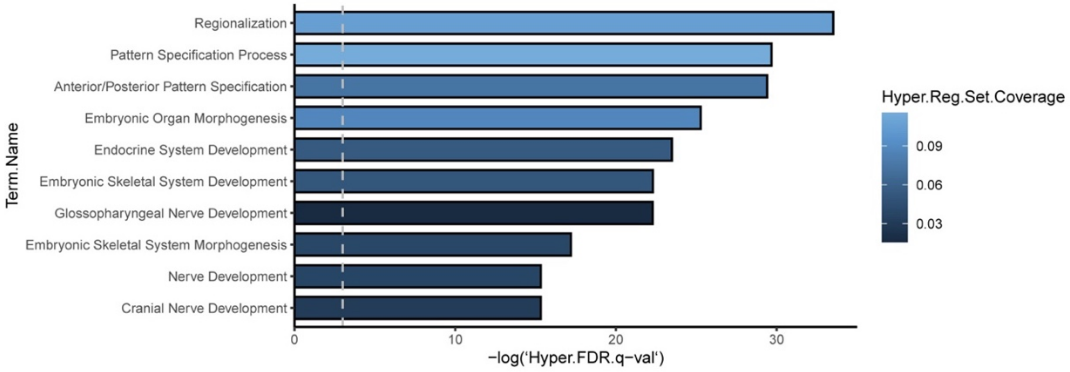

C. GREAT analysis, NMP V2a over background peaks, GO Molecular Function (top 10)

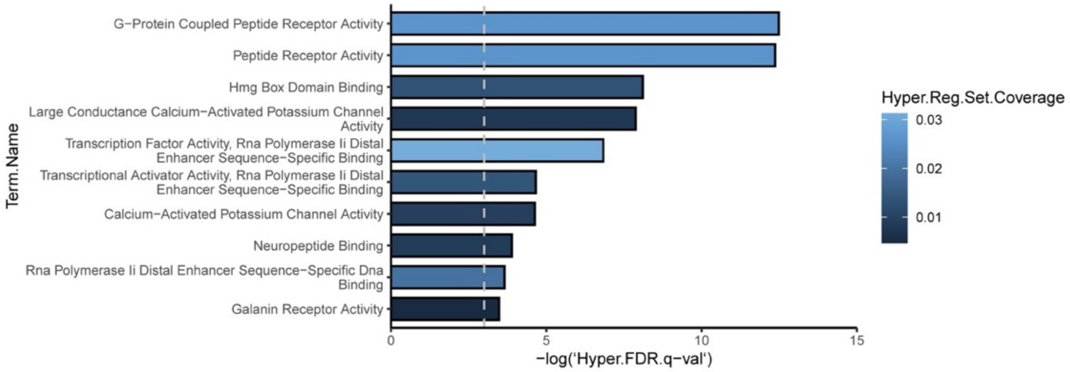

Figure 3.S4. Enrichment of Gene Ontology terms for the genes near ATAC peaks.
A. GREAT Analysis showing all significantly enriched biological process GO terms for the genes near NEP-enriched peaks. Dashed grey line is significance threshold.
B. GREAT analysis showing the top 10 significantly enriched biological process GO terms for the genes near NMP-enriched peaks. Dashed grey line is significance threshold.
C. GREAT analysis showing the top 10 significantly enriched molecular function GO terms for the genes near NMP-enriched peaks. Dashed grey line is significance threshold.

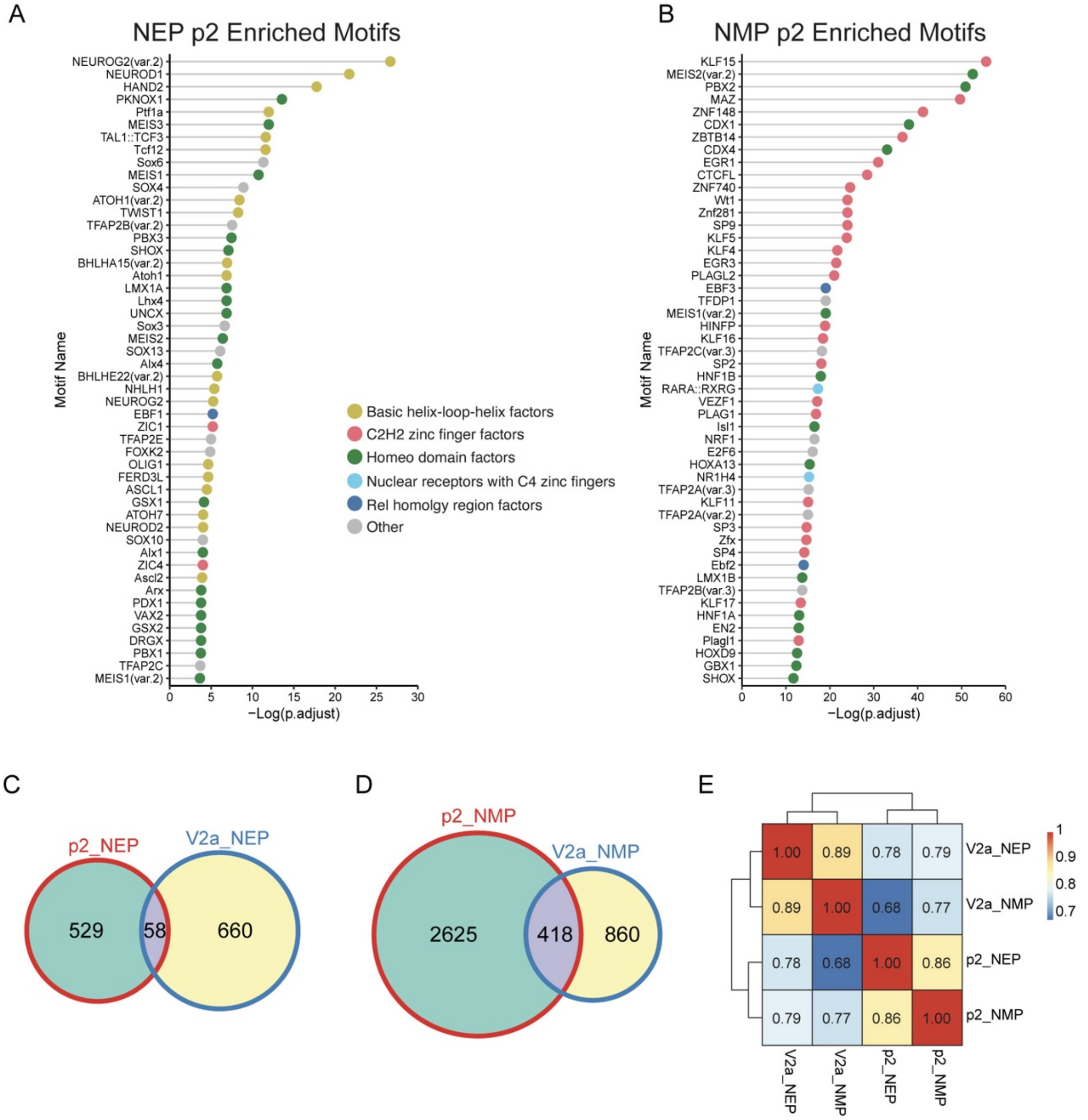

Figure 3.S5. Lineally distinct p2 progenitors possess enriched transcription factor motifs similar to V2a but limited overlap in lineage specific ATAC peaks.

A. Top 50 most enriched transcription factor motifs in NEP p2 DARs. Each motif is colored by transcription factor class.

B. Top 50 most enriched transcription factor motifs in NMP p2 DARs. Each motif is colored by transcription factor class.

C. Venn diagram of the DARs found in both the p2 and V2a cells from the NEP condition

D. Venn diagram of the DARs found in both the p2 and V2a cells from the NMP condition

E. Pearson diagram showing the global similarity of ATAC peaks between p2 and V2a populations.

A. NEP (C10 d43)

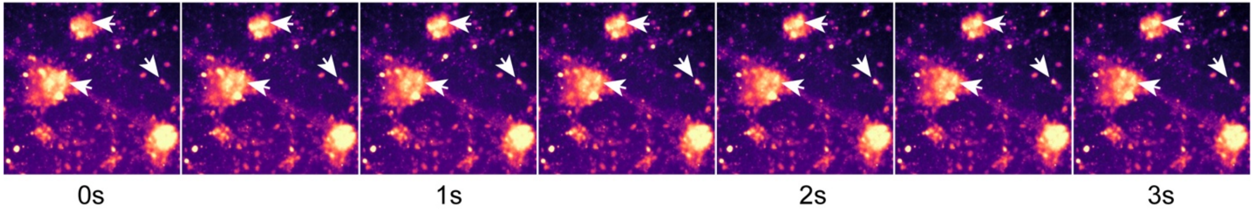

B. NMP (C09 d43)

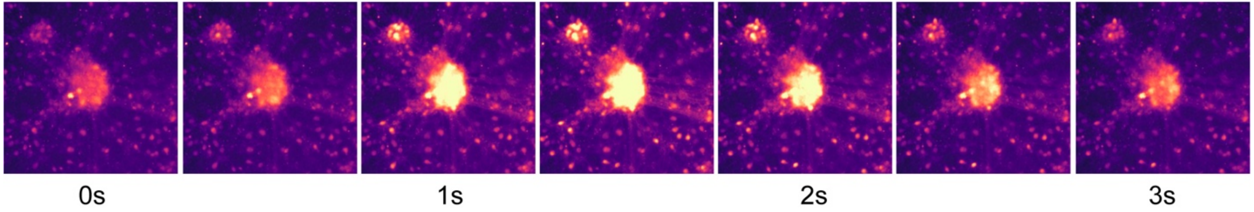

Figure 3.S6. Representative stills of neural activity from calcium imaging videos.
A. Representative images from a d43 NEP-derived neuron culture calcium imaging video. Arrow heads point to regions with fluorescent activity.
B. Representative images from a d43 NMP-derived neuron culture calcium imaging video. Panels show a synchronous burst of activity across the population.

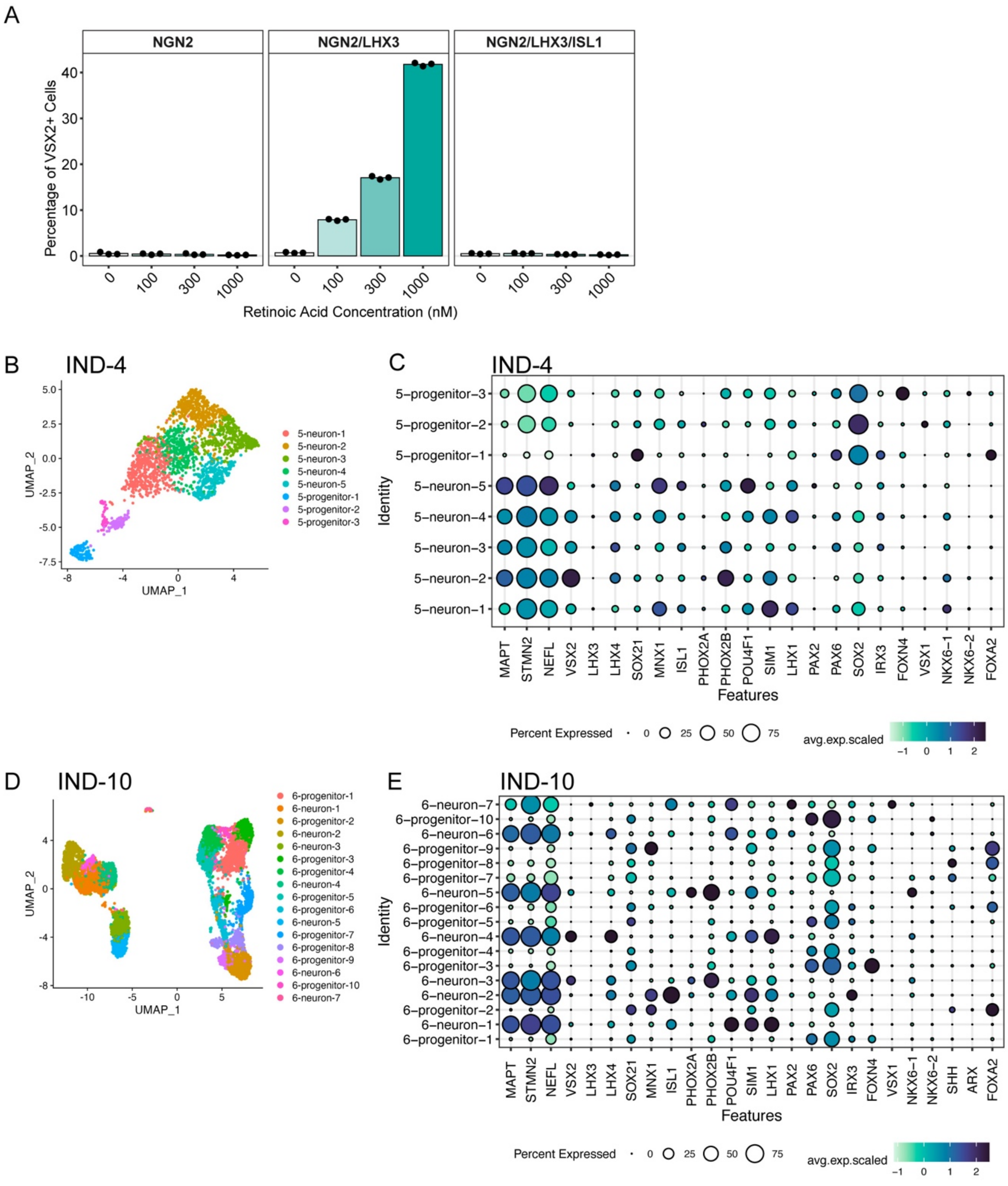

Figure 3.S7. Marker gene expression in induced neurons.

A. Flow cytometry quantification of VSX2 expression in induced neuron populations under graded concentration of retinoic acid (RA). The specific combination of transcription factors is shown at the top of each panel. n = 3 technical replicates.

B. UMAP of day 4 induced neurons.

C. Marker gene expression in clusters identified in day 4 induced neurons

D. UMAP of day 10 induced neurons.

E. Marker gene expression in clusters identified in day 10 induced neurons.

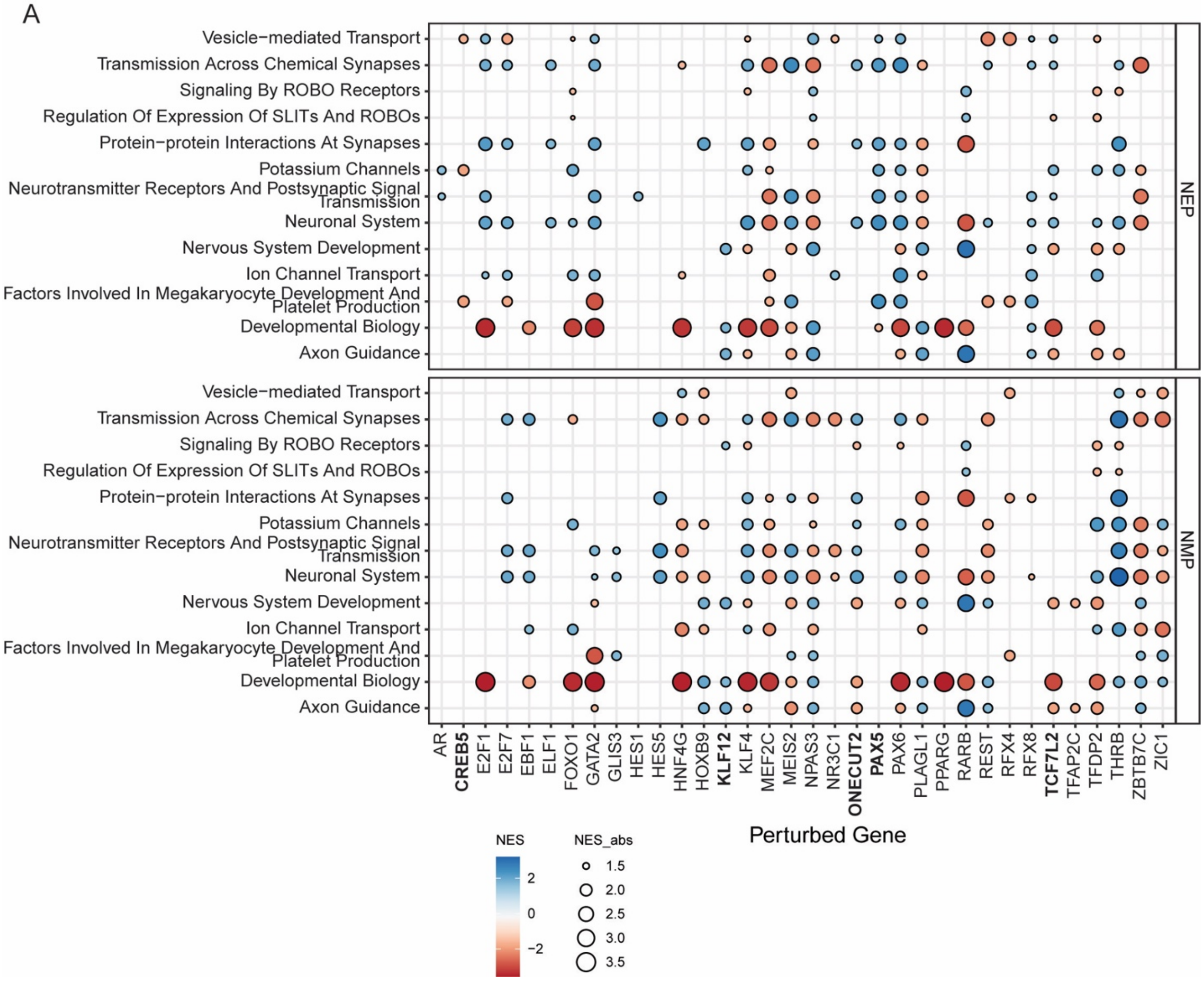

Figure 3.S8. GSEA in distinct V2a populations after *in silico* knockout of highly central transcription factors.

A. GSEA normalized enrichment scores for selected gene sets after predicting CellOracle gene knockout effects in both NEP and NMP V2a neurons. Target genes for CellOracle knockout are from the most central genes in the predicted V2a gene regulatory networks.

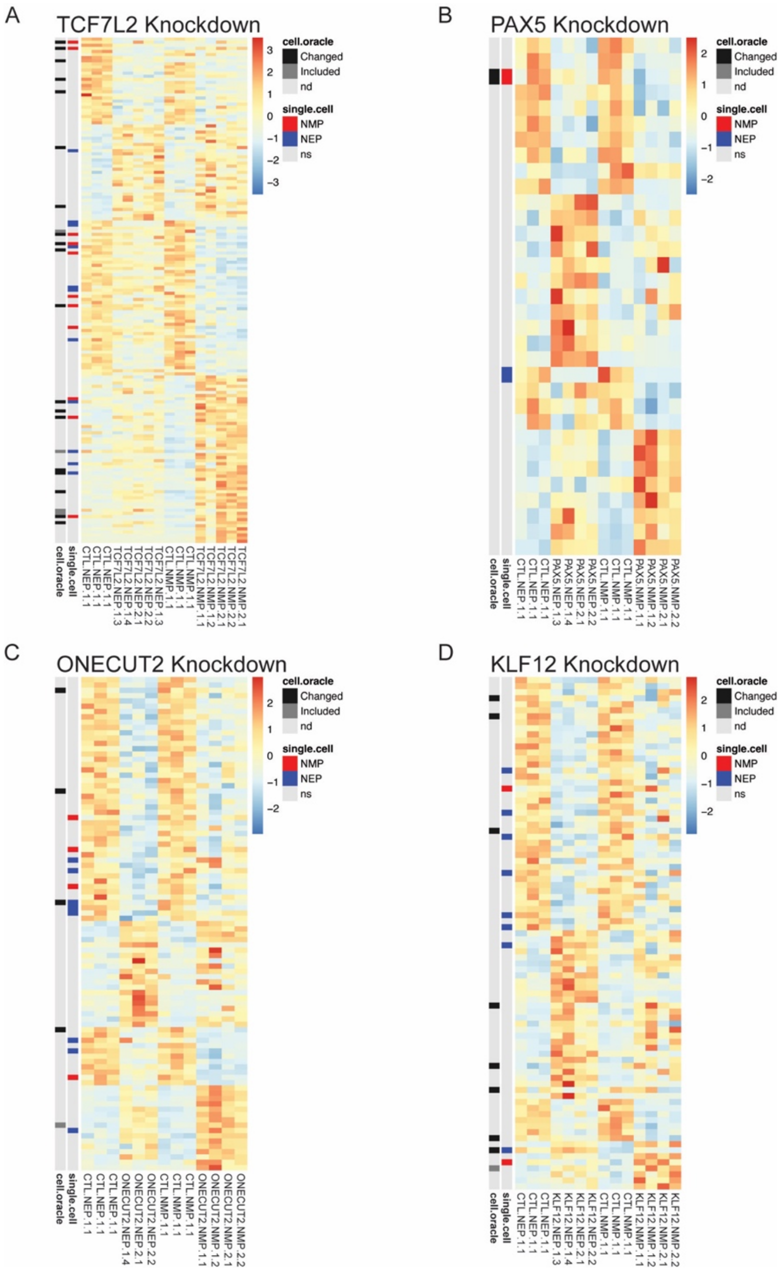

Figure 3.S9. Differential gene expression resulting from transcription factor knockdown in NEP and NMP differentiations.

A. Heatmap depicting the significantly differentially expressed genes in the TCF7L2 KD condition across both NEP and NMP differentiations.

B. Heatmap depicting the significantly differentially expressed genes in the PAX5 KD condition across both NEP and NMP differentiations.

C. Heatmap depicting the significantly differentially expressed genes in the ONECUT2 KD condition across both NEP and NMP differentiations.

D. Heatmap depicting the significantly differentially expressed genes in the KLF12 KD condition across both NEP and NMP differentiations.

Materials and Methods

Stem cell maintenance

The parental stem cell lines used in this study include WA09 (WiCell), WTC11 (Coriell Institute), and WTB lines (Conklin Lab; Miyaoka et al., 2014). Stem cells were seeded on Geltrex coated plates and maintained in mTeSR1 with daily feeds or in mTeSR Plus and fed every other day and kept at 37°C and 5% CO2. Stem cells were passaged at ~70% confluency using Accutase at a 1:10 ratio. A defined pro-survival small molecule cocktail, CET, was included in the media for the first 24 hours after passaging (Chen et al., 2021). All stem cell lines were tested quarterly for mycoplasma.

Generation of the FOXN4:GFP reporter line

The FOXN4:Cre cell line was built into the WTC-hNIL transgenic iPSC line (previously described in Shi et al., 2018; Fernandopulle et al., 2018). First, a lox-STOP-lox reporter cassette called XR1(Addgene plasmid #129111; a gift from Bruce Conklin) was integrated into the CLYBL safe harbor locus using locus-specific TALEN (Addgene plasmid #62196 and #62197; gifts from Jizhong Zou). Donor and TALEN plasmids were nucleofected into WTC-hNIL stem cells using the P3 Primary Cell 4D Nucleofector X Kit (Lonza). Cells were then selected for with G418 and integration was confirmed using junction PCR (Supplemental Table 3). Excision of the lox-STOP-lox cassette was tested using CRISPR-mediated activation of the reporter by excision of the terminator using combinations of 5 RNA guides targeting each side of the cassette (L1-5, R1-5; Supplemental Table 3). We next made a donor plasmid for integration of a P2A-cleaved Cre in-frame with the endogenous FOXN4 locus. The donor plasmid contained a pCAGG::mCherry integration reporter for non-antibiotic selection which could be removed by CRISPR/Cas9 using flanking tia1L guide sites (Roberts et al., 2019, fragments taken from AICSDP-45: TTN-mEGFP, a gift from Allen Institute for Cell Science; Addgene # 114412). A homology region of ~2kb in length surrounding the FOXN4 stop codon was amplified using PCR for HDR targeting (Supplemental

Table 4). FOXN4:Cre donor plasmid was nucleofected into XR1-containing stem cells along with Cas9 complexed with a single-guide RNA (ACAGCUCAAAGCAGGGCUAU; Synthego). After recovery and expansion, mCherry+ clones were hand-picked and confirmed with junction PCR. To remove the mCherry selection cassette, tia1L sgRNA (GGUAUGUCGGGAACCUCUCC, Synthego) and Cas9 were added using Lipofectamine Stem to mCherry+ cultures. After one passage, mCherry- cells (~30% of the population) were sorted on a FACS Aria Fusion, recovered, expanded, and cryopreserved.

Neuromesodermal progenitor differentiation

Neuromesodermal progenitor (NMP) differentiation loosely followed the protocol set out in Lippmann et al. (2015). Briefly, stem cells were passaged as normal in 6-well plates and allowed to grow to ~70% confluency in mTeSR Plus. To begin differentiation, cells were then fed with 4 mL/well E6 media. One day later, cells were fed with 4 mL/well E6 with 20 ng/mL bFGF. Following 24-hours of FGF treatment, at which point cells were 100% confluent, cells were washed 1x with PBS and dissociated using 1.5 mL/well of Accutase in the incubator for ~10 minutes. Dissociated cells were collected, washed, and spun at 1200 rpm for 2 minutes. For each well that was dissociated, cells were resuspended in 12 mL of E6 media containing 1x CET, 10 uM SB 435142 (SB), 20 ng/mL bFGF, and 3-5 uM CHIR99021 (CHIR). Note, the CHIR dose should be adjusted for each cell line; WTC-11 and derivative cell lines require 3 uM CHIR, while WTB and H9 require 5 uM CHIR. Cells were plated into Geltrex-coated 24-well plates using 0.8 mL of cell suspension per well. 48-hours later, cells had a cobble-stone appearance covering 100% of the well, and were either collected to assess NMP identity or immediately transitioned into day 5 differentiation media (see V2a differentiation below).

V2a differentiation

The NEP V2a differentiation followed the detailed protocol outlined in Butts et al. (2019) with minor modifications. To start differentiation (day 0), stem cell cultures at ~70% confluency were dissociated using Accutse, counted, and resuspended in mTeSR Plus with 1x CET, 10 uM SB, and 200 nM LDN 193189 (LDN) to a concentration of 100k cells/mL. 1 mL of cell suspension was plated into each well of Geltrex-coated 24-well plates, resulting in a final seeding density of ~50k cells/cm2. At days 1 and 3, cells were fed with 2 mL/well mTeSR Plus with 10 uM SB and 200 nM LDN. By day 5, cells were 100% confluent. From day 5 onward, the base media was changed to Neural Induction Media (NIM; DMEM:F12 containing 1x N2 supplement, 1x Glutagro, 1x NEAA, 1x PenStrep, 0.4 ug/mL ascorbic acid, and 2 ug/mL heparin). On day 5, cells were fed with 2 mL/well NIM with 100 nM retinoic acid, 10 ng/mL BDNF, 10 uM SB, and 200 nM LDN. Day 5 also marks the time point at which NMPs are transitioned into the neural differentiation. From day 7 to 19, cells were fed every other day with 2 mL/well of NIM with 100 nM retinoic acid, 10 ng/mL BDNF, 0.4 ug/mL ascorbic acid, 300 nM purmorphamine, and 1 uM DAPT.

V2a dissociation and cryopreservation

On day 19 of neuron differentiation, cultures were washed 1x with PBS then incubated for 20 min with 1 mL/well of Accutase. An additional 1 mL of PBS was then added to each well and neural cultures were broken up by smoothly pipetting up and down 10x. Dissociated cells were then pooled in a vessel containing an additional 24 mL of PBS (or an additional mL of PBS for every well being dissociated). Dissociated cells were distributed to 50 mL conicals and centrifuged at 1000 rpm for 3 minutes and supernatant was aspirated, being careful not to disturb the cell pellet. Cells were resuspended in 5-8 mL of NIM with 100 nM RA, 10 ng/mL BDNF, 300 nM PUR, 1 uM DAPT, and 1x CET. The cell suspension was passed through a 37 um filter and counted using an automated cell counter and Trypan dye. Each well of a 24-well plate should yield 3-4e6 cells. The cell concentration was then adjusted to ~8-10e6 cells/mL by adding additional supplemented NIM. Cells were then mixed in a 1:1 ratio with cell preservation media (80% FBS, 20% DMSO) and distributed into labeled cryovials. Prior to transfer to LN2 for long-term storage, cryovials were chilled in a -80C freezer in CoolCell (Corning) or Mr. Frosty (Thermo Fisher) containers to keep the cooling rate to -1°C per minute.

Flow Cytometry and FACS

Cells were dissociated as described above. Cells were spun for 2 min at 1200 RPM, then supernatant was aspirated and cells resuspended in 100 uL of PBS. Single cell suspensions were fixed using the FOXP3/Transcription factor kit (eBiosciences) following the manufacturer's protocol. Cells in the Perm Buffer were stored at 4°C until use. For staining, the desired volume of cells was transferred to a clean 1.5 mL tube and washed 1x with 500 uL of PBS containing 0.1% BSA. Cells were spun in a fixed angle centrifuge at 400 g for 1.5 minutes, then tubes were rotated 180° and spun again. Supernatant was aspirated leaving ~25 uL of liquid in the bottom of the tube to not disturb the cell pellet. Primary and secondary antibodies were diluted in FOXP3 kit Perm Buffer and cells were stained in 100 uL volume in the dark at room temp for 1 hr or overnight at 4°C. Cells were washed 2x with PBS/BSA between the primary and secondary antibody steps. For antibody product numbers and dilutions, see Supplemental Table 1. All flow cytometry was carried out on an Attune NxT. For live cell sorting, dissociated cells were resuspended in DMEM/F12 with 0.5 uM EDTA and 1x CET to a concentration of ~10e6 cells/mL. Cells were immediately sorted on a FACS Aria Fusion into the same media.

Immunostaining

For staining cells in plates, cells were fixed with 4% PFA at room temperature for 10 minutes, then washed 3x with PBS. Cells were blocked for 1hr at room temperature in PBS containing 5% normal donkey serum and 0.3% Triton X-100. Primary and secondary antibodies were diluted in PBS containing 1% BSA and 0.3% Triton X-100 and incubated at room temperature for 1 hr hour or overnight at 4°C, with 3x washes of PBS following each antibody incubation. For antibody product numbers and dilutions, see Supplemental Table 1.

Nuclei Isolation for 10X Multiome

For multiome, all samples had been previously cryopreserved. Samples were thawed, washed with 10 mL of NIM, resuspended in 0.5 mL of NIM with CET and counted using Trypan Blue dye to assess viability. For sample pooling, 333k cells from three technical replicates were pooled, and 500k cells were used for subsequent nuclei isolation. Nuclei isolation followed 10X Genomics Demonstrated Protocol CG000365 Rev C: Nuclei Isolation for Single Cell Multiome ATAC + Gene Expression Sequencing including the DNase treatment step and using 0.8x lysis buffer strength. Nuclei were submitted to the UCSF Genomics CoLabs for library preparation and sequenced by the UCSF Institute for Human Genetics.

Multiome Data Analysis

For each sample, multiome sequencing data was aligned to the Human GRCh38 reference genome (10X Genomics) containing custom reference sequences for integrated transgenes using CellRanger ARC (v2.0.2). Background RNA transcripts were then removed using CellBender (v0.1) before creation of a dual RNA/ATAC object and data analysis using Seurat (v4.4.0) and (Signac v1.9.0). Cells were filtered to have between 500 and 10,000 detected genes, between 1,000 and 50,000 RNA UMI, TSS enrichment score greater than 1, a nucleosome signal less than 2, and at least 1000 ATAC UMI. DoubletFinder (v2.0.3) was implemented only on RNA data to detect and remove presumptive doublets. RNA assay data was log normalized and scaled, while ATAC assay data was processed by latent semantic indexing using the RunTFIDF() and RunSVD() functions. Both assays were incorporated for UMAP visualization using the FindMultimodalNeighbors() function, and clustering was performed on RNA data with FindClusters() using the Louvain algorithm with multilevel refinement (algorithm = 2) and a resolution of 0.8. Clusters were annotated as described in the text by examining relative expression levels of marker genes. To facilitate balanced analysis, samples from matched cell lines (i.e., WTC-NEP and WTC-NMP) were subset to approximately the same number of cells.

Subsetting included taking a random sample of a fixed number of cells as well as all cells in p2 and V2a clusters since they represented the major cell types of interest. Only after each sample was individually annotated and subset were samples merged using Harmony integration (theta = 1, sigma = 0.6). 12,020 cells were included in the subset and integrated object (NEP, NMP, and IND samples).

In the merged data, differentially expressed genes were identified using the FindMarkers() function using the Wilcoxon test (test.use = 'wilcox'). Differentially expressed genes were tested for enriched gene ontology terms using the enrichGO() function in the clusterProfiler (v4.4.4) package. Differentially accessible ATAC peaks were identified using FindMarkers() function (test.use = 'wilcox' and min.pct = 0.1). The genes near the differentially expressed peaks were tested for enriched gene ontology terms using the GREAT tool (http://great.stanford.edu/public/html/). Motifs were assigned to ATAC peaks with the AddMotifs() function and using the JASPAR2020 motif database. Motif enrichment in ATAC regions was run using the FindMotifs() function and compared to a set of 50,000 GC-content matched background peaks identified using MatchRegionStats(). For label transfer, human fetal samples were downloaded from GEO (GSE171890) with the provided cell annotations. Each sample was subset to ventral spinal cord cell types then integrated into a single object in Seurat. NEP and NMP *in vitro* datasets were mapped onto the *in vivo* data using FindTransferAnchors() and TransferData() functions.

Calcium Imaging

Freshly thawed d19 neurons were counted and replated at a density of 150,000 cells per well into geltrex coated 96-well plates in NIM supplemented with 100 nM retinoic acid, 10 ng/mL BDNF, 0.4 ug/mL ascorbic acid, 300 nM Purmorphamine, 1 uM DAPT, and 1x CET cocktail. After two days, an additional 1x volume supplemented BrainPhys media was added to each well. BrainPhys media (StemCell Technologies) was supplemented with 1:50 SM1 supplement, 1:100 CultureOne supplement, 1x PenStrep, 10 ng/mL BDNF, and 10 ng/mL GDNF. At indicated time points, media was fully removed and replaced with BrainPhys Imaging Optimized Medium with 1 ug/mL Fluo4-AM (Ion Biosciences) and 1:100 Pluronic F-127 (Ion Biosciences) and incubated for 1 hour. Media was then again completely replaced with warmed BrainPhys Imaging Optimized Medium alone and cells were imaged on an ImageXpress Confocal HT (Molecular Devices) equipped with stage heating and CO2 control (37°C, 5% CO2) at 10x magnification for 1 minute at a frame rate of 2 Hz. After calcium imaging, cells were fed with supplemented BrainPhys media and returned to the incubator for continued maturation.

Calcium imaging data was analyzed using custom written python code. Dense cultures and overlapping cells prevented easy masking on cell bodies for ROI, so a more agnostic approach was taken. All images in a single imaging session were collapsed into a maximum projection and then a global threshold was applied to create a mask of the recorded cell area. The cell mask was then divided into a 64x64 grid, with each square of the grid being treated as a single ROI (4,096 potential ROI). All pixels within the ROI which were included in the threshold mask were included in fluorescent intensity calculations. ROI with no pixels included in the threshold mask were not quantified.

Induced Line Creation

The NGN2:LHX3 induced cell line was produced by modifying an existing plasmid for induced motor neurons: PB-TO-hNIL was a gift from iPSC Neurodegenerative Disease Initiative (iNDI) & Michael Ward (Addgene plasmid # 172113). PB-TO-hNIL was amplified in a PCR reaction to remove the ISL1 coding sequence using the forward primer ATGGAAGCCAGAGGCGAAC and reverse primer AGGTCCAGGGTTCTCCTCCACGTCTC using KOD XtremeTM Hotstart Polymerase (Millipore) then digested with DpnI (NEB) and recircularized using a T4 ligase (NEB) blunt end ligation with PNK (NEB). The resulting plasmid was transformed into DH5ɑ competent E. coli (NEB) for colony selection and miniprep purification using a QIAprep Spin Miniprep Kit (QIAGEN). Deletion of ISL1 was confirmed by separate restriction digests with DraIII, SmaI, and BbsI. For transfection, WTC11 stem cells were passaged at a density of 25k cells/well into a 24-well plate. The following day, the cells were fed with fresh media for 1 hour prior to transfection using 250 ng each of the NGN2:LHX3 plasmid and pEIF1a::Transposase (gifted by Dr. M. Ward), and 1 uL of Lipofectamine Stem (Invitrogen) prepared according to manufacturer's instructions. The following day, the entire population of cells was passaged into T25 flasks and allowed to grow for another 24 hours prior to selection with 0.5 ug/mL puromycin. Purified cells were expanded and cryopreserved until future use.

Induced Neuron Differentiation

Induced neuron differentiation protocols were based on previously described protocols for NGN2 and NGN2:ISL1:LHX3 neurons (Fernandopulle et al., 2018). For induced neuron differentiation, stem cells were grown to near confluency on Geltrex coated plates before changing to induction media (NIM supplemented with 1 uM DAPT, 2 ug/mL doxycycline (dox), and listed concentrations of RA (most efficient for NGN2:LHX3 line is 1 uM RA). Cells were then fed every other day. On day 2, cells received NIM with 2 ug/mL dox, RA, and 10 ng/mL BDNF. From day 4 onward, the media formulation was the same as day 2, but without dox.

RNA Isolation and qPCR

RNA was isolated using the QIAGEN RNeasy Mini Plus Kit according to manufacturer’s instructions. Whenever possible, cells were lysed directly in the culture vessel. Note, for highly dense V2a differentiations from day 9-19, up to 1 mL of RLT with BME was used per well of a 24-well plate. Cell lysate was transferred to 1.5 mL tubes and directly placed in a -80°C freezer until RNA extraction. QIAShredder tubes were used to homogenize samples prior to gDNA clean-up and RNA isolation. RNA was eluted in 50 uL of nuclease-free water (Ambion) and quantified via nanodrop. If samples had insufficient concentration (<60 ng/uL) or salt contaminants (260/230 ratios < 1.5), they were further processed using the Zymo RNA Clean and Concentrator Kit. If not used immediately, RNA was stored at -80°C. RNA was converted to cDNA for qPCR using the qScript cDNA SuperMix (Quanta Bio) according to manufacturer’s instructions. qCPR reactions were set up in 10 uL volumes in 384-well plates using 20 ng of cDNA per reaction, 2X PowerUp SYBR Green Master Mix, and 200 nM of each primer. Custom primer sequences were ordered from IDT as single-stranded DNA oligonucleotides. qPCR reactions were run on a QuantStudio 6 Flex following the manufacturer recommended standard cycling conditions for the PowerUp SYBR Green Master Mix.

Cell Oracle

Cells were filtered to include only those with scATAC-seq peaks between 2,000 and 20,000. Cicero was used to extract cis-regulatory connections and identify co-accessible peaks (Pliner et al., 2018). We scanned these peaks for transcription factor motifs using the motif scan function from CellOracle (Kamimoto et al., 2023).

For the scRNA-seq data, we followed similar preprocessing steps to analyses from previous section, and then filtered down cells to p2 and V2a annotated cells. The remaining clusters were then integrated based on their NMP/NEP identity using the Combat function in Scanpy (Wolf et al., 2018). Genes were filtered to include the top 3,000 most variable genes. The base gene regulatory network (GRN) was generated through the CellOracle pipeline by combining ATAC-seq peaks with motif information, after which centrality scores for each node in the GRN were calculated. Pseudotime analysis was performed based on NEP and NMP lineages.

Desired perturbations were simulated using the generated GRNs and the CellOracle pipeline. Subsequently, the gradient of shifts and effects on developmental pseudotime were calculated. Pre- and post-perturbation gene expression matrices were exported, and gene set enrichment analysis was performed using the GSEApy package with the c2.cp.reactome category (database version 2023.2.Hs) from the Msigdb class (Fang et al., 2023). Enrichment was analyzed with the gp.gsea function, utilizing the signal-to-noise ratio metric for gene ranking and permutation testing on pre- and post-perturbation data.

Lentiviral shRNA production and knockdown

Cloning and lentivirus production followed recommended protocols by the Broad Institute Genetic Perturbation Platform (https://portals.broadinstitute.org/gpp/public/). Briefly, the pLKO.1 cloning vector (a gift from David Root; Addgene plasmid # 10878) was digested with AgeI and EcoRI and gel purified. Oligos containing shRNA sequences against target genes (see Supplemental Table 2; IDT) were annealed to form double stranded inserts and ligated into the pLKO.1 backbone. Two shRNA different sequences per target gene were made, for a total of 10 unique plasmids. Plasmid DNA was isolated using ZymoPURE Plasmid Miniprep Kit (Zymo) and confirmed using long-read whole plasmid sequencing (Plasmidsaurus).

For lentivirus production, pLKO.1-shRNA plasmid, pCMV-dR8.91, and pMD2.G (a gift from Didier Trono; Addgene plasmid # 12259) plasmids were combined in a 9:8:1 ratio and transfected into HEK293T cells using Nanofect Transfection reagent (ALSTEM) following the manufacturer's protocol. Media was changed the following day and collected at 48 and 72 hours post transfection. Viral supernatant was stored at -20°C until use. For WTC11 stem cell transduction, viral supernatant was added to stem cell media in a 1:20 ratio with 10 ug/mL polybrene (Millipore). After two days, stem cells were selected using 0.5 ug/mL puromycin for an additional two days before subsequent expansion. Upon differentiation to V2a neurons by NEP and NMP routes, cultures were additionally selected with puromycin between day 7 and 9 to ensure that the shRNA construct had not been silenced.

Bulk RNA Sequencing and Analysis

Bulk RNA sequencing libraries were produced using the Mercurious™ High sensitivity BRB-seq kit (Alithea Genomics). For the High sensitivity BRB-seq kit, purified RNA was first isolated using the RNeasy Mini Plus kit (QIAGEN). Libraries were sequenced on a NovaSeq X (Illumina) by the UCSF CAT Core. Code for sequence quality control, alignment, and generation of count matrices followed MercuriousTM High sensitivity BRB-seq kit recommendations and used fastQC (v0.11.5) and STAR (v2.7.11b) packages. Samples with greater than 2e6 total counts were kept for further analysis. Counts and metadata tables were combined into a single dataset using DESeq2 (v1.36.0). For all-sample comparison using PCA, VST-normalized counts were extracted and batch corrected using the limma (v3.54.2) removeBatchEffect() function. For heatmap plotting, the size-factor normalized counts were extracted and used. For differential expression testing, the counts matrices were subset to only include either NEP or NMP data before generating the DESeq object using a ' ~ batch + KD_Gene' design. The lists of differentially expressed genes were filtered to only include genes that crossed the significance threshold in 1 or 2 samples. For single sample GSEA scoring, raw counts matrices were TPM normalized prior to running removeBatchEffect(). This corrected TPM matrix was then ranked and analyzed using singscore (v1.19.1) with the differentially expressed genes between NEP and NMP V2a neurons from Multiome being used as input gene sets.

Acknowledgements

We would like to thank Kenneth Wu and Luke Judge for generating and sharing the XR1 cell line. We would like to thank Karissa Hansen for her expertise and assistance with bulk RNAseq analysis. We also thank following core facilities for their support and experimental advice: the UCSF Center for Advanced Technology (CAT) supported by UCSF PBBR, RRP IMIA, and NIH 1S10OD028511-01 grants, UCSF Laboratory for Cell Analysis, UCSF Center for Advanced Light Microscopy, UCSF Genomics CoLabs, UCSF Institute for Human Genetics, Gladstone Stem Cell Core, Gladstone Assay Development Core, and Gladstone Flow Core. We would like to thank the members of the Fattahi Lab for their thoughtful feedback. The work was generously supported by grants from the NIH Director's New Innovator Award (DP2NS116769) and the National Institute of Diabetes and Digestive and Kidney Diseases (R01DK121169) to F.F. N.H.E was supported by a fellowship from the ARCS Foundation. L.V.Z was supported by a grant from the California Institute for Regenerative Medicine (DISC2-14180).

CHAPTER 4

Strategies for improved engineering of *in vitro* neurological systems

Introduction

Proper function of the nervous system depends on precise orchestration of numerous neural and non-neural (glial, vascular, etc.) cell types to create complex networks. While there is some neuroplastic potential, damage to mature neural networks due to injury or disease is often irreversible. Neurons are especially susceptible to permanent loss of function when these networks are compromised in conditions ranging from acute traumatic injury to chronic neurodegeneration (Kwon et al., 2004; Ahuja et al., 2017). Abnormal development, loss of circuit relay, or selective degeneration of neurons can result in life-long and debilitating outcomes, with limited chance of neural regeneration or spontaneous replacement. This has led to a growing interest in the promise of cell-transplantation therapies for neural diseases, including in engineering relevant cell types *in vitro* to replace those lost in specific disease or injury settings (Assinck et al., 2017; Zholudeva and Lane, 2019; Fischer et al., 2020; Piao et al., 2021).

Here, we highlight the expanding toolbox of techniques used to derive neurons from pluripotent stem cells (PSCs), and describe their utility in research and preclinical settings for disease modeling and nervous system repair. We propose that combining aspects of directed and induced differentiations could improve cell type specificity, purity, scalability, and modularity in downstream applications. Specifically, we will discuss how different methods of morphogen and chemical stimulation, transcription factor overexpression, transcription factor cooperation, microRNA regulation, and fate “blocking” can be utilized to generate defined populations of neurons.

Directed versus induced differentiation

The generation of neurons from human PSCs *in vitro* largely centers around two approaches: directed differentiation and induced differentiation. Directed differentiation recapitulates the developmental progression from stem cells to neurons by employing exogenous factors, such as recombinant proteins or small molecules, to stimulate or antagonize signaling pathways known to be important during development of the cell types of interest (**Figure 4.1A**). For example, dual inhibition of BMP and TGFb signaling is necessary to specify the anterior neural plate during gastrulation (Camus et al., 2006; Smith et al., 2008; Muñoz-Sanjuán and Brivanlou, 2022). This can be recapitulated *in vitro* by the addition of recombinant proteins, such as Noggin, or more commonly by small molecule compounds which antagonize the intracellular relay of TGF and BMP signals (Smith et al., 2008; Chambers et al., 2009, 2012). The cells are sequentially transitioned through increasingly restricted progenitor populations to achieve target neural identity, and protocols utilizing this strategy have been described for numerous neural types (Wichterle et al., 2002; Li et al., 2005; Kriks et al., 2011; Shi et al., 2012; Fattahi et al., 2016; Butts et al., 2017). Because cells are transitioned via exogenous stimulation, directed differentiations rely on an intrinsic rate of developmental progression, can take weeks to months to produce post-mitotic target cell populations, and even longer for those cells to display appropriate physiological characteristics. These long differentiations also typically result in heterogeneous populations of neurons from target nervous system regions (Merkle et al., 2015; Butts et al., 2017; Sloan et al., 2018). This heterogeneity can be useful, for instance when studying developmental determinants which promote one neural fate over the other, especially when the decision points of such fate decisions are unknown (Hoang et al., 2018; Bhaduri et al., 2020). Further, when cultured in three-dimensional organoids, mixed populations of progenitors and neurons from directed differentiations can give rise to highly patterned tissues that closely resemble *in vivo* development, such as the layers of the cortex or the folding of the optic cup (Eiraku et al., 2011; Kadoshima et al., 2013; Lancaster et al., 2013), enabling investigation of complex aspects of nervous system development (Qian et al., 2016; Tang et al., 2016; Bershteyn et al., 2017; Pollen et al., 2019; Birey et al., 2022). However, the balance of specific neural populations can shift dramatically batch-to-batch within a single cell line and between cell lines, decreasing the translational potential of such strategies for targeted therapeutic applications (Volpato et al., 2018). This is not to say that it is impossible—indeed, PSC-derived dopaminergic neurons are currently entering clinical trials to treat Parkinson's disease (Doi et al., 2020; Schweitzer et al., 2020; Kim et al., 2021; Piao et al., 2021). Directed differentiation from stem cells to neurons using exogenous factors remains a standard approach across the field.

By contrast, direct induction uses genetic engineering techniques to "turn-on" expression of neurogenic factors to generate a post-mitotic neural fate directly from stem cells (**Figure 4.1B**). This process bypasses or drastically abbreviates developmental progression, and shortens the amount of time that it takes to generate neurons, with morphological changes occurring within 72 h in human cells and spontaneous electrical activity observable in as little as 4 weeks (Zhang et al., 2013; Busskamp et al., 2014; Wang et al., 2017). Not only is the speed of the induction beneficial, but induced neuron populations tend to be more homogenous than those produced by directed differentiation, both within and between batches (Zhang et al., 2013). By combining induced expression of pro-neural transcription factors, usually bHLH family proteins, with cell type-specific transcription factors, induced neurons can be further directed to adopt highly specific cell fates. Combinations of transcription factors (TFs) have been used to produce dopaminergic neurons, sensory neurons, motor neurons, and cortical GABAergic neurons, among others (Goto et al., 2017; Yang et al., 2017; Azimi et al., 2018; Nickolls et al., 2020). Such targeted strategies allow for screening of disease phenotypes (e.g., disease-in-a-dish), high-throughput drug screens, and could potentially serve as a cell source for cell replacement therapies (Wang et al., 2017; Feliciano et al., 2021). However, induced approaches exist for very few of the vast diversity of neuron types within the body.

Source of cells

The starting cellular material is an important consideration when producing neurons for disease modeling or potential therapeutic applications. This review is focused on stem cells as the starting source for both directed and induced differentiations to allow for comparison between these methods and to contrast with *in vivo* development. Early experiments used somatic cells, typically astrocytes or fibroblasts, as a starting point to screen for factors with direct reprogramming or transdifferentiation (i.e., across germ lineage) neurogenic potential, which were subsequently successfully applied to stem cells (Berninger et al., 2007; Vierbuchen et al., 2010; Bocchi et al., 2022). Furthermore, neurons induced directly from fibroblasts retain epigenetic markers of aging, and thus can be useful for screening age-related phenotypes that are difficult to recapitulate in stem cell-derived neurons (Mertens et al., 2015; Yang et al., 2015). Thus, fibroblasts and other somatic cell types, such as glia, are a useful cell source for screening and age-associated disease modeling.

Pluripotent stem cells, by contrast, can be more flexibly programmed or directed to desired cell types. The discovery of induced pluripotent stem cells (iPSCs) drastically improved stem-cell based disease models (Takahashi and Yamanaka, 2006; Takahashi et al., 2007; Yu et al., 2007). iPSC technology has allowed research to generate cell lines from individuals with clinically confirmed illness, and thus study disease phenotypes in the genetic contexts known to present disease phenotypes. iPSC lines from patients can also be matched with "unaffected" cell lines derived from siblings or parents. Alternatively, scientists can generate a defined mutation or set of mutations in a "wild-type" cell line. However, due a re-setting of the epigenetic clock during reprogramming, or soon after fertilization in the case of embryonic stem cells (ESCs), stem cells lack many markers of age, and thus make for imperfect models of age-related disease (Marion et al., 2009; Suhr et al., 2010; Kerepesi et al., 2021; Simpson et al., 2021).

Stem cell lines can also possess lineage biases, both between genetically unique donors and between uniquely isolated clones from the same donor, which can manifest as a "preference" to differentiate to certain germ lineages over others (Osafune et al., 2008; Boulting et al., 2011; Strano et al., 2020). While this poses less of a hurdle in induced differentiations, which employ strong over-expression of transcription factors, it can shift the outcome of directed differentiations. In addition to innate lineage bias, PSC lines can also exhibit differing sensitivities to morphogens. The most common example of this is sensitivity to WNT signaling. The concentration of CHIR99021, a GSK3 inhibitor and agonist of the WNT pathway frequently used in neural differentiations, has to be routinely titrated for each cell line to achieve similar results (Ashton et al., 2015; Strano et al., 2020; Libby et al., 2021).

Lastly, when considering the production of neurons for therapeutic applications, cell lines must be produced and maintained under current good manufacturing practices (cGMPs), including use of defined, xeno-free culture reagents, testing for viral or bacterial contaminants, and confirming normal karyotypes. Both ESC and iPSC lines have been produced under cGMP conditions and are commercially available. Although there are many considerations to working with stem cells, their ability to be differentiated through both directed and induced methods into neurons has made them an invaluable tool to study development and model disease, and has opened new avenues for personalized medicine and potential cell replacement therapies.

Regionalization – the foundation of cell identity

One of the earliest processes in post-gastrulation development is the axial rostro-caudal (head–to-tail) specification of the nervous system. In the gastrula, the anterior neural plate gives rise to the forebrain, while caudalizing signals originating from the node at the posterior of the embryo and, later, anterior somites are necessary to induce hindbrain identity, as well as to specify a pool of axial stem cells called neuromesodermal progenitors (NMPs) (Tzouanacou et al., 2009; Wymeersch et al., 2016; Metzis et al., 2018; Frank and Sela-Donenfeld, 2019). NMPs are maintained around the node-streak border during axial elongation, and proliferate to give rise to both spinal cord progenitors and presomitic mesoderm. The allocation of different progenitors to different regions of the rostrocaudal axis at such an early time in development underscores how critical this step is in preventing unwanted cell types from arising in the wrong location. Even a transcription factor as ubiquitous in the nervous system as SOX2 shows differential chromatin binding in the developing embryo depending on the region-specific cofactors available (Hagey et al., 2016). For these reasons, regionalizing steps are critically important in any differentiation protocol, as this process sets up the chromatin landscape upon which downstream, cell-type-specific TFs act, while also limiting the number of potential cell fates.

Throughout the nervous system, regional identity is underwritten and reinforced by the expression of TFs containing highly evolutionarily conserved homeobox domains. Homeobox gene families important for forebrain and midbrain development include LHX, OTX, SIX, and DLX (some of which are also used in induced differentiation strategies). However, among the most well-studied regionally specific homeobox proteins are the HOX and CDX gene families, which are expressed at hindbrain levels and below. Consisting of 39 genes across four unique clusters in mice and humans, HOX proteins demarcate functionally and anatomically distinct regions within the hindbrain and spinal cord (Dasen et al., 2005; Philippidou and Dasen, 2013; Deschamps and Duboule, 2017). HOX genes play a central role in hindbrain rhombomere formation, with deletion or misexpression of anterior HOX genes resulting in loss or expansion of unique rhombomere domains (Frank and Sela-Donenfeld, 2019; Parker and Krumlauf, 2020). In the spinal cord, HOX genes help direct motoneuron identity, with distinct motor pools and columns generated at limb and trunk-innervating levels (Dasen et al., 2005; Dasen and Jessell, 2009; Jung et al., 2014). Homeobox-containing genes are frequently some of the earliest genes whose expression is differentially segregated into different regions of the nervous system, and they act as downstream effectors of regionalization.

Fortunately, extensive study in embryology has uncovered the major signaling determinants of regionalization, allowing for these processes to be recapitulated *in vitro*. For example, removal of stem cell maintenance signals and/or dual inhibition of TGFb and BMP pathways (also known as dual SMAD inhibition) is sufficient to produce SOX2 + /PAX6 + forebrain neural stem cells from PSCs (Smith et al., 2008; Chambers et al., 2009, 2012; Lippmann et al., 2014). To obtain neurons of hindbrain or high spinal cord identity, treatment of stem cells with either retinoic acid or low levels of Wnt is sufficient to upregulate rostral HOX paralogs 1–6, usually in conjunction with or even after neural induction with dual SMAD inhibition (Butts et al., 2017; Valiulahi et al., 2021). However, protocols to generate cells representing the most caudal segments of the spinal cord, including lumbar and sacral regions expressing HOX paralogs 10–13, were lacking until researchers learned to transition stem cells through a NMP state capable of upregulating these genes (Lippmann et al., 2015; Kumamaru et al., 2018; Wind et al., 2021). While cooperative FGF and Wnt activity is necessary to induce cervical and thoracic HOX genes (HOX7-9), caudalization of the cellular identity toward the lumbar level requires further stimulation by GDF11 to express HOX 10 and beyond (Mazzoni et al., 2013b; Lippmann et al., 2015). To date, most protocols to generate neurons of spinal identity achieve only rostral HOX gene expression, encompassing only cervical regions of the spinal cord, which innervate the forelimbs. Apart from the central nervous system (CNS), neurons of the peripheral nervous system (PNS), including sensory and enteric neurons, transition through a neural crest lineage during development. Therefore, differentiation protocols for these populations incorporate a period of neural crest induction, requiring Wnt and BMP, in conjunction with dual SMAD inhibition for neural induction (Denham et al., 2015; Fattahi et al., 2016; Alshawaf et al., 2018).

Emerging evidence points to the action of HOX genes in regulating and maintaining post-mitotic and post-natal neural identity as well (Feng et al., 2021), demonstrating that HOX expression is not only necessary for developmental patterning, but also strongly influences circuit connectivity and mature neural function. Osseward et al. (2021) reported that a k-means clustering approach to divide lumbar neurons from newborn mice revealed that the first major division between neurons did not resolve into neurotransmitter identity, as expected, but instead divided sensory laminae I-III from HOXC10 expressing neurons in laminae IV-X involved in motor control and proprioception (Osseward et al., 2021). Though not a direct tie to neural function, this evidence points to HOX gene function throughout spinal motor networks, not just in motor neurons themselves, as has been well-described.

Notably, genetic signatures of regional identity can persist through ex vivo culture across many passages and even through direct reprogramming (Kelly et al., 2009). Regional signatures are also maintained in expanded pools of neural stem cells, and can either help to reinforce cell identity or prevent adoption of cell fates that are not matched to the region of the starting cellular material (Kumamaru et al., 2018). For example, neurons induced from cortical gray matter or spinal cord-derived astrocytes retained markers of regional identity, particularly in the HOX genes expressed, producing neurons with more spinal or more cortical-like identities, respectively (Kempf et al., 2021). Similarly, neural induction via NGN2 overexpression yielded a mixed population of cells with CNS and PNS characteristics that were resolved by short regional patterning steps prior to NGN2 induction (Chen et al., 2020; Lin et al., 2021). Dual SMAD inhibition was sufficient to specify cortical-like populations, whereas treatment with a TGFb inhibitor and Wnt agonist prior to induction specified hindbrain-like populations. Further, overexpression of specific HOX TFs in *in vitro* differentiated motor neurons shows that individual HOX genes can bind thousands of different regions, changing the chromatin landscape and the resulting motoneuron subtype under otherwise uniform induction conditions (Bulajić et al., 2020). It remains unknown, however, the extent to which expression of individual HOX genes can recapitulate the regulatory landscape that is produced by sequential activation of all of the HOX clusters simultaneously, as happens in development. Thus, regionalization steps are complementary to TF-driven neural induction, increasing the specificity of the resulting populations. Regionalization using readily available potent small molecule modulators or recombinant proteins can be a fast process during the relative timeline of neuron differentiation and maturation. It is also a critical step that informs all downstream processes of neuronal subtype specification.

Neural Induction

Following regionalization, which may require maintaining a multipotent progenitor pool such as neural crest cells or NMPs, cells must be further coaxed toward a neural lineage. During development, an ever-changing milieu of morphogenic gradients, metabolites, and extracellular environments direct transcriptional and epigenetic changes that influence downstream cell fate. In order to faithfully recapitulate this process *in vitro*, cells must be sequentially passed through distinct developmental states that require time to adapt and to further progress. Thus, directed differentiations tend to rely on prior *in vivo* studies that have determined the major underlying signaling cues and developmental processes that give rise to target populations (Sagner and Briscoe, 2019). In induced differentiations, many of these developmental steps are skipped over by the expression of one or more factors that can efficiently direct cell fate in the absence of otherwise necessary extrinsic cues.

Some of the most commonly utilized induction systems, and indeed the simplest, rely on over-expression of single proneural TFs. These TFs, often members of the bHLH family (including ASCL1, NGN2, NGN1, NEUROD1) are sufficient to induce a neural fate on their own (Flitsch et al., 2020; Bocchi et al., 2022; Hulme et al., 2022). They can act as pioneer factors, binding to and opening regions of chromatin that are normally silent in the base state, and their potency is perhaps amplified by the fact that they can upregulate the endogenous expression of other proneural TFs (Busskamp et al., 2014). Within a short timeframe, neurogenic TFs upregulate a pan-neural transcriptional program, which includes genes for axon and dendrite morphogenesis and synaptic transmission. For example, while initially activating different networks, independent induction of either ASCL1 or NGN2 produce largely similar populations of neurons from spinal cord glia, though ASCL1 has also demonstrated an increased ability to activate inhibitory identity in other models (Yang et al., 2017; Kempf et al., 2021). NGN2 has proven to be especially potent in producing induced neurons, leading to the creation of a human stem cell line harboring a dox-inducible NGN2 cassette that can readily be used to generate large numbers of neurons for screening purposes (Zhang et al., 2013; Wang et al., 2017; Fernandopulle et al., 2018; Tian et al., 2019). While these screens are highly informative, they may miss cell-type specific differences, such as those that make motor neurons or dopaminergic neurons susceptible in ALS and Parkinson's disease contexts, respectively. In order to study cell type-specific effects, one must either (1) isolate primary cells, (2) follow or develop directed differentiation protocols, or (3) engineer mechanisms to direct the identity of the resulting neural populations.

Introducing specificity through transcription factor interactions

Because directed differentiations closely recapitulate developmental processes and morphogenic cues, the resulting neural progenitors simultaneously express many TFs necessary for neuron fate specification. By contrast, single-factor induced neurons appear to adopt an excitatory glutamatergic identity most similar in expression pattern to cortical neurons (Zhang et al., 2013; Busskamp et al., 2014). In order to use an induced approach to generate specific neuron sub-types for disease modeling or pre-clinical study, cell type-specific TFs with a known role in the desired cell fate are frequently expressed alongside neurogenic TFs. The number of co-expressed proteins can range from one additional TF to several, depending on the desired cell type. If well-established unique markers exist for a population of interest, screens can be employed to agnostically determine the best combination of TFs to induce. Screens can range in complexity, from screens containing all annotated TFs, to targeted screens of a short-list of likely candidates (Teratani-Ota et al., 2016; Guo and Morris, 2017; Yang et al., 2017; Ng et al., 2021).

However, the co-expression of several TFs should come with considerations of their cooperation, potential cross-repression, timing of expression during development, and duration of induction (Bocchi et al., 2022; Hulme et al., 2022). In tissues with highly conserved and well-described genetics, such as the spinal cord, *in vivo* studies have identified factors that are both necessary and sufficient to induce specific cell fates when ectopically over-expressed. For example, spinal motor neurons (MNs) specifically degenerate in ALS, and homogenous populations of MNs are desired for *in vitro* studies. Developmental studies in chick and mice identified LHX3 as an overlapping marking of the adjacent progenitor domains of spinal V2a interneurons and MNs, while ISL1 was necessary for MN development and expressed solely in the MN domain. Subsequent research found that LHX3, ISL1 and third protein, NLI, form a hexameric complex in a 2:2:2 ratio that potently activates a MN transcriptional program (Tanabe et al., 1998; Thaler et al., 2002; Song et al., 2009; Lee et al., 2012; Erb et al., 2017). By contrast, LHX3 and NLI, in the absence of ISL1, form a tetrameric complex, again in equimolar ratios, that promotes adoption of the V2a fate. Ectopic expression in the dorsal spinal cord of LHX3 alone produces CHX10 + V2a neurons, while co-expression of LHX3 and ISL1 produces HB9+ MNs (Thaler et al., 2002; Song et al., 2009). Knowledge of the specific TF complexes that are sufficient to induce these fates led to the development of mouse and human cell lines that utilize doxycycline-induced expression of LHX3 and ISL1 in equimolar ratios alongside the neurogenic TF NGN2, and which rapidly and homogenously produce MNs in a short time frame (Mazzoni et al., 2013a; Fernandopulle et al., 2018).

Other cooperative systems are known to drive specific spinal cord neuron populations, but have not yet been engineered into induced differentiation systems. For instance, V2a neurons, which have a role in the spinal motor circuitry and central pattern generator (CPG) networks, and degenerate alongside the MN population in ALS (Crone et al., 2012; Azim et al., 2014; Bubnys et al., 2019; Salamatina et al., 2020), could potentially be generated by induced expression of NGN2 and LHX3 in the absence of ISL1 (**Figure 4.2B**). Since NLI is abundantly expressed in the developing nervous system, the LHX3:NLI tetrameric complex could be readily assembled. Inhibitory V2b neurons share a common progenitor with V2a neurons, but differentiate toward a GATA2/3 + GABAergic fate due to activated Notch signaling, while V2a neurons require Notch inhibition (Peng et al., 2007). A direct target of Notch activation is the factor SCL, which forms a complex with the LIM competitor LMO4 and NLI (Peng et al., 2007; Joshi et al., 2009). This V2b complex activates and incorporates GATA2, as well as activating GATA3 and GABAergic genes. One could then hypothesize that an inducible cell line containing a proneural factor, such as NGN2 or ASCL1, co-expressed with SCL and LMO4, would produce V2b spinal inhibitory interneurons, though this has yet to be demonstrated. Undoubtedly, many other cooperative TF complexes could be reconstituted in induced systems to promote specific cell fates.

microRNA-mediated repression as a means to increase cell-type specificity

Another method to direct neural development and fate is through the use of micro-RNA (miRNA). Consisting of approximately 22 nucleotides, miRNAs are highly conserved and abundant in the human genome. Processed from double stranded RNA by Dicer and later bound by the RISC complex, miRNAs bind mRNAs and repress their translation (Bartel, 2004). Similar to how single TFs can activate or repress genes throughout the genome, miRNAs are capable of regulating hundreds of genes simultaneously, biasing cells between states (progenitor to postmitotic neuron) or fates. For example, neuron-specific miR-9/9* functions to balance the neural progenitor and terminal differentiation states by inhibiting Notch activity (Roese-Koerner et al., 2016). Interestingly, miR-9/9* is also a target of Notch, creating a regulatory loop wherein Notch slowly activates its own inhibitor to ensure eventual cell cycle exit and terminal differentiation. MiR-9/9* and miR-124, another neuron specific miRNA, have been used in studies to induce neural fates and facilitate neural maturation (Yoo et al., 2011).

Other miRNAs help to refine cell fate by facilitating boundary formation during development. For example, in the absence of Dicer, Olig2, a TF that helps specify MNs, is expressed more broadly than expected in the developing embryo (Chen et al., 2011). Further work identified miR-17-3p as a miRNA that was upregulated by IRX3, a reciprocal inhibitor of OLIG2 during spinal cord development, and that miR-17-3p targeted the 3'UTR of OLIG2 to spatially restrict its expression. Interestingly, the miRNA cluster that contains miR-17-3p, miR-17~92, was found to govern postmitotic survival of limb-innervating MNs via PTEN regulation (Tung et al., 2015). miRNAs can also regulate boundary formation and positional identity by acting on HOX genes. For example, boundary formation between Hoxa5 and Hoxc8 in the brachial spinal cord was found to rely on miR-27 (Li et al., 2017), while other miRNAs embedded within the HOX clusters themselves contribute to the posterior dominance of HOX genes (Mansfield and McGlinn, 2012). In all, these studies show that miRNA possesses strong regulatory activity *in vivo*, and can have an outsized influence on neuron maturity, fate, and positional identity.

Many methods to derive specific populations of neurons focus on positive enforcement of the desired fate, either through morphogen stimulation or expression of specific transcription factors. However, blocking undesired phenotypes could serve as an alternative route to increase specificity. Short-hairpin RNAs (shRNAs) are processed by the same endogenous machinery as miRNAs, resulting in repression of target transcripts. In both induced and directed systems, shRNAs against specific TFs or miRNAs could serve to canalize identity by blocking alternative routes at the same time as cells receive signals to promote the identity of interest. Indeed, in many cell lineages, loss of key genes that specify one cell fate can lead to the transformation to another (Arlotta and Hobert, 2015).

Caveats of induced systems

To this point, we have considered what to induce, but attention should also be paid to intracellular stresses associated with induction and the method used to express genes of interest. Ectopic overexpression of potent neurogenic genes, such as NGN2, induces a myriad of changes in a short time-span, including transcriptional, epigenetic, morphogenic, and metabolic changes as cells take a fast-track route to a neural identity (Gascón et al., 2016; Ordreau et al., 2021; Russo et al., 2021). While being able to perform neural induction without different media supplementation is a gold standard approach for proving the neurogenic potency of a system, it doesn't account for changing nutrient requirements as cells adopt a neuronal fate. Further, the duration of induction is important. A one-day pulse of doxycycline in induced sensory neurons can produce a phenotypically and functionally different population than a 14-day pulse of doxycycline (Nickolls et al., 2020). Though the exact reason why prolonged induction produced different cell fates is unknown, induction duration remains a crucial part of protocol optimization.

Maturation and neural activity

Aside from morphology, one of the most common benchmarks for neural maturity is the ability to form functional synapses and display electrophysiological activity. While patch clamp electrophysiology remains a gold standard approach, microelectrode arrays (MEAs) are becoming an increasingly commonly used tool for measuring neural activity from hundreds or thousands of cells simultaneously (Novellino et al., 2011; Odawara et al., 2014; Mossink et al., 2021). Consisting of a grid of electrodes embedded in a cell culture surface, MEAs allow for a single plated population of neurons to be monitored over hours, days, or weeks without disturbance (Nehme et al., 2021). Temporal changes observed in neuronal firing and network formation, as measured on an MEA (e.g., network bursts, network synchrony, etc.), may also reflect neuronal maturation. Multi-well MEA formats even allow for scaled screening approaches with neural activity as a readout, to assess how experimental conditions (e.g., application of drugs/neurotransmitters, change in oxygen or carbon dioxide concentration, disease state, stimulation, etc.) within the MEA alter these characteristics of neuronal maturation.

While monitoring electrophysiological activity can give an assessment of maturity as neurons are kept in culture for increasing amounts of time, it does nothing to speed the maturation process. However, due to age being such a strong risk factor for many neurodegenerative diseases, there is an experimental need to obtain fully mature or even aged neuronal phenotypes for therapeutic screening. Many techniques exist to try to advance neural maturation for both directed and induced populations. One of the most common methods is to co-culture neurons with glia [e.g., primarily astrocytes (Tang et al., 2013; Odawara et al., 2014; Nehme et al., 2021)]. Other groups have transitioned neurons into media more permissible to synaptic activity (Satir et al., 2020), altered the extracellular matrix (Hyysalo et al., 2017), or cultured neurons with their target populations (Bubnys et al., 2019; Vila et al., 2021). Directly inducing activity in neurons, either through optogenetics or electrical stimulation, has also been shown to improve morphological and electrophysiological properties (Park et al., 2015; Latchoumane et al., 2018; Giraldo et al., 2020; Pagan-Diaz et al., 2020). Some compounds, such as the Notch inhibitor DAPT, have been shown to speed the rate of differentiation in neurons and shorten the timeline to synaptic activity, and ongoing studies are searching for other compounds to further reduce barriers to maturation (Borghese et al., 2010). Lastly, expression of progerin, a protein associated with premature aging in Hutchinson-Gilford progeria syndrome, induces many phenotypes of aging in both stem cells and neurons (Miller et al., 2013). No single maturation method will work for every experiment, and as with differentiation methods, a combinatorial approach may produce the most robust results.

Delivery of inducible genetic elements

Various methods can be used to express induced elements, including viral integration, targeted safe-harbor integration, transposon integration, and even episomal expression. For purely research purposes, the method used to introduce an inducible cassette can be left up to researcher preference and familiarity. However, the safety and likelihood of integration of the delivery system is especially important if an engineered genetic system may move toward clinical trials. Retroviral and lentiviral transfections are highly efficient means of integrating genetic cassettes (Ma et al., 2003; Cao et al., 2010). Similarly, transposon-based piggybac systems can yield efficient integrations and stable expression, but with the additional benefit of transgene excision upon re-expression of the transposon (De Santis et al., 2018). Further, both transposon and donor DNA vectors can be introduced with simple electroporation, nucleofection, or lipofection, making them safer to work with than viruses.

Safe harbor loci, such as AASV1 or CLYBL, can be targeted using specific TALENs or CRISPR/Cas machinery. Functionally similar to the ROSA26 locus in mice, these regions allow for a site-specific integration without disrupting necessary genes, and have proven to be useful sites in which to integrate and standardize inducible gene systems since each clonal cell line will have a relatively uniform expression level, with one or two copies available.

One can express a genetic cassette from an episomal vector. Episomal vectors do not integrate into the genome and can maintain stable expression for extended periods of time. RNA-based Sendai viruses are commonly used to over-express Yamanaka reprogramming factors for iPSC production, but have also been used to express transcription factors to induce neurons (Goto et al., 2017). Plasmids containing the Epstein-Barr virus OriP/EBN1A features replicate within cells and are segregated with chromosomes during cell division, allowing long-term expansion of cell lines (Yates et al., 1985; Conese et al., 2004). Miniplasmids, lacking any bacterial sequences, are less likely to be silenced, but also lack replication competence and are diluted out in actively dividing cell populations. This limitation has been overcome by the production of pSMAR vectors, which contain scaffold/matrix attachment regions (SMARs) that allow them to be replicated and maintained throughout many mitotic cell divisions in both mouse and human stem cells and throughout differentiations (Mulia et al., 2021; Roig-Merino et al., 2022). Interestingly, while stable during mitotic division, pSMAR vectors are lost upon meiotic divisions and cannot be propagated through the germ line. Synthetic mRNA molecules can also be readily delivered into cells and maintain expression of transgenes long enough to induce cell fates from stem cells, but may require re-transfection for sustained expression (Warren et al., 2010; Goparaju et al., 2017; Azimi et al., 2018).

Expanding the system and building in complexity

As outlined above, deep understanding of the *in vivo* development of a neuron population of interest can allow for genetic engineering techniques to be leveraged to efficiently generate large numbers of pure neurons for study, as has been shown with the induced MN system. However, the resulting control over cell identity also allows for heterogenous systems, such as those produced during directed differentiations and which better recapitulate the *in vivo* environment of the neuron, to be "built" with reliable and reproducible complexity. For instance, by combining two or more induced cell lines together in defined proportions, one could pre-determine the relative ratio of each cell type in the resulting neuronal culture. This would reduce the need for cell selection or dissociation and sorting, while maintaining long-term developmental contacts. Possessing control over cell proportions would allow researchers to ask targeted questions about how subtle shifts in the balance of excitatory and inhibitory populations influence circuit activity or disease phenotypes in ways that are difficult to achieve using purely directed differentiations.

Another potential application of engineered cells is to understand the progression and spread of disease. For instance, in ALS, MNs are known to specifically degenerate, though it remains undetermined whether the disease begins at the neuromuscular junction (NMJ) or in the motor regions of the cortex, termed the bottom-up and top-down models, respectively. Recent evidence also points to spinal interneurons being lost around the same time as MNs (Salamatina et al., 2020). Using innovative co-culture systems and induced cells that produce muscle, MNs, and spinal INs, one could mix not only the cell types, but also cell lines with disease associated genetic mutations (Andersen et al., 2020; Vila et al., 2021). Such a system could help elucidate which aspects of ALS disease progression are cell autonomous, and which result from compounded susceptibility throughout the circuit.

Induced cell identities can also add an orthogonal approach to a directed differentiation in order to obtain a fractional population of cells from a different CNS region or a difficult-to-generate cell type. For example, induced overexpression of SOX9 was shown to produce oligodendrocyte precursor cells (OPCs) from stem cells (Ng et al., 2021). By mixing SOX9-expressing cells with wild-type cells in a cortical organoid differentiation, organoids developed myelinating cells by day 30 instead of the 100 + days observed in wild-type only organoids. Thus, induced cell lines can help improve directed differentiation models by adding to the cellular complexity, not just simplifying it.

Of course, identity is not the only feature that can be engineered into cells. We now possess a wide array of genetically encoded tools to augment cell function, such as the channelrhodopsins, halorhodopsins, and designer receptors exclusively activated by designer drugs (DREADDs). These tools allow for modulation of neural activity in real time upon application of an exogenous stimulant in the form of light or specific ligands. By incorporating these tools into the systems outlined above to generate specific types of neurons, one can closely examine the contribution of these cell types to circuit activity or function. Modified neural activity can also be used to enhance integration or reintegration into functional circuits. For instance, increased neural activity has been reported to improve functional recovery in spinal dorsal roots, retina, motor cortex, and sciatic nerve, and the spinal cord itself (Carmel and Martin, 2014; Lim et al., 2016; Ward et al., 2016; Wu et al., 2020; English et al., 2021; Petersen et al., 2021). Incorporation of similar opto-or chemogenetic modulators into transplanted cells for therapies could be another way to promote cell survival, integration and plasticity, such as in phrenic and autonomic circuits after spinal cord injury (Zholudeva et al., 2018; Squair et al., 2021). Recently developed synthetic biology systems and modulations of cellular adhesion molecules have also been demonstrated to be able to control cell fate and spatial patterns (Libby et al., 2018, 2019; Toda et al., 2018, 2020). Further development of these systems and incorporation into specific neuron populations produced *in vitro* could allow researchers to control boundary formation between two populations of neurons or even direct their synaptic connections to create neuro-chip circuits.

Concluding remarks

As highlighted in this review, advances in cellular engineering techniques have paved a new era of disease modeling, therapeutic development and a giant leap toward personalized medicine. Indeed, several new clinical trials are already underway to bring stem-cell derived neurons to patients. The development of specific neural cell types, co-cultures, and organoids will continue to greatly improve our understanding of neural development, network formation, and the processes that lead to change in neural injury and disease. Production of highly pure, relevant cell types at scale will be necessary to model circuits, use in high-throughput screens, and translate cell-replacement therapies to preclinical and clinical settings. Therefore, we posit that "hybrid approaches" that combine aspects of both directed and induced differentiation strategies will allow for the reproducible and flexible generation of desired cell types (**Figure 4.2A**). As discussed above, early regionalization steps are critical or refining the cell types produced by both directed and induced differentiation strategies and can be achieved by manipulating a limited number of developmental pathways. Subsequent induction of neurogenic or cell-type specific transcription factors, miRNA, or shRNA, along with exogenous small molecule supplementation will serve to further restrict cell fate to desired cell-types. Hybrid differentiation protocols will inevitably enhance our ability to create more specific neural components that can be used to develop treatments for neural injury and disease.

Figures

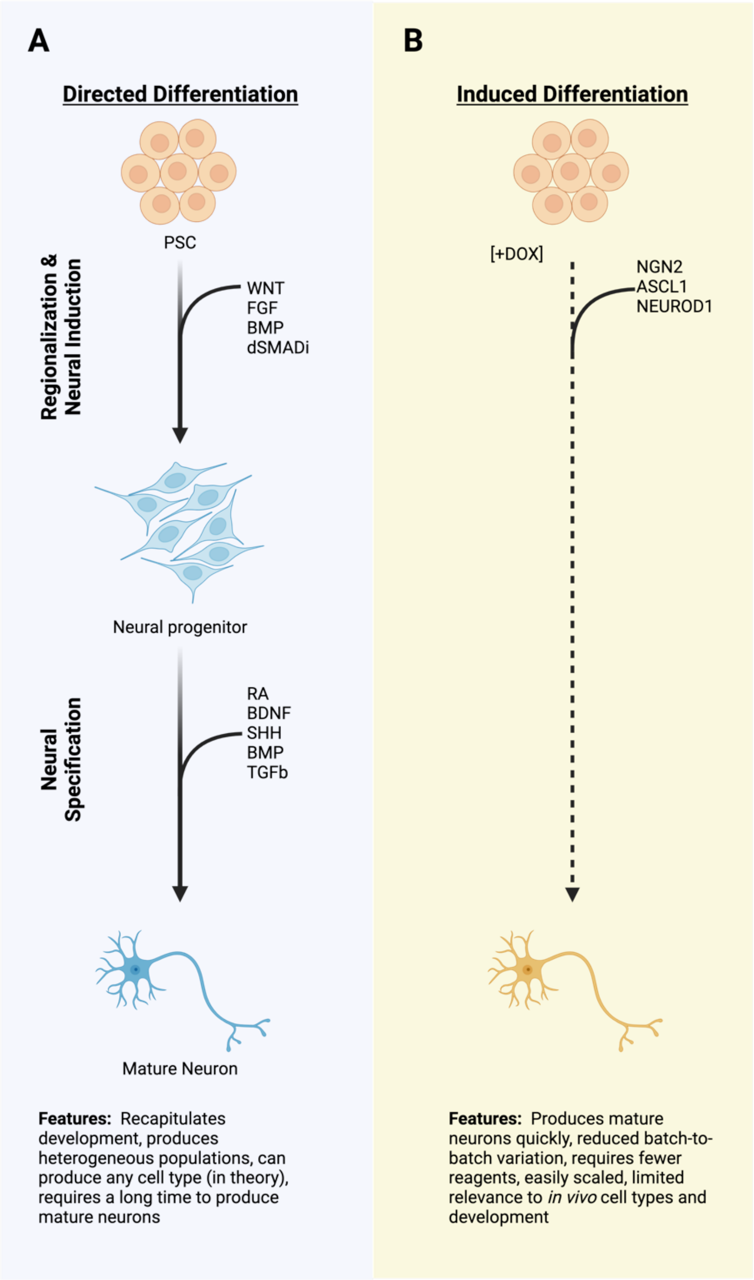

Figure 4.1. A schematic diagram of two strategies for differentiating pluripotent stem cells (PSCs) to neurons.
(A) Directed differentiation employing exogenous manipulation of common signaling pathways to produce neural progenitors and neurons. (B) Induced differentiation from PSCs using overexpression of proneural transcription factors which quickly produce a neuronal molecular fate. Dashed lines represent rapid processes due to induced TF expression as compared to the directed differentiation, which typically take a longer time. PSCs, pluripotent stem cells; TFs, transcription factors.

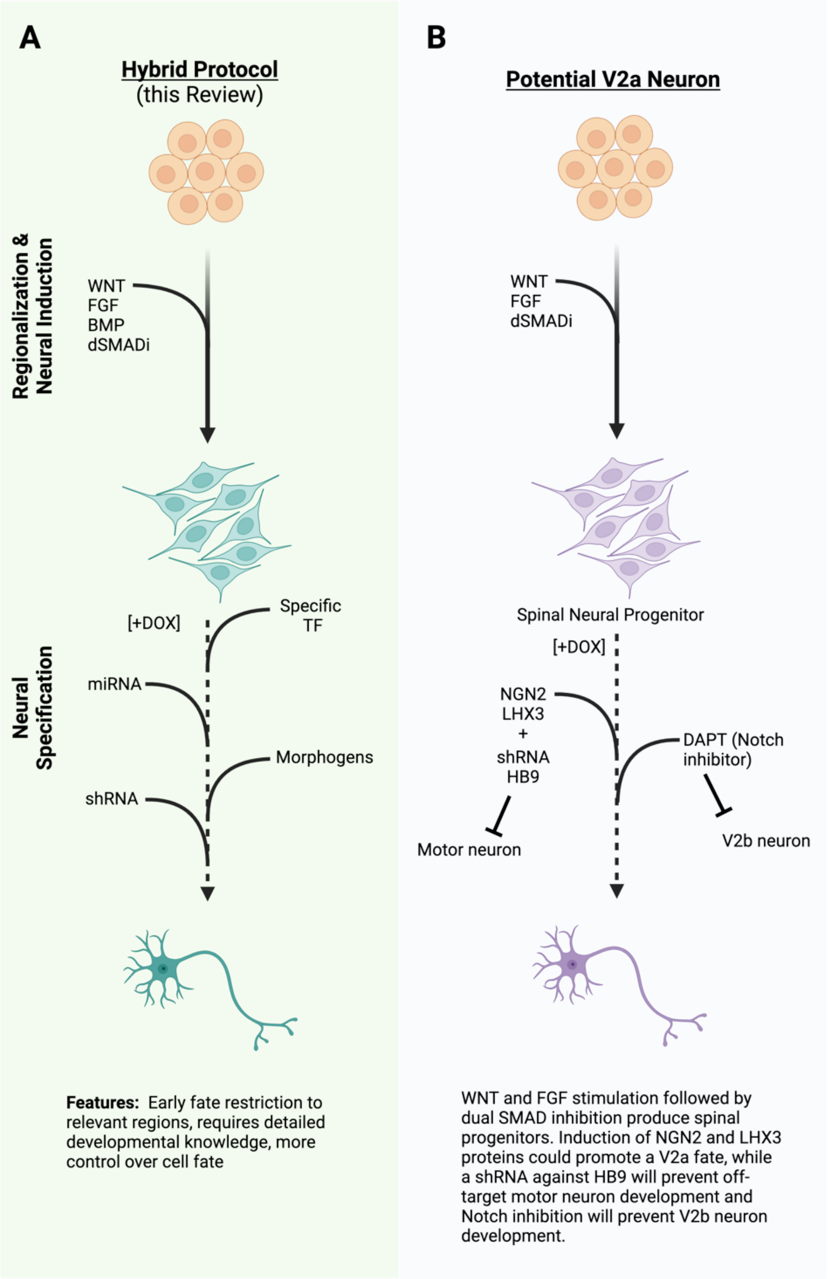

Figure 4.2. Diagrams detailing how multiple strategies can be combined to induce differentiation of specific, desired neural populations.

(A) A diagram of a hybrid differentiation paradigm employing the same regionalizing steps as directed differentiation while inducing specific transcription factors (TFs), miRNA, or shRNA to quickly induce or refine cell type during neural specification. (B) An example of a potential way to generate V2a neurons using the hybrid approach in 4.2A. TFs, transcription factors; miRNA, micro ribonucleic acid; shRNA, short hairpin ribonucleic acid; DOX, doxycycline; dSMADi, dual SMAD inhibition.

CHAPTER 5

Future Directions

Controlling populations in elongating organoids

The work presented in Chapter 2 stemmed from completely unexpected results of mine during a rotation project. Jessica Butts, who first published the human V2a protocol, had already worked on producing organoids using a modification of her protocol where she treated stem cells with CHIR for 48 hours prior to forming organoids of 10,000 cells and proceeding with differentiation (unpublished work). These organoids stayed spherical. My rotation project was meant to study whether making the organoids of different sizes altered the proportion of neural cell types. However, when I dropped the aggregates down to 3,000 cells total, I saw the first instance of the elongation phenotype. This observation proved to be reproducible and kicked off the entire elongating organoid project. After realizing that the period of CHIR treatment in stem cell media produced conditions amenable to NMP formation, we started staining organoids for TBXT. Since the organoids were started from dissociated populations of cells, the TBXT population was initially intermixed. However, both organoid sections and light sheet imaging showed that the TBXT positive cells 'sorted' themselves into islands or single poles prior to elongation (**Fig 2.7Aii**).

This observation opens several intriguing questions that I believe still remain unanswered, though I have not been following the gastruloid field very closely over the last few years. First, we never established the minimum number or percentage of NMPs necessary to generate elongation. This would be a relatively straightforward question to answer with AggreWell organoid formation where known proportions of NMPs and unpatterned cells could be mixed. I presume that this sorting happens due to different expression of surface cadherins and a level of EMT that may occur in the NMPs, but this process could also be investigated. Second, after formation of an NMP pole, do the NMPs act like an organizer, capable of recruiting and inducing surrounding cells into morphogenesis, or are they behaving separately of the rest of the aggregate? One way to potentially answer this would be to use a labeled population of NMPs (GFP expression, for example). If non-labeled cells become TBXT+ and/or are recruited into the elongating epithelium, then that would support some organizing activity and morphogen or contact-dependent signaling. In this case, does the opposite, non-elongating pole organize or secrete molecules to restrict the NMP activity, or does it remain 'neutral'? Spatial transcriptomics or delicate microdissection of organoids could be used to answer this.

So far, I have been focusing on the NMPs and a neural-biased organoid like the one we published. It's possible, however, that they could promote elongation, or recruit into the elongation, cells of other germ layers. How would early primitive streak like cells, mesoderm, endoderm, or dissociated EB cells behave in this context? The NMPs can produce mesoderm, but that seems to be a minority in our media conditions, and endoderm was never observed, constrasting with somewhat minimally patterned gastruloids. Using predifferentiated cells and mixing populations in fixed proportions, perhaps a slightly more engineered version of gastruloids could produce more reliable phenotypes and organization.

In our hands, it was difficult to maintain the organoids post-elongation for long periods of time, with the 'tail' becoming more compact or dying off or collapsing. These organoids were maintained on orbital shakers, adding a large degree of movement and shear to their environment. Transition to a stationary low-adherent culture condition could improve their long-term maintenance. Regardless, I believe that some of the greatest utility of the system lies in its use to study early patterning, cell sorting, and change in gross morphology, which all happen within a 10-day time period.

More questions asked than answered on V2a neurons

In Chapter 3, I present work investigating the impact of early progenitor lineage on V2a populations. One of the first observations that I made using the Multiome data was that the proportions of different cell populations are different between the two populations. Despite identical treatment with the relevant patterning molecules (retinoic acid and SHH via purmorphamine), the hindbrain-like NEP population was more ventrally shifted, with a large proportion of PHOX2B+ motor neurons and even floor plate cells. The spinal-like NMP population had no floor plate cells, fewer motor neurons, more V2a neurons, and more 'interneurons' which was my catch-all term for potential V3, V1 and V0 neurons. As reviewed in Chapter 1, the major signaling molecule specifying these ventral populations is SHH. The NEP population seems to be more sensitive to the same concentration of SHH signaling via purmophamine than the NMP population, even to such a degree that no floor plate cells were present in the later population, not just fewer. It is important to keep in mind that floor plate cells themselves also express and secrete SHH, perhaps exacerbating the ventral bias observed in the NEP populations. But the requirement of SHH to specify floor plate in the first place means that this is likely a confounding factor but not the primary driver. More research is required to study why this occurs and whether, as I hypothesize, this is due to an altering by Wnt of SHH sensitivity.

Another interesting finding that will require follow-up studies is that knockdown of CREB5 or TCF7L2 in the NMP differentiation significantly change gene expression in overlapping gene sets and specifically reduce the expression of the set of specific genes upregulated in NMP-derived V2a. The major caveat of this finding is that these results were obtained from bulk RNA seq data, and the effects may be due to larger differences in non-V2a populations than the V2a neurons themselves. I believe that some immunostaining or flow cytometry experiments to stain for both VSX2 and the differentially expressed genes could go a long way to answering this question. Another obvious start point is to perform a time-series qPCR experiment to look at expression levels of CREB5 and TCF7L2 which would give us insight into which period of differentiation they are most expressed during and in which they may display the most activity. TCF7L2 is known Wnt signaling effector protein, so it likely acts during the NMP phase of differentiation.

Some of the results from the CREB5 knockdown, however, provide the most exciting avenues for follow-up, at least in my opinion. We see that CREB5 KD reduces PBX3 expression and that there is an NMP-condition specific ATAC peak in the PBX3 locus. PBX3 belongs to the TALE family of transcription factors which are known to interact with HOX genes. Perhaps downregulation of PBX3 is the driver of many of the changes observed with CREB5 knockdown. This is supported by CellOracle, with PBX3 having some of the highest centrality scores in the predicted GRN. Investigation of the PBX3 NMP-enriched region on the UCSC genome browser shows that it is poorly conserved evolutionarily. Other nearby ATAC peaks which were strongly accessibly in both conditions are annotated as potential enhancers, but not this specific peak. Using this region and others, it would be interesting to perform enhancer reporter experiments in model organisms to see if they exhibit activity specific to the posterior embryo or control PBX3 expression levels.

Another intriguing line of research is how the NMP-derived lineage is propagated from the NMP state through to the post-mitotic neuron. We know that many transcriptional changes occur over this developmental period, and even comparing the p2 and V2a ATAC peaks via Pearson correlation shows that NEP- and NMP-derived p2 populations are far more similar to each other than they are to either V2a and *vice versa*. If you compare the NMP enriched peaks in p2 and V2a populations, you find that there is limited overlap there as well. This suggests that there is some degree of epigenetic imprinting, but that there are also many new peaks opening and closing at successive stages of differentiation. This could be mediated by the successive action of transcription factors or transcription factor complexes whose activity are modulated by lineage-specific genes, like HOX genes. The easy ability to sort an enriched V2a population from the FOXN4:Cre stem cell line means that a time course of ATAC or ChIPseq experiments could be used to answer these questions, especially with protocols requiring limited cell input such as CUT&RUN or CUT&TAG.

Perhaps the finding from Chapter 3 that will most intrigue the field is the observation of spontaneous synchronous activity being enriched in the NMP-derived V2a populations. While I have performed preliminary experiments to suggest that this activity is not exclusively mediated by gap junctions and can be reduced or blocked by the AMAPR inhibitor CNQX, it does not give a full picture into why this occurs. In a study that used labeled and sorted populations of mouse-derived spinal neurons, they showed that purified populations of excitatory V3 interneurons also produced reliable patterns of pulsing activity and that the speed of this could be controlled by adding defined proportions of inhibitory V1 interneurons (Sternfeld et al., 2017). The obvious next step to study the V2a population is the sort purified populations and observe their activity and see whether the synchronous bursts remain specific to the NMP-derived condition or if the presence of other neuron populations drastically changes the activity of mixed cultures. Another way to get a more granular view of the electrophysiological properties of the V2a neurons is to perform single cell patch clamp studies. This would allow comparison of resting membrane potential, burst rate, response to neuromodulatory drugs, and so on. Some of the most highly differentially expressed genes between the NEP and NMP conditions in the V2a populations were voltage gated ion channels, specifically CACNA2D3, CACNA2D1, and KCND2. The effects of these ion channels on synaptic transmission would be best described using patch clamp and treatment with channel-specific drugs such as gabapentin (a CACNA2D1 inhibitor).

The most difficult series of follow-up experiments would be to actually perform transplantation studies of each of the V2a populations see whether one of them displays better survival, integration, or recovery. The efficacy of the transplant may also be related to the transplant location, with the NEP population perhaps being more relevant in high cervical injuries and the NMP populations relating to low cervical or thoracic injuries. The work by Gregoire Courtine's group showing V2a-mediated recovery with epidural electrical stimulation is especially fascinating (Kathe et al., 2022; Matson et al., 2022; Squair et al., 2023). Are the V2a cells a convenient location to form new connections because of their preexisting connectivity, or are they specifically able to recruit new inputs? In a therapeutic context, is stimulated activity sufficient to drive this remodeling? Maybe combining a V2a cell replacement therapy with different stimulation paradigms, via electricity or through DREADDs, will improve overall functional recovery. *In vitro* populations of V2a neurons could potentially be used to study some of these fundamental processes, pairing stimulation with readouts for axon growth, for example.

Engineering V2a and V2b neurons. And astrocytes.

Chapter 3 also discusses induced neurons and my attempt to create inducible V2a neurons. I would like to stress that my primary research goal was to answer a more fundamental biological question and a minimal amount of work went into optimizing the induced system. However, Chapter 4 explores several ways that I could have tried to optimize the induced V2a neurons, given sufficient time and focus. One of the first observations that I made was that LHX3 seemed just as likely to produce HB9 (MNX1) expression as it was to produce VSX2 expression. Since these transcription factors mutually antagonize one another (Clovis et al., 2016), addition of a shRNA against HB9 could improve the percent of cells expressing VSX2. Another hypothesis is that I did not keep DOX in the media for long enough and that 14 days of DOX as opposed to 4 would result in more stable identity. Of course, this likely still leaves you with an induced neuron that barely resembles *bona fide* V2a interneurons. Expression of PHOX2B and POU4F1 have also been observed in NGN2-only induced neurons (Lin et al., 2021). This observation indicates that some of the off-target genes that I observed in the V2a populations are the result of NGN2 expression and not due to retinoic acid treatment or LHX3. NGN2 may be too much of a sledgehammer in this context and screening other bHLH proteins could be one way to find a more relevant transcription factor with fewer off-target genes. Another route entirely would be to use a minimal patterning step in stem cells with dual SMAD inhibition and CHIR, then to induce expression of transcription factors that pattern the neural tube. This could include a combination of PAX6, IRX3, and NXK6.1, which in combination would delineate the p2 domain *in vivo*. Neurogenesis and V2a identity would then be promoted by DAPT during maturation.

I have also explored the possibility of generating V2b cells. The problem with this sister population is that V2b generation requires activated Notch signaling. Notch signaling between cells is contact dependent, with the receptor and ligand being located on the cell surface. Robust activation of the Notch receptor typically requires some form of mechanical tension to induce its surface and plasma membrane cleavages and allow signal transduction to occur. For this reason, no readily commercially available Notch agonist exists. One way to get around this is by specifically expressing the part of the Notch receptor that goes into the nucleus and changes gene expression: the notch intracellular domain (NICD). I ordered an inducible NICD construct off Addgene (Plasmid #130934) and incorporated it into some stem cells. These stem cells showed strong upregulation of Notch target genes with DOX addition. In collaboration with Dr. Lana Zholudeva, we differentiated these stem cells along the V2a route until day 15, then replaced the standard DAPT treatment with either DMSO, DAPT, or DOX and collected RNA at day 17. In hindsight, this was a late time point to perform the experiment, but we did see a decrease of VSX2 expression with DAPT > DMSO > DOX, and a strong increase in the expression of a transcription factor called TAL1 which is specific to the V2b lineage with DAPT < DMSO < DOX. This is a promising first pass and showed that even stem cells which had been differentiated for two weeks did not silence the NICD construct. In future studies, the use of DAPT could confound V2b differentiations. In V2a differentiations its role is twofold: it inhibits the V2b lineage and also speeds up cell cycle progression to push cells to become neurons. Without DAPT, I doubt we would get post-mitotic neurons as fast as we do. In a context where you want V2b neurons, either the timing of DAPT will have to be controlled such that a critical window is skipped, or DAPT could be replaced with other small molecules that are being described to promote neuron maturation (Hergenreder et al., 2024).

The inducible NICD cell line could have another use in the generation of glial populations, and astroglia in particular. During development, neural progenitors first form neurons before switching to producing glia. The transition to gliogenesis has been shown to be dependent on activated Notch signaling (Rowitch & Kriegstein, 2010). Since neurogenesis is exhausted first, existing protocols to derive glia, such as astrocytes and oligodendrocytes rely on long differentiations lasting two to three months. Controlled Notch activation could rapidly advance this process, as could the expression of key transcription factors such as NFIA and SOX9 or activation of signaling pathways like Jak/Stat (Wang et al., 2014). There is a need for the development of more rapid and reliable glial populations for disease modeling and I think this could be an exciting avenue of future work. Regardless of the cell type, cell engineering work should be approached with a touch of humility. The cell will have the ultimate say in what it becomes, and the natural process of development has been refined over eons to not skip the important stuff.

Final word

Over the course of my doctoral work, I have been a part of several collaborations, started many side projects, and pitched even more. While I cannot claim that it helped me get to graduation any sooner, I do believe that my willingness to try new things and to pitch new ideas has made me a better scientist. Given unlimited time and resources, I would be more than happy to continue to build on the work presented here and to try all of the experiments that I just outlined above. If that cannot be the case, then I hope that some other brave soul takes interest some part of it and takes it in on their own long, rambling, beautiful journey.

References

Ahuja, C. S., Nori, S., Tetreault, L., Wilson, J., Kwon, B., Harrop, J., et al. (2017). Traumatic spinal cord injury-repair and regeneration. Neurosurgery 80, S9–S22. doi: 10.1093/neuros/nyw080

Aires, R., de Lemos, L., Nóvoa, A., Jurberg, A. D., Mascrez, B., Duboule, D., & Mallo, M. (2019). Tail bud progenitor activity relies on a network comprising gdf11, lin28, and hox13 genes. Developmental Cell, 48(3), 383-395.e8. https://doi.org/10.1016/j.devcel.2018.12.004

Alshawaf, A. J., Viventi, S., Qiu, W., D'Abaco, G., Nayagam, B., Erlichster, M., et al. (2018). Phenotypic and functional characterization of peripheral sensory neurons derived from human embryonic stem cells. Sci. Rep. 8:603. doi: 10.1038/s41598-017-19093-0

Amin, S., Neijts, R., Simmini, S., Van Rooijen, C., Tan, S. C., Kester, L., Van Oudenaarden, A., Creyghton, M. P. and Deschamps, J. (2016). Cdx and T Brachyury Co-activate growth signaling in the embryonic axial progenitor niche. Cell Rep. 17, 3165-3177. https://doi.org/10.1016/j.celrep.2016.11.069

Amoroso, M. W., Croft, G. F., Williams, D. J., O'keeffe, S., Carrasco, M. A., Davis, A. R., Roybon, L., Oakley, D. H., Maniatis, T., Henderson, C. E. et al. (2013). Accelerated high-yield generation of limb-innervating motor neurons from human stem cells. J. Neurosci. 33, 574-586. https://doi.org/10.1523/JNEUROSCI.0906-12.2013

Ampatzis, K., Song, J., Ausborn, J., & El Manira, A. (2014). Separate Microcircuit Modules of Distinct V2a Interneurons and Motoneurons Control the Speed of Locomotion. Neuron, 83(4), 934–943. https://doi.org/10.1016/j.neuron.2014.07.018

Andersen, J., Revah, O., Miura, Y., Thom, N., Amin, N. D., Kelley, K. W., et al. (2020). Generation of functional human 3D cortico-motor assembloids. Cell 183, 1913–1929.e26. doi: 10.1016/j.cell.2020.11.017

Andrews, M. G., Kong, J., Novitch, B. G., & Butler, S. J. (2019). New perspectives on the mechanisms establishing the dorsal-ventral axis of the spinal cord. Current Topics in Developmental Biology, 132, 417–450. https://doi.org/10.1016/bs.ctdb.2018.12.010

Arlotta, P., and Hobert, O. (2015). Homeotic transformations of neuronal cell identities. Trends Neurosci. 38, 751–762. doi: 10.1016/j.tins.2015.10.005

Ashton, R., Lippmann, E., Estevez-Silva, M., and Ashton, R. (2015). Chemically defined differentiation of human pluripotent stem cells to hindbrain and spinal cord neural stem cells with defined regional identities. Protoc. Exch. 2015:76. doi: 10.1038/protex.2015.076

Assinck, P., Duncan, G. J., Hilton, B. J., Plemel, J. R., and Tetzlaff, W. (2017). Cell transplantation therapy for spinal cord injury. Nat. Neurosci. 20, 637–647. doi: 10.1038/nn.4541

Azim, E., Jiang, J., Alstermark, B. and Jessell, T. M. (2014). Skilled reaching relies on a V2a propriospinal internal copy circuit. Nature 508, 357-363. https://doi.org/10.1038/nature13021

Azimi, S. M., Sheridan, S. D., Ghannad-Rezaie, M., Eimon, P. M., and Yanik, M. F. (2018). Combinatorial programming of human neuronal progenitors using magnetically-guided stoichiometric mRNA delivery. eLife 7:31922. doi: 10.7554/eLife.31922

Bartel, D. P. (2004). MicroRNAs: Genomics, biogenesis, mechanism, and function. Cell 116, 281–297. doi: 10.1016/s0092-8674(04)00045-5

Beccari, L., Moris, N., Girgin, M., Turner, D. A., Baillie-Johnson, P., Cossy, A.-C., Lutolf, M. P., Duboule, D., & Arias, A. M. (2018). Multi-axial self-organization properties of mouse embryonic stem cells into gastruloids. Nature, 562(7726), 272–276. https://doi.org/10.1038/s41586-018-0578-0

Beck, F., Erler, T., Russell, A. and James, R. (1995). Expression of Cdx-2 in the mouse embryo and placenta: possible role in patterning of the extra-embryonic membranes. Dev. Dyn. 204, 219-227. https://doi.org/10.1002/aja.1002040302

Beddington, R. S. P. and Robertson, E. J. (1999). Axis development and early asymmetry in mammals. Cell 96, 195-209. https://doi.org/10.1016/S0092-8674(00)80560-7

Bel-Vialar, S., Itasaki, N. and Krumlauf, R. (2002). Initiating Hox gene expression: in the early chick neural tube differential sensitivity to FGF and RA signaling subdivides the HoxB genes in two distinct groups. Development 129, 5103-5115. https://doi.org/10.1242/dev.129.22.5103

Bénazéraf, B., & Pourquié, O. (2013). Formation and Segmentation of the Vertebrate Body Axis. Annual Review of Cell and Developmental Biology, 29(Volume 29, 2013), 1–26. https://doi.org/10.1146/annurev-cellbio-101011-155703

Berninger, B., Costa, M. R., Koch, U., Schroeder, T., Sutor, B., Grothe, B., et al. (2007). Functional properties of neurons derived from in vitro reprogrammed postnatal astroglia. J. Neurosci. 27, 8654–8664. doi: 10.1523/JNEUROSCI.1615-07.2007

Bershteyn, M., Nowakowski, T. J., Pollen, A. A., Di Lullo, E., Nene, A., Wynshaw-Boris, A., et al. (2017). Human iPSC-derived cerebral organoids model cellular features of lissencephaly and reveal prolonged mitosis of outer radial glia. Cell Stem Cell 20, 435–449.e4. doi: 10.1016/j.stem.2016.12.007

Bhaduri, A., Andrews, M. G., Mancia Leon, W., Jung, D., Shin, D., Allen, D., et al. (2020). Cell stress in cortical organoids impairs molecular subtype specification. Nature 578, 142–148. doi: 10.1038/s41586-020-1962-0

Birey, F., Li, M.-Y., Gordon, A., Thete, M. V., Valencia, A. M., Revah, O., et al. (2022). Dissecting the molecular basis of human interneuron migration in forebrain assembloids from timothy syndrome. Cell Stem Cell 29, 248–264.e7. doi: 10.1016/j.stem.2021.11.011

Blin, G., Wisniewski, D., Picart, C., Thery, M., Puceat, M. and Lowell, S. (2018). Geometrical confinement controls the asymmetric patterning of brachyury in cultures of pluripotent cells. Development 145, dev166025. https://doi.org/10.1242/dev.166025

Bocchi, R., Masserdotti, G., and Götz, M. (2022). Direct neuronal reprogramming: Fast forward from new concepts toward therapeutic approaches. Neuron 110, 366–393. doi: 10.1016/j.neuron.2021.11.023

Bonner, J. F., & Steward, O. (2015). Repair of spinal cord injury with neuronal relays: From fetal grafts to neural stem cells. Brain Research, 1619, 115–123. https://doi.org/10.1016/j.brainres.2015.01.006

Borghese, L., Dolezalova, D., Opitz, T., Haupt, S., Leinhaas, A., Steinfarz, B., et al. (2010). Inhibition of notch signaling in human embryonic stem cell-derived neural stem cells delays G1/S phase transition and accelerates neuronal differentiation in vitro and in vivo. Stem Cells 28, 955–964. doi: 10.1002/stem.408

Boulting, G. L., Kiskinis, E., Croft, G. F., Amoroso, M. W., Oakley, D. H., Wainger, B. J., et al. (2011). A functionally characterized test set of human induced pluripotent stem cells. Nat. Biotechnol. 29, 279–286. doi: 10.1038/nbt.1783

Briscoe, J. and Ericson, J. (1999). The specification of neuronal identity by graded sonic hedgehog signalling. Semin. Cell Dev. Biol. 10, 353-362. https://doi.org/10.1006/scdb.1999.0295

Broutier, L., Andersson-Rolf, A., Hindley, C. J., Boj, S. F., Clevers, H., Koo, B.-K. and Huch, M. (2016). Culture and establishment of self-renewing human and mouse adult liver and pancreas 3D organoids and their genetic manipulation. Nat. Protoc. 11, 1724-1743. https://doi.org/10.1038/nprot.2016.097

Bubnys, A., Kandel, H., Kao, L. M., Pfaff, D., & Tabansky, I. (2019). Hindbrain v2a neurons pattern rhythmic activity of motor neurons in a reticulospinal coculture. Frontiers in Neuroscience, 13, 1077. https://doi.org/10.3389/fnins.2019.01077

Bulajić, M., Srivastava, D., Dasen, J. S., Wichterle, H., Mahony, S., and Mazzoni, E. O. (2020). Differential abilities to engage inaccessible chromatin diversify vertebrate hox binding patterns. Development 147:194761. doi: 10.1242/dev.194761

Bulger, E. A., McDevitt, T. C., & Bruneau, B. G. (2024). CDX2 dose-dependently influences the gene regulatory network underlying human extraembryonic mesoderm development. Biology Open, 13(3), bio060323. https://doi.org/10.1242/bio.060323

Bulger, E. A., Muncie-Vasic, I., Libby, A. R. G., McDevitt, T. C., & Bruneau, B. G. (2024). TBXT dose sensitivity and the decoupling of nascent mesoderm specification from EMT progression in 2D human gastruloids. Development (Cambridge, England), 151(6), dev202516. https://doi.org/10.1242/dev.202516

Busskamp, V., Lewis, N. E., Guye, P., Ng, A. H. M., Shipman, S. L., Byrne, S. M., et al. (2014). Rapid neurogenesis through transcriptional activation in human stem cells. Mol. Syst. Biol. 10:760. doi: 10.15252/msb.20145508

Butler, A., Hoffman, P., Smibert, P., Papalexi, E. and Satija, R. (2018). Integrating single-cell transcriptomic data across different conditions, technologies, and species. Nat. Biotechnol. 36, 411-420. https://doi.org/10.1038/nbt.4096

Butts, J. C., Iyer, N., White, N., Thompson, R., Sakiyama-Elbert, S., & McDevitt, T. C. (2019). V2a interneuron differentiation from mouse and human pluripotent stem cells. Nature Protocols, 14(11), Article 11. https://doi.org/10.1038/s41596-019-0203-1

Butts, J. C., McCreedy, D. A., Martinez-Vargas, J. A., Mendoza-Camacho, F. N., Hookway, T. A., Gifford, C. A., et al. (2017). Differentiation of V2a interneurons from human pluripotent stem cells. Proc. Natl. Acad. Sci. U.S.A. 114, 4969–4974. doi: 10.1073/pnas.1608254114

Cambray, N. and Wilson, V. (2002). Axial progenitors with extensive potency are localised to the mouse chordoneural hinge. 129, Development 4855-4866. https://doi.org/10.1242/dev.129.20.4855

Cambray, N., & Wilson, V. (2007). Two distinct sources for a population of maturing axial progenitors. Development, 134(15), 2829–2840. https://doi.org/10.1242/dev.02877

Camus, A., Perea-Gomez, A., Moreau, A., and Collignon, J. (2006). Absence of nodal signaling promotes precocious neural differentiation in the mouse embryo. Dev. Biol. 295, 743–755. doi: 10.1016/j.ydbio.2006.03.047

Cao, F., Xie, X., Gollan, T., Zhao, L., Narsinh, K., Lee, R. J., et al. (2010). Comparison of gene-transfer efficiency in human embryonic stem cells. Mol. Imaging Biol. 12, 15–24. doi: 10.1007/s11307-009-0236-x

Carmel, J. B., and Martin, J. H. (2014). Motor cortex electrical stimulation augments sprouting of the corticospinal tract and promotes recovery of motor function. Front. Integr. Neurosci. 8:51. doi: 10.3389/fnint.2014.00051

Carpenedo, R. L., Sargent, C. Y., & McDevitt, T. C. (2007). Rotary suspension culture enhances the efficiency, yield, and homogeneity of embryoid body differentiation. Stem Cells, 25(9), 2224–2234. https://doi.org/10.1634/stemcells.2006-0523

Carpenter, E. M. (2002). Hox genes and spinal cord development. Dev. Neurosci. 24, 24-34. https://doi.org/10.1159/000064943

Chambers, S. M., Fasano, C. A., Papapetrou, E. P., Tomishima, M., Sadelain, M., and Studer, L. (2009). Highly efficient neural conversion of human ES and iPS cells by dual inhibition of SMAD signaling. Nat. Biotechnol. 27, 275–280. doi: 10.1038/nbt.1529

Chambers, S. M., Qi, Y., Mica, Y., Lee, G., Zhang, X.-J., Niu, L., et al. (2012). Combined small-molecule inhibition accelerates developmental timing and converts human pluripotent stem cells into nociceptors. Nat. Biotechnol. 30, 715–720. doi: 10.1038/nbt.2249

Chapman, D. L. and Papaioannou, V. E. (1998). Three neural tubes in mouse embryos with mutations in the T-box gene Tbx6. Nature 391, 695-697. https://doi.org/10.1038/35624

Chen, J.-A., Huang, Y.-P., Mazzoni, E. O., Tan, G. C., Zavadil, J., and Wichterle, H. (2011). Mir-17-3p controls spinal neural progenitor patterning by regulating Olig2/Irx3 cross-repressive loop. Neuron 69, 721–735. doi: 10.1016/j.neuron.2011.01.014

Chen, M., Maimaitili, M., Habekost, M., Gill, K. P., Mermet-Joret, N., Nabavi, S., et al. (2020). Rapid generation of regionally specified CNS neurons by sequential patterning and conversion of human induced pluripotent stem cells. Stem Cell Res. 48:101945. doi: 10.1016/j.scr.2020.101945

Chesley, P. (1935). Development of the short-tailed mutant in the house mouse. J. Exp. Zool. 70, 429-459. https://doi.org/10.1002/jez.1400700306

Cho, K. W., & De Robertis, E. M. (1990). Differential activation of Xenopus homeo box genes by mesoderm-inducing growth factors and retinoic acid. Genes & Development, 4(11), 1910–1916. https://doi.org/10.1101/gad.4.11.1910

Clovis, Y. M., Seo, S. Y., Kwon, J.-S., Rhee, J. C., Yeo, S., Lee, J. W., Lee, S., & Lee, S.-K. (2016). Chx10 Consolidates V2a Interneuron Identity through Two Distinct Gene Repression Modes. Cell Reports, 16(6), 1642–1652. https://doi.org/10.1016/j.celrep.2016.06.100

Conese, M., Auriche, C., and Ascenzioni, F. (2004). Gene therapy progress and prospects: episomally maintained self-replicating systems. Gene Ther. 11, 1735–1741. doi: 10.1038/sj.gt.3302362

Cooper, F., Gentsch, G. E., Mitter, R., Bouissou, C., Healy, L., Rodriguez, A. H., Smith, J. C., & Bernardo, A. S. (2020). Rostrocaudal patterning and neural crest differentiation of human pre-neural spinal cord progenitors in vitro. BioRxiv. https://doi.org/10.1101/2020.06.16.155564

Crone, S. A., Quinlan, K. A., Zagoraiou, L., Droho, S., Restrepo, C. E., Lundfald, L., Endo, T., Setlak, J., Jessell, T. M., Kiehn, O. et al. (2008). Genetic ablation of V2a ipsilateral interneurons disrupts left-right locomotor coordination in mammalian spinal cord. Neuron 60, 70-83. https://doi.org/10.1016/j.neuron.2008.08.009

Crone, S. A., Viemari, J.-C., Droho, S., Mrejeru, A., Ramirez, J.-M., and Sharma, K. (2012). Irregular breathing in mice following genetic ablation of V2a neurons. J. Neurosci. 32, 7895–7906. doi: 10.1523/JNEUROSCI.0445-12.2012

Crone, S. A., Zhong, G., Harris-Warrick, R., & Sharma, K. (2009). In mice lacking V2a interneurons, gait depends on speed of locomotion. The Journal of Neuroscience, 29(21), 7098–7109. https://doi.org/10.1523/JNEUROSCI.1206-09.2009

Cruz, C., Ribes, V., Kutejova, E., Cayuso, J., Lawson, V., Norris, D., Stevens, J., Davey, M., Blight, K., Bangs, F., Mynett, A., Hirst, E., Chung, R., Balaskas, N., Brody, S. L., Marti, E., & Briscoe, J. (2010). Foxj1 regulates floor plate cilia architecture and modifies the response of cells to sonic hedgehog signalling. Development, 137(24), 4271–4282. https://doi.org/10.1242/dev.051714

Dasen, J. S., & Jessell, T. M. (2009). Chapter Six Hox Networks and the Origins of Motor Neuron Diversity. In Hox Genes (Vol. 88, pp. 169–200). Elsevier. https://doi.org/10.1016/S0070-2153(09)88006-X

Dasen, J. S., Tice, B. C., Brenner-Morton, S., and Jessell, T. M. (2005). A hox regulatory network establishes motor neuron pool identity and target-muscle connectivity. Cell 123, 477–491. doi: 10.1016/j.cell.2005.09.009

De Santis, R., Garone, M. G., Pagani, F., de Turris, V., Di Angelantonio, S., and Rosa, A. (2018). Direct conversion of human pluripotent stem cells into cranial motor neurons using a piggyBac vector. Stem Cell Res. 29, 189–196. doi: 10.1016/j.scr.2018.04.012

Debrulle, S., Baudouin, C., Hidalgo-Figueroa, M., Pelosi, B., Francius, C., Rucchin, V., Ronellenfitch, K., Chow, R. L., Tissir, F., Lee, S.-K., & Clotman, F. (2019). Vsx1 and Chx10 paralogs sequentially secure V2 interneuron identity during spinal cord development. Cellular and Molecular Life Sciences. https://doi.org/10.1007/s00018-019-03408-7

Del Barrio, M. G., Taveira-Marques, R., Muroyama, Y., Yuk, D.-I., Li, S., Wines-Samuelson, M., Shen, J., Smith, H. K., Xiang, M., Rowitch, D., & Richardson, W. D. (2007). A regulatory network involving Foxn4, Mash1 and delta-like 4/Notch1 generates V2a and V2b spinal interneurons from a common progenitor pool. Development, 134(19), 3427–3436. https://doi.org/10.1242/dev.005868

Denans, N., Iimura, T., & Pourquié, O. (2015). Hox genes control vertebrate body elongation by collinear Wnt repression. eLife, 4(e04379). https://doi.org/10.7554/eLife.04379

Denham, M., Hasegawa, K., Menheniott, T., Rollo, B., Zhang, D., Hough, S., et al. (2015). Multipotent caudal neural progenitors derived from human pluripotent stem cells that give rise to lineages of the central and peripheral nervous system. Stem Cells 33, 1759–1770. doi: 10.1002/stem.1991

Deschamps, J., and Duboule, D. (2017). Embryonic timing, axial stem cells, chromatin dynamics, and the hox clock. Genes Dev. 31, 1406–1416. doi: 10.1101/gad.303123.117

Dessaud, E., McMahon, A. P., & Briscoe, J. (2008). Pattern formation in the vertebrate neural tube: A sonic hedgehog morphogen-regulated transcriptional network. Development, 135(15), 2489–2503. https://doi.org/10.1242/dev.009324

Diez Del Corral, R. and Storey, K. G. (2004). Opposing FGF and retinoid pathways: a signalling switch that controls differentiation and patterning onset in the extending vertebrate body axis. BioEssays 26, 857-869. https://doi.org/10.1002/bies.20080

Doi, D., Magotani, H., Kikuchi, T., Ikeda, M., Hiramatsu, S., Yoshida, K., et al. (2020). Pre-clinical study of induced pluripotent stem cell-derived dopaminergic progenitor cells for Parkinson's disease. Nat. Commun. 11:3369. doi: 10.1038/s41467-020-17165-w

Eiraku, M., Takata, N., Ishibashi, H., Kawada, M., Sakakura, E., Okuda, S., Sekiguchi, K., Adachi, T. and Sasai, Y. (2011). Self-organizing optic-cup morphogenesis in three-dimensional culture. Nature 472, 51-56. https://doi.org/10.1038/nature09941

Eiraku, M., Watanabe, K., Matsuo-Takasaki, M., Kawada, M., Yonemura, S., Matsumura, M., Wataya, T., Nishiyama, A., Muguruma, K., & Sasai, Y. (2008). Self-organized formation of polarized cortical tissues from ESCs and its active manipulation by extrinsic signals. Cell Stem Cell, 3(5), 519–532. https://doi.org/10.1016/j.stem.2008.09.002

Elder, N., Fattahi, F., McDevitt, T. C., & Zholudeva, L. V. (2022). Diseased, differentiated and difficult: Strategies for improved engineering of in vitro neurological systems. Frontiers in Cellular Neuroscience, 16. https://www.frontiersin.org/articles/10.3389/fncel.2022.962103

English, A. W., Berglund, K., Carrasco, D., Goebel, K., Gross, R. E., Isaacson, R., et al. (2021). Bioluminescent optogenetics: A novel experimental therapy to promote axon regeneration after peripheral nerve injury. Int. J. Mol. Sci. 22:217. doi: 10.3390/ijms22137217

Erb, M., Lee, B., Yeon Seo, S., Lee, J. W., Lee, S., and Lee, S.-K. (2017). The isl1-Lhx3 complex promotes motor neuron specification by activating transcriptional pathways that enhance its own expression and formation. eNeuro 4:2017. doi: 10.1523/ENEURO.0349-16.2017

Ericson, J. Fischer, C., Urzi, A., Vidal, R., Kunz, S., Ruffault, P.-L., Kabuss, L., Hube, I., Gazzerro, E. and Birchmeier, C. et al. (1997). Graded sonic hedgehog signaling and the specification of cell fate in the ventral neural tube. Cold Spring Harbor Symp. Quant. Biol. 62, 451-466. https://doi.org/10.1101/SQB.1997.062.01.053

Fang, Z., Liu, X., and Peltz, G. (2023). GSEApy: a comprehensive package for performing gene set enrichment analysis in Python. Bioinformatics 39, btac757. https://doi.org/10.1093/bioinformatics/btac757.

Fattahi, F., Steinbeck, J. A., Kriks, S., Tchieu, J., Zimmer, B., Kishinevsky, S., et al. (2016). Deriving human ENS lineages for cell therapy and drug discovery in hirschsprung disease. Nature 531, 105–109. doi: 10.1038/nature16951

Faustino Martins, J.-M., Fischer, C., Urzi, A., Vidal, R., Kunz, S., Ruffault, P.-L., Kabuss, L., Hube, I., Gazzerro, E., Birchmeier, C. et al. (2020). Self-organizing 3D human trunk neuromuscular organoids. Cell Stem Cell 26, 172-186.e6. https://doi.org/10.1016/j.stem.2019.12.007

Feliciano, C. M., Wu, K., Watry, H. L., Marley, C. B. E., Ramadoss, G. N., Ghanim, H. Y., et al. (2021). Allele-specific gene editing rescues pathology in a human model of charcot-marie-tooth disease type 2E. Front. Cell Dev. Biol. 9:723023. doi: 10.3389/fcell.2021.723023

Feng, W., Li, Y., and Kratsios, P. (2021). Emerging roles for hox proteins in the last steps of neuronal development in worms, flies, and mice. Front. Neurosci. 15:801791. doi: 10.3389/fnins.2021.801791

Fernandopulle, M. S., Prestil, R., Grunseich, C., Wang, C., Gan, L., and Ward, M. E. (2018). Transcription factor-mediated differentiation of human iPSCs into neurons. Curr. Protoc. Cell Biol. 79:e51. doi: 10.1002/cpcb.51

Fischer, I., Dulin, J. N., and Lane, M. A. (2020). Transplanting neural progenitor cells to restore connectivity after spinal cord injury. Nat. Rev. Neurosci. 21, 366–383. doi: 10.1038/s41583-020-0314-2

Flitsch, L. J., Laupman, K. E., and Brüstle, O. (2020). Transcription factor-based fate specification and forward programming for neural regeneration. Front. Cell. Neurosci. 14:121. doi: 10.3389/fncel.2020.00121

Frank, D., and Sela-Donenfeld, D. (2019). Hindbrain induction and patterning during early vertebrate development. Cell. Mol. Life Sci. 76, 941–960. doi: 10.1007/s00018-018-2974-x

Fujii, M., Matano, M., Nanki, K. and Sato, T. (2015). Efficient genetic engineering of human intestinal organoids using electroporation. Nat. Protoc. 10, 1474-1485. https://doi.org/10.1038/nprot.2015.088

Gascón, S., Murenu, E., Masserdotti, G., Ortega, F., Russo, G. L., Petrik, D., et al. (2016). Identification and successful negotiation of a metabolic checkpoint in direct neuronal reprogramming. Cell Stem Cell 18, 396–409. doi: 10.1016/j.stem.2015.12.003

Giraldo, E., Palmero-Canton, D., Martinez-Rojas, B., Sanchez-Martin, M. D. M., and Moreno-Manzano, V. (2020). Optogenetic modulation of neural progenitor cells improves neuroregenerative potential. Int. J. Mol. Sci. 22:10365. doi: 10.3390/ijms22010365

Gonzalez-Gobartt, E., Blanco-Ameijeiras, J., Usieto, S., Allio, G., Benazeraf, B. and Martí, E. (2021). Cell intercalation driven by SMAD3 underlies secondary neural tube formation. Dev. Cell 56, 1147-1163. https://doi.org/10.1016/j.devcel.2021.03.023

Goparaju, S. K., Kohda, K., Ibata, K., Soma, A., Nakatake, Y., Akiyama, T., et al. (2017). Rapid differentiation of human pluripotent stem cells into functional neurons by mRNAs encoding transcription factors. Sci. Rep. 7:42367. doi: 10.1038/srep42367

Goto, K., Imamura, K., Komatsu, K., Mitani, K., Aiba, K., Nakatsuji, N., et al. (2017). Simple derivation of spinal motor neurons from ESCs/iPSCs using sendai virus vectors. Mol. Ther. Methods Clin. Dev. 4, 115–125. doi: 10.1016/j.omtm.2016.12.007

Gould, A., Itasaki, N., & Krumlauf, R. (1998). Initiation of rhombomeric Hoxb4 expression requires induction by somites and a retinoid pathway. Neuron, 21(1), 39–51. https://doi.org/10.1016/s0896-6273(00)80513-9

Gouti, M., Metzis, V., & Briscoe, J. (2015). The route to spinal cord cell types: A tale of signals and switches. Trends Genet, 31(6), 282–289. https://doi.org/10.1016/j.tig.2015.03.001

Gouti, M., Tsakiridis, A., Wymeersch, F. J., Huang, Y., Kleinjung, J., Wilson, V., & Briscoe, J. (2014). In vitro generation of neuromesodermal progenitors reveals distinct roles for wnt signalling in the specification of spinal cord and paraxial mesoderm identity. PLoS Biology, 12(8), e1001937. https://doi.org/10.1371/journal.pbio.1001937

Grady, L. (2006). Random walks for image segmentation. IEEE Trans. Pattern Anal. Mach. Intell. 28, 1768-1783.

Guibentif, C., Griffiths, J. A., Imaz-Rosshandler, I., Ghazanfar, S., Nichols, J., Wilson, V., Göttgens, B. and Marioni, J. C. (2021). Diverse routes toward early somites in the mouse embryo. Dev. Cell 56, 141-153.e6. https://doi.org/10.1016/j.devcel.2020.11.013

Guo, C., and Morris, S. A. (2017). Engineering cell identity: establishing new gene regulatory and chromatin landscapes. Curr. Opin. Genet. Dev. 46, 50–57. doi: 10.1016/j.gde.2017.06.011

Hagey, D. W., Zaouter, C., Combeau, G., Lendahl, M. A., Andersson, O., Huss, M., et al. (2016). Distinct transcription factor complexes act on a permissive chromatin landscape to establish regionalized gene expression in CNS stem cells. Genome Res. 26, 908–917. doi: 10.1101/gr.203513.115

Halir, R. and Flusser, J. (2020). Numerically stable direct least squares fitting of ellipses. In Proc. 6th International Conference in Central Europe on Computer Graphics and Visualization. WSCG 98, 125-132.

Hay, E. D. and Meier, S. (1974). Glycosaminoglycan synthesis by embryonic inductors: neural tube, notochord, and lens. J. Cell Biol. 62, 889-898. https://doi.org/10.1083/jcb.62.3.889

Hayashi, M., Hinckley, C. A., Driscoll, S. P., Moore, N. J., Levine, A. J., Hilde, K. L., Sharma, K., & Pfaff, S. L. (2018). Graded arrays of spinal and supraspinal v2a interneuron subtypes underlie forelimb and hindlimb motor control. Neuron, 97(4), 869-884.e5. https://doi.org/10.1016/j.neuron.2018.01.023

Henrique, D., Abranches, E., Verrier, L., & Storey, K. G. (2015). Neuromesodermal progenitors and the making of the spinal cord. Development, 142(17), 2864–2875. https://doi.org/10.1242/dev.119768

Hergenreder, E., Minotti, A. P., Zorina, Y., Oberst, P., Zhao, Z., Munguba, H., Calder, E. L., Baggiolini, A., Walsh, R. M., Liston, C., Levitz, J., Garippa, R., Chen, S., Ciceri, G., & Studer, L. (2024). Combined small-molecule treatment accelerates maturation of human pluripotent stem cell-derived neurons. Nature Biotechnology. https://doi.org/10.1038/s41587-023-02031-z

Hoang, P. T., Chalif, J. I., Bikoff, J. B., Jessell, T. M., Mentis, G. Z., and Wichterle, H. (2018). Subtype diversification and synaptic specificity of stem cell-derived spinal interneurons. Neuron 100, 135–149.e7. doi: 10.1016/j.neuron.2018.09.016

Hookway, T. A., Butts, J. C., Lee, E., Tang, H. and Mcdevitt, T. C. (2016). Aggregate formation and suspension culture of human pluripotent stem cells and differentiated progeny. Methods 101, 11-20. https://doi.org/10.1016/j.ymeth.2015.11.027

Hulme, A. J., Maksour, S., St-Clair Glover, M., Miellet, S., and Dottori, M. (2022). Making neurons, made easy: The use of neurogenin-2 in neuronal differentiation. Stem Cell Rep. 11:15. doi: 10.1016/j.stemcr.2021.11.015

Hyysalo, A., Ristola, M., Mäkinen, M. E.-L., Häyrynen, S., Nykter, M., and Narkilahti, S. (2017). Laminin $\alpha 5$ substrates promote survival, network formation and functional development of human pluripotent stem cell-derived neurons in vitro. Stem Cell Res. 24, 118–127. doi: 10.1016/j.scr.2017.09.002

Iimura, T., & Pourquié, O. (2006). Collinear activation of Hoxb genes during gastrulation is linked to mesoderm cell ingression. Nature, 442(7102), 568–571. https://doi.org/10.1038/nature04838

Jessell, T. M. (2000). Neuronal specification in the spinal cord: Inductive signals and transcriptional codes. Nature Reviews Genetics, 1(1), Article 1. https://doi.org/10.1038/35049541

Joshi, K., Lee, S., Lee, B., Lee, J. W., and Lee, S.-K. (2009). LMO4 controls the balance between excitatory and inhibitory spinal V2 interneurons. Neuron 61, 839–851. doi: 10.1016/j.neuron.2009.02.011

Jung, H., Mazzoni, E. O., Soshnikova, N., Hanley, O., Venkatesh, B., Duboule, D., et al. (2014). Evolving hox activity profiles govern diversity in locomotor systems. Dev. Cell 29, 171–187. doi: 10.1016/j.devcel.2014.03.008

Kadoshima, T., Sakaguchi, H., Nakano, T., Soen, M., Ando, S., Eiraku, M., et al. (2013). Self-organization of axial polarity, inside-out layer pattern, and species-specific progenitor dynamics in human ES cell-derived neocortex. Proc. Natl. Acad. Sci. U.S.A. 110, 20284–20289. doi: 10.1073/pnas.1315710110

Kadoya, K., Lu, P., Nguyen, K., Lee-Kubli, C., Kumamaru, H., Yao, L., Knackert, J., Poplawski, G., Dulin, J. N., Strobl, H., Takashima, Y., Biane, J., Conner, J., Zhang, S.-C., & Tuszynski, M. H. (2016). Spinal cord reconstitution with homologous neural grafts enables robust corticospinal regeneration. Nature Medicine, 22(5), 479–487. https://doi.org/10.1038/nm.4066

Kamimoto, K., Stringa, B., Hoffmann, C. M., Jindal, K., Solnica-Krezel, L., & Morris, S. A. (2023). Dissecting cell identity via network inference and in silico gene perturbation. Nature, 614(7949), 742–751. https://doi.org/10.1038/s41586-022-05688-9

Karzbrun, E., Khankhel, A. H., Megale, H. C., Glasauer, S. M. K., Wyle, Y., Britton, G., Warmflash, A., Kosik, K. S., Siggia, E. D., Shraiman, B. I., & Streichan, S. J. (2021). Human neural tube morphogenesis in vitro by geometric constraints. Nature, 599(7884), 268–272. https://doi.org/10.1038/s41586-021-04026-9

Kathe, C., Skinnider, M. A., Hutson, T. H., Regazzi, N., Gautier, M., Demesmaeker, R., Komi, S., Ceto, S., James, N. D., Cho, N., Baud, L., Galan, K., Matson, K. J. E., Rowald, A., Kim, K., Wang, R., Minassian, K., Prior, J. O., Asboth, L., … Courtine, G. (2022). The neurons that restore walking after paralysis. Nature, 611(7936), 540–547. https://doi.org/10.1038/s41586-022-05385-7

Kaul, H., Werschler, N., Jones, R. D., Siu, M. M., Tewary, M., Hagner, A., Ostblom, J., Aguilar-Hidalgo, D., & Zandstra, P. W. (2023). Virtual cells in a virtual microenvironment recapitulate early development-like patterns in human pluripotent stem cell colonies. Stem Cell Reports, 18(1), 377–393. https://doi.org/10.1016/j.stemcr.2022.10.004

Kelly, T. K., Karsten, S. L., Geschwind, D. H., and Kornblum, H. I. (2009). Cell lineage and regional identity of cultured spinal cord neural stem cells and comparison to brain-derived neural stem cells. PLoS One 4:e4213. doi: 10.1371/journal.pone.0004213

Kempf, J., Knelles, K., Hersbach, B. A., Petrik, D., Riedemann, T., Bednarova, V., et al. (2021). Heterogeneity of neurons reprogrammed from spinal cord astrocytes by the proneural factors Ascl1 and Neurogenin2. Cell Rep. 36:109409. doi: 10.1016/j.celrep.2021.109409

Kerepesi, C., Zhang, B., Lee, S.-G., Trapp, A., and Gladyshev, V. N. (2021). Epigenetic clocks reveal a rejuvenation event during embryogenesis followed by aging. Sci. Adv. 7:6082. doi: 10.1126/sciadv.abg6082

Kim, D., Langmead, B. and Salzberg, S. L. (2015). HISAT: a fast spliced aligner with low memory requirements. Nat. Methods 12, 357-360. https://doi.org/10.1038/nmeth.3317

Kim, M., Habiba, A., Doherty, J. M., Mills, J. C., Mercer, R. W. and Huettner, J. E. (2009). Regulation of mouse embryonic stem cell neural differentiation by retinoic acid. Dev. Biol. 328, 456-471. https://doi.org/10.1016/j.ydbio.2009.02.001

Kim, T. W., Piao, J., Koo, S. Y., Kriks, S., Chung, S. Y., Betel, D., et al. (2021). Biphasic activation of WNT signaling facilitates the derivation of midbrain dopamine neurons from hESCs for translational Use. Cell Stem Cell 28, 343–355.e5. doi: 10.1016/j.stem.2021.01.005

Kriks, S., Shim, J.-W., Piao, J., Ganat, Y. M., Wakeman, D. R., Xie, Z., et al. (2011). Dopamine neurons derived from human ES cells efficiently engraft in animal models of Parkinson's disease. Nature 480, 547–551. doi: 10.1038/nature10648

Kumamaru, H., Kadoya, K., Adler, A. F., Takashima, Y., Graham, L., Coppola, G., & Tuszynski, M. H. (2018). Generation and post-injury integration of human spinal cord neural stem cells. Nature Methods, 15(9), 723–731. https://doi.org/10.1038/s41592-018-0074-3

Kwon, B. K., Tetzlaff, W., Grauer, J. N., Beiner, J., and Vaccaro, A. R. (2004). Pathophysiology and pharmacologic treatment of acute spinal cord injury. Spine J. 4, 451–464. doi: 10.1016/j.spinee.2003.07.007

Lancaster, M. A. and Knoblich, J. A. (2014). Organogenesis in a dish: Modeling development and disease using organoid technologies. Science 345, 1247125. https://doi.org/10.1126/science.1247125

Lancaster, M. A., Renner, M., Martin, C.-A., Wenzel, D., Bicknell, L. S., Hurles, M. E., et al. (2013). Cerebral organoids model human brain development and microcephaly. Nature 501, 373–379. doi: 10.1038/nature12517

Larson, M. H., Gilbert, L. A., Wang, X., Lim, W. A., Weissman, J. S. and Qi, L. S. (2013). CRISPR interference (CRISPRi) for sequence-specific control of gene expression. Nat. Protoc. 8, 2180-2196. https://doi.org/10.1038/nprot.2013.132

Latchoumane, C.-F. V., Jackson, L., Sendi, M. S. E., Tehrani, K. F., Mortensen, L. J., Stice, S. L., et al. (2018). Chronic electrical stimulation promotes the excitability and plasticity of ESC-derived neurons following glutamate-induced inhibition in vitro. Sci. Rep. 8:10957. doi: 10.1038/s41598-018-29069-3

Law, C. W., Chen, Y., Shi, W. and Smyth, G. K. (2014). voom: precision weights unlock linear model analysis tools for RNA-seq read counts. Genome Biol. 15, R29. https://doi.org/10.1186/gb-2014-15-2-r29

Lee, S., Cuvillier, J. M., Lee, B., Shen, R., Lee, J. W., and Lee, S.-K. (2012). Fusion protein Isl1-Lhx3 specifies motor neuron fate by inducing motor neuron genes and concomitantly suppressing the interneuron programs. Proc. Natl. Acad. Sci. U.S.A. 109, 3383–3388. doi: 10.1073/pnas.1114515109

Li, C.-J., Hong, T., Tung, Y.-T., Yen, Y.-P., Hsu, H.-C., Lu, Y.-L., et al. (2017). MicroRNA filters hox temporal transcription noise to confer boundary formation in the spinal cord. Nat. Commun. 8:14685. doi: 10.1038/ncomms14685

Li, S., Misra, K., Matise, M. P., & Xiang, M. (2005). Foxn4 acts synergistically with Mash1 to specify subtype identity of V2 interneurons in the spinal cord. Proceedings of the National Academy of Sciences of the United States of America, 102(30), 10688–10693. https://doi.org/10.1073/pnas.0504799102

Li, X.-J., Du, Z.-W., Zarnowska, E. D., Pankratz, M., Hansen, L. O., Pearce, R. A. and Zhang, S.-C. (2005). Specification of motoneurons from human embryonic stem cells Nature Biotechnology. Nat. Biotechnol. 23, 215-221. https://doi.org/10.1038/nbt1063

Liao, Y., Smyth, G. K. and Shi, W. (2014). featureCounts: an efficient general purpose program for assigning sequence reads to genomic features. Bioinformatics 30, 923-930. https://doi.org/10.1093/bioinformatics/btt656

Libby, A. R. G., Briers, D., Haghighi, I., Joy, D. A., Conklin, B. R., Belta, C., et al. (2019). Automated design of pluripotent stem cell self-organization. Cell Syst. 9, 483–495.e10. doi: 10.1016/j.cels.2019.10.008

Libby, A. R. G., Joy, D. A., Elder, N. H., Bulger, E. A., Krakora, M. Z., Gaylord, E. A., et al. (2021). Axial elongation of caudalized human organoids mimics aspects of neural tube development. Development 148:198275. doi: 10.1242/dev.198275

Libby, A. R., Joy, D. A., So, P.-L., Mandegar, M. A., Muncie, J. M., Mendoza-Camacho, F. N., et al. (2018). Spatiotemporal mosaic self-patterning of pluripotent stem cells using CRISPR interference. eLife 7:36045. doi: 10.7554/eLife.36045

Liem, K. F., Tremml, G., Roelink, H. and Jessell, T. M. (1995).Dorsal differentiation of neural plate cells induced by BMP-mediated signals from epidermal ectoderm. Cell 82, 969-979. https://doi.org/10.1016/0092-8674(95)90276-7

Lim, J.-H. A., Stafford, B. K., Nguyen, P. L., Lien, B. V., Wang, C., Zukor, K., et al. (2016). Neural activity promotes long-distance, target-specific regeneration of adult retinal axons. Nat. Neurosci. 19, 1073–1084. doi: 10.1038/nn.4340

Lin, H.-C., He, Z., Ebert, S., Schörnig, M., Santel, M., Nikolova, M. T., et al. (2021). NGN2 induces diverse neuron types from human pluripotency. Stem Cell Rep. 16, 2118–2127. doi: 10.1016/j.stemcr.2021.07.006

Lindborg, B. A., Brekke, J. H., Vegoe, A. L., Ulrich, C. B., Haider, K. T., Subramaniam, S., Venhuizen, S. L., Eide, C. R., Orchard, P. J., Chen, W. et al. (2016). Rapid induction of cerebral organoids from human induced pluripotent stem cells using a chemically defined hydrogel and defined cell culture medium. Stem Cells Transl. Med. 5, 970-979. https://doi.org/10.5966/sctm.2015-0305

Lippmann, E. S., Estevez-Silva, M. C., and Ashton, R. S. (2014). Defined human pluripotent stem cell culture enables highly efficient neuroepithelium derivation without small molecule inhibitors. Stem Cells 32, 1032–1042. doi: 10.1002/stem.1622

Lippmann, E. S., Williams, C. E., Ruhl, D. A., Estevez-Silva, M. C., Chapman, E. R., Coon, J. J., et al. (2015). Deterministic hox patterning in human pluripotent stem cell-derived neuroectoderm. Stem Cell Rep. 4, 632–644. doi: 10.1016/j.stemcr.2015.02.018

Lu, D. C., Niu, T., & Alaynick, W. A. (2015). Molecular and cellular development of spinal cord locomotor circuitry. Frontiers in Molecular Neuroscience, 8, 25. https://doi.org/10.3389/fnmol.2015.00025

Ludwig, T. E., Bergendahl, V., Levenstein, M. E., Yu, J., Probasco, M. D. and Thomson, J. A. (2006). Feeder-independent culture of human embryonic stem cells. Nat. Methods 3, 637-646. https://doi.org/10.1038/nmeth902

Ma, Y., Ramezani, A., Lewis, R., Hawley, R. G., and Thomson, J. A. (2003). High-level sustained transgene expression in human embryonic stem cells using lentiviral vectors. Stem Cells 21, 111–117. doi: 10.1634/stemcells.21-1-111

Maden, M. (2002). Retinoid signalling in the development of the central nervous system. Nature Reviews Neuroscience, 3(11), 843–853. https://doi.org/10.1038/nrn963

Mandegar, M. A., Huebsch, N., Frolov, E. B., Shin, E., Truong, A., Olvera, M. P., Chan, A. H., Miyaoka, Y., Holmes, K., Spencer, C. I. et al. (2016). CRISPR interference efficiently induces specific and reversible gene silencing in human iPSCs. Cell Stem Cell 18, 541-553. https://doi.org/10.1016/j.stem.2016.01.022

Mansfield, J. H., and McGlinn, E. (2012). Evolution, expression, and developmental function of hox-embedded miRNAs. Curr. Top. Dev. Biol. 99, 31–57. doi: 10.1016/B978-0-12-387038-4.00002-1

Marikawa, Y., Chen, H.-R., Menor, M., Deng, Y. and Alarcon, V. B. (2020). Exposure-based assessment of chemical teratogenicity using morphogenetic aggregates of human embryonic stem cells. Reprod. Toxicol. 91, 74-91. https://doi.org/10.1016/j.reprotox.2019.10.004

Marion, R. M., Strati, K., Li, H., Tejera, A., Schoeftner, S., Ortega, S., et al. (2009). Telomeres acquire embryonic stem cell characteristics in induced pluripotent stem cells. Cell Stem Cell 4, 141–154. doi: 10.1016/j.stem.2008.12.010

Martins-Green, M. and Erickson, C. A. (1986). Development of neural tube basal lamina during neurulation and neural crest cell emigration in the trunk of the mouse embryo. Development 98, 219-236. https://doi.org/10.1242/dev.98.1.219

Martyn, I., Brivanlou, A. H., & Siggia, E. D. (2019). A wave of WNT signaling balanced by secreted inhibitors controls primitive streak formation in micropattern colonies of human embryonic stem cells. Development, 146(6). https://doi.org/10.1242/dev.172791

Martyn, I., Kanno, T. Y., Ruzo, A., Siggia, E. D., & Brivanlou, A. H. (2018). Self-organization of a human organizer by combined Wnt and Nodal signalling. Nature, 558(7708), 132–135. https://doi.org/10.1038/s41586-018-0150-y

Mathis, L., Kulesa, P. M., & Fraser, S. E. (2001). FGF receptor signalling is required to maintain neural progenitors during Hensen's node progression. Nature Cell Biology, 3(6), 559–566. https://doi.org/10.1038/35078535

Matson, K. J. E., Russ, D. E., Kathe, C., Hua, I., Maric, D., Ding, Y., Krynitsky, J., Pursley, R., Sathyamurthy, A., Squair, J. W., Levi, B. P., Courtine, G., & Levine, A. J. (2022). Single cell atlas of spinal cord injury in mice reveals a pro-regenerative signature in spinocerebellar neurons. Nature Communications, 13(1), 5628. https://doi.org/10.1038/s41467-022-33184-1

Mazzoni, E. O., Mahony, S., Closser, M., Morrison, C. A., Nedelec, S., Williams, D. J., et al. (2013a). Synergistic binding of transcription factors to cell-specific enhancers programs motor neuron identity. Nat. Neurosci. 16, 1219–1227. doi: 10.1038/nn.3467

Mazzoni, E. O., Mahony, S., Peljto, M., Patel, T., Thornton, S. R., McCuine, S., et al. (2013b). Saltatory remodeling of Hox chromatin in response to rostrocaudal patterning signals. Nat. Neurosci. 16, 1191–1198. doi: 10.1038/nn.3490

McCreedy, D. A., Jalufka, F. L., Platt, M. E., Min, S. W., Kirchhoff, M. A., Pritchard, A. L., Reid, S. K., Manlapaz, R., Mihaly, E., Butts, J. C., Iyer, N. R., Sakiyama-Elbert, S. E., Crone, S. A., & McDevitt, T. C. (2021). Passive Clearing and 3D Lightsheet Imaging of the Intact and Injured Spinal Cord in Mice. Frontiers in Cellular Neuroscience, 15, 684792. https://doi.org/10.3389/fncel.2021.684792

Mcginnis, C. S., Patterson, D. M., Winkler, J., Conrad, D. N., Hein, M. Y., Srivastava, V., Hu, J. L., Murrow, L. M., Weissman, J. S., Werb, Z. et al. (2019). MULTI-seq: sample multiplexing for single-cell RNA sequencing using lipid-tagged indices. Nat. Methods 16, 619-626. https://doi.org/10.1038/s41592-019-0433-8

Meinhardt, A., Eberle, D., Tazaki, A., Ranga, A., Niesche, M., Wilsch-Bräuninger, M., Stec, A., Schackert, G., Lutolf, M. and Tanaka, E. M. (2014). 3D reconstitution of the patterned neural tube from embryonic stem cells. Stem Cell Rep. 3, 987-999. https://doi.org/10.1016/j.stemcr.2014.09.020

Menelaou, E., & McLean, D. L. (2019). Hierarchical control of locomotion by distinct types of spinal V2a interneurons in zebrafish. Nature Communications, 10. https://doi.org/10.1038/s41467-019-12240-3

Menelaou, E., VanDunk, C., & McLean, D. L. (2014). Differences in Spinal V2a Neuron Morphology Reflect Their Recruitment Order During Swimming in Larval Zebrafish. The Journal of Comparative Neurology, 522(6), 1232–1248. https://doi.org/10.1002/cne.23465

Merkle, F. T., Maroof, A., Wataya, T., Sasai, Y., Studer, L., Eggan, K., et al. (2015). Generation of neuropeptidergic hypothalamic neurons from human pluripotent stem cells. Development 142, 633–643. doi: 10.1242/dev.117978

Mertens, J., Paquola, A. C. M., Ku, M., Hatch, E., Böhnke, L., Ladjevardi, S., et al. (2015). Directly reprogrammed human neurons retain aging-associated transcriptomic signatures and reveal age-related nucleocytoplasmic defects. Cell Stem Cell 17, 705–718. doi: 10.1016/j.stem.2015.09.001

Metzis, V., Steinhauser, S., Pakanavicius, E., Gouti, M., Stamataki, D., Ivanovitch, K., et al. (2018). Nervous system regionalization entails axial allocation before neural differentiation. Cell 175, 1105–1118.e17. doi: 10.1016/j.cell.2018.09.040

Miller, J. D., Ganat, Y. M., Kishinevsky, S., Bowman, R. L., Liu, B., Tu, E. Y., et al. (2013). Human iPSC-based modeling of late-onset disease via progerin-induced aging. Cell Stem Cell 13, 691–705. doi: 10.1016/j.stem.2013.11.006

Misra, K., Luo, H., Li, S., Matise, M., & Xiang, M. (2014). Asymmetric activation of Dll4-Notch signaling by Foxn4 and proneural factors activates BMP/TGFβ signaling to specify V2b interneurons in the spinal cord. Development, 141(1), 187–198. https://doi.org/10.1242/dev.092536

Miyaoka, Y., Chan, A. H., Judge, L. M., Yoo, J., Huang, M., Nguyen, T. D., Lizarraga, P. P., So, P.-L. and Conklin, B. R. (2014). Isolation of single-base genome-edited human iPS cells without antibiotic selection. Nat. Methods 11, 291-293. https://doi.org/10.1038/nmeth.2840

Mizoguchi, T., Fukada, M., Iihama, M., Song, X., Fukagawa, S., Kuwabara, S., Omaru, S., Higashijima, S.-I., & Itoh, M. (2020). Transient activation of the Notch-her15.1 axis plays an important role in the maturation of V2b interneurons. Development, 147(16). https://doi.org/10.1242/dev.191312

Moore, N. J., Bhumbra, G. S., Foster, J. D., & Beato, M. (2015). Synaptic Connectivity between Renshaw Cells and Motoneurons in the Recurrent Inhibitory Circuit of the Spinal Cord. The Journal of Neuroscience: The Official Journal of the Society for Neuroscience, 35(40), 13673–13686. https://doi.org/10.1523/JNEUROSCI.2541-15.2015

Moris, N., Anlas, K., van den Brink, S. C., Alemany, A., Schröder, J., Ghimire, S., Balayo, T., van Oudenaarden, A., & Martinez Arias, A. (2020). An in vitro model of early anteroposterior organization during human development. Nature, 582(7812), 410–415. https://doi.org/10.1038/s41586-020-2383-9

Mossink, B., Verboven, A. H. A., van Hugte, E. J. H., Klein Gunnewiek, T. M., Parodi, G., Linda, K., et al. (2021). Human neuronal networks on micro-electrode arrays are a highly robust tool to study disease-specific genotype-phenotype correlations in vitro. Stem Cell Rep. 16, 2182–2196. doi: 10.1016/j.stemcr.2021.07.001

Mouilleau, V., Vaslin, C., Gribaudo, S., Robert, R., Nicolas, N., Jarrige, M., Terray, A., Lesueur, L., Mathis, M. W., Croft, G. et al. (2021). Dynamic extrinsic pacing of the HOX clock in human axial progenitors controls motor neuron subtype specification. Development 148, dev194514. https://doi.org/10.1242/dev.194514

Mulia, G. E., Picanço-Castro, V., Stavrou, E. F., Athanassiadou, A., and Figueiredo, M. L. (2021). Advances in the development and the applications of nonviral, episomal vectors for gene therapy. Hum. Gene Ther. 32, 1076–1095. doi: 10.1089/hum.2020.310

Muncie, J. M., Ayad, N. M. E., Lakins, J. N., Xue, X., Fu, J. and Weaver, V. M. (2020). Mechanical tension promotes formation of gastrulation-like nodes and patterns mesoderm specification in human embryonic stem cells. Dev. Cell 55, 679-694.e11. https://doi.org/10.1016/j.devcel.2020.10.015

Muñoz-Sanjuán, I., and Brivanlou, A. H. (2022). Neural induction, the default model and embryonic stem cells. Nat. Rev. Neurosci. 3, 271–280. doi: 10.1038/nrn786

Murdoch, J. N. and Copp, A. J. (2010). The relationship between Sonic hedgehog signaling, cilia and neural tube defects. Birth Defects Res. A Clin. Mol. Teratol. 88, 633-652. https://doi.org/10.1002/bdra.20686

Murisic, N., Hakim, V., Kevrekidis, I. G., Shvartsman, S. Y. and Audoly, B. (2015). From discrete to continuum models of three-dimensional deformations in epithelial sheets. Biophys. J. 109, 154-163. https://doi.org/10.1016/j.bpj.2015.05.019

Nehme, R., Zuccaro, E., Ghosh, S. D., Li, C., Sherwood, J. L., Pietilainen, O., et al. (2021). Combining NGN2 programming with developmental patterning generates human excitatory neurons with NMDAR-mediated synaptic transmission. Cell Rep. 23, 2509–2523. doi: 10.1016/j.celrep.2018.04.066

Neijts, R., & Deschamps, J. (2017). At the base of colinear Hox gene expression: Cis-features and trans-factors orchestrating the initial phase of Hox cluster activation. Developmental Biology, 428(2), 293–299. https://doi.org/10.1016/j.ydbio.2017.02.009

Neijts, R., Amin, S., van Rooijen, C., & Deschamps, J. (2017). Cdx is crucial for the timing mechanism driving colinear Hox activation and defines a trunk segment in the Hox cluster topology. Developmental Biology, 422(2), 146–154. https://doi.org/10.1016/j.ydbio.2016.12.024

Nelson, M. R., Howard, D., Jensen, O. E., King, J. R., Rose, F. R. A. J. and Waters, S. L. (2011). Growth-induced buckling of an epithelial layer. Biomech. Model. Mechanobiol. 10, 883-900. https://doi.org/10.1007/s10237-010-0280-0

Ng, A. H. M., Khoshakhlagh, P., Rojo Arias, J. E., Pasquini, G., Wang, K., Swiersy, A., et al. (2021). A comprehensive library of human transcription factors for cell fate engineering. Nat. Biotechnol. 39, 510–519. doi: 10.1038/s41587-020-0742-6

Nickolls, A. R., Lee, M. M., Espinoza, D. F., Szczot, M., Lam, R. M., Wang, Q., et al. (2020). Transcriptional programming of human mechanosensory neuron subtypes from pluripotent stem cells. Cell Rep. 30, 932–946.e7. doi: 10.1016/j.celrep.2019.12.062

Nikolopoulou, E., Galea, G. L., Rolo, A., Greene, N. D. E., & Copp, A. J. (2017). Neural tube closure: Cellular, molecular and biomechanical mechanisms. Development, 144(4), 552–566. https://doi.org/10.1242/dev.145904

Novellino, A., Scelfo, B., Palosaari, T., Price, A., Sobanski, T., Shafer, T. J., et al. (2011). Development of micro-electrode array based tests for neurotoxicity: Assessment of interlaboratory reproducibility with neuroactive chemicals. Front. Neuroeng. 4:4. doi: 10.3389/fneng.2011.00004

O'Shea, K. S. (1987). Differential deposition of basement membrane components during formation of the caudal neural tube in the mouse embryo. Development 99, 509-519. https://doi.org/10.1242/dev.99.4.509

Odawara, A., Saitoh, Y., Alhebshi, A. H., Gotoh, M., and Suzuki, I. (2014). Long-term electrophysiological activity and pharmacological response of a human induced pluripotent stem cell-derived neuron and astrocyte co-culture. Biochem. Biophys. Res. Commun. 443, 1176–1181. doi: 10.1016/j.bbrc.2013.12.142

Oginuma, M., Harima, Y., Tarazona, O. A., Diaz-Cuadros, M., Michaut, A., Ishitani, T., Xiong, F. and Pourquié, O. (2020). Intracellular pH controls WNT downstream of glycolysis in amniote embryos. Nature 584, 98-101. https://doi.org/10.1038/s41586-020-2428-0

Oginuma, M., Moncuquet, P., Xiong, F., Karoly, E., Chal, J., Guevorkian, K. and Pourquié, O. (2017). A gradient of glycolytic activity coordinates FGF and Wnt signaling during elongation of the body axis in amniote embryos. Dev. Cell 40, 342-353.e10. https://doi.org/10.1016/j.devcel.2017.02.001

Okada, Y., Shimazaki, T., Sobue, G. and Okano, H. (2004). Retinoic-acid-concentration-dependent acquisition of neural cell identity during in vitro differentiation of mouse embryonic stem cells. Dev. Biol. 275, 124-142. https://doi.org/10.1016/j.ydbio.2004.07.038

Ordreau, A., Kraus, F., Zhang, J., An, H., Park, S., Ahfeldt, T., et al. (2021). Temporal proteomics during neurogenesis reveals large-scale proteome and organelle remodeling via selective autophagy. Mol. Cell 81, 5082–5098.e11. doi: 10.1016/j.molcel.2021.10.001

Ortmann, D. and Vallier, L. (2017). Variability of human pluripotent stem cell lines. Curr. Opin. Genet. Dev. 46, 179-185. https://doi.org/10.1016/j.gde.2017.07.004

Osafune, K., Caron, L., Borowiak, M., Martinez, R. J., Fitz-Gerald, C. S., Sato, Y., et al. (2008). Marked differences in differentiation propensity among human embryonic stem cell lines. Nat. Biotechnol. 26, 313–315. doi: 10.1038/nbt1383

Osseward, P. J., Amin, N. D., Moore, J. D., Temple, B. A., Barriga, B. K., Bachmann, L. C., et al. (2021). Conserved genetic signatures parcellate cardinal spinal neuron classes into local and projection subsets. Science 372, 385–393. doi: 10.1126/science.abe0690

Ozair, M. Z., Kintner, C., & Brivanlou, A. H. (2012). Neural induction and early patterning in vertebrates. Wiley Interdisciplinary Reviews. Developmental Biology, 2(4), 479. https://doi.org/10.1002/wdev.90

Pagan-Diaz, G. J., Drnevich, J., Ramos-Cruz, K. P., Sam, R., Sengupta, P., and Bashir, R. (2020). Modulating electrophysiology of motor neural networks via optogenetic stimulation during neurogenesis and synaptogenesis. Sci. Rep. 10:12460. doi: 10.1038/s41598-020-68988-y

Panayi, H., Panayiotou, E., Orford, M., Genethliou, N., Mean, R., Lapathitis, G., Li, S., Xiang, M., Kessaris, N., Richardson, W. D., & Malas, S. (2010). Sox1 is required for the specification of a novel p2-derived interneuron subtype in the mouse ventral spinal cord. The Journal of Neuroscience, 30(37), 12274–12280. https://doi.org/10.1523/JNEUROSCI.2402-10.2010

Park, S., Kim, D., Jung, Y.-G. and Roh, S. (2015). Thiazovivin, a Rho kinase inhibitor, improves stemness maintenance of embryo-derived stem-like cells under chemically defined culture conditions in cattle. Anim. Reprod. Sci 161, 47-57. https://doi.org/10.1016/j.anireprosci.2015.08.003

Park, S., Koppes, R. A., Froriep, U. P., Jia, X., Achyuta, A. K. H., McLaughlin, B. L., et al. (2015). Optogenetic control of nerve growth. Sci. Rep. 5:9669. doi: 10.1038/srep09669

Parker, H. J., and Krumlauf, R. (2020). A hox gene regulatory network for hindbrain segmentation. Curr. Top. Dev. Biol. 139, 169–203. doi: 10.1016/bs.ctdb.2020.03.001

Peng, C.-Y., Yajima, H., Burns, C. E., Zon, L. I., Sisodia, S. S., Pfaff, S. L., et al. (2007). Notch and MAML signaling drives Scl-dependent interneuron diversity in the spinal cord. Neuron 53, 813–827. doi: 10.1016/j.neuron.2007.02.019

Pennimpede, T., Proske, J., König, A., Vidigal, J. A., Morkel, M., Bramsen, J. B., Herrmann, B. G. and Wittler, L. (2012). In vivo knockdown of Brachyury results in skeletal defects and urorectal malformations resembling caudal regression syndrome. Dev. Biol. 372, 55-67. https://doi.org/10.1016/j.ydbio.2012.09.003

Petersen, E. D., Sharkey, E. D., Pal, A., Shafau, L. O., Zenchak-Petersen, J., Peña, A. J., et al. (2021). Restoring function after severe spinal cord injury through bioluminescent-optogenetics. Front. Neurol. 12:792643. doi: 10.3389/fneur.2021.792643

Philippidou, P., and Dasen, J. S. (2013). Hox genes: Choreographers in neural development, architects of circuit organization. Neuron 80, 12–34. doi: 10.1016/j.neuron.2013.09.020

Piao, J., Zabierowski, S., Dubose, B. N., Hill, E. J., Navare, M., Claros, N., et al. (2021). Preclinical efficacy and safety of a human embryonic stem cell-derived midbrain dopamine progenitor product, MSK-DA01. Cell Stem Cell 28, 217–229.e7. doi: 10.1016/j.stem.2021.01.004

Placzek, M., & Briscoe, J. (2005). The floor plate: Multiple cells, multiple signals. Nature Reviews. Neuroscience, 6(3), 230–240. https://doi.org/10.1038/nrn1628

Pliner, H.A., Packer, J.S., McFaline-Figueroa, J.L., Cusanovich, D.A., Daza, R.M., Aghamirzaie, D., Srivatsan, S., Qiu, X., Jackson, D., Minkina, A., et al. (2018). Cicero Predicts cis-Regulatory DNA Interactions from Single-Cell Chromatin Accessibility Data. Mol. Cell 71, 858-871.e8. https://doi.org/10.1016/j.molcel.2018.06.044.

Pollen, A. A., Bhaduri, A., Andrews, M. G., Nowakowski, T. J., Meyerson, O. S., Mostajo-Radji, M. A., et al. (2019). Establishing cerebral organoids as models of human-specific brain evolution. Cell 176, 743–756.e17. doi: 10.1016/j.cell.2019.01.017

Qian, X., Nguyen, H. N., Song, M. M., Hadiono, C., Ogden, S. C., Hammack, C., et al. (2016). Brain-region-specific organoids using mini-bioreactors for modeling ZIKV exposure. Cell 165, 1238–1254. doi: 10.1016/j.cell.2016.04.032

Rayon, T., Maizels, R. J., Barrington, C., & Briscoe, J. (2021). Single-cell transcriptome profiling of the human developing spinal cord reveals a conserved genetic programme with human-specific features. Development, 148(15), dev199711. https://doi.org/10.1242/dev.199711

Rekaik, H., Lopez-Delisle, L., Hintermann, A., Mascrez, B., Bochaton, C., Mayran, A., & Duboule, D. (2023). Sequential and directional insulation by conserved CTCF sites underlies the Hox timer in stembryos. Nature Genetics, 55(7), 1164–1175. https://doi.org/10.1038/s41588-023-01426-7

Rekler, D., & Kalcheim, C. (2021). From neural crest to definitive roof plate: The dynamic behavior of the dorsal neural tube. International Journal of Molecular Sciences, 22(8). https://doi.org/10.3390/ijms22083911

Rifes, P., Isaksson, M., Rathore, G. S., Aldrin-Kirk, P., Møller, O. K., Barzaghi, G., Lee, J., Egerod, K. L., Rausch, D. M., Parmar, M., Pers, T. H., Laurell, T., & Kirkeby, A. (2020). Modeling neural tube development by differentiation of human embryonic stem cells in a microfluidic WNT gradient. Nature Biotechnology, 38(11), 1265–1273. https://doi.org/10.1038/s41587-020-0525-0

Roese-Koerner, B., Stappert, L., Berger, T., Braun, N. C., Veltel, M., Jungverdorben, J., et al. (2016). Reciprocal regulation between bifunctional miR-9/9(*) and its transcriptional modulator notch in human neural stem cell self-renewal and differentiation. Stem Cell Rep. 7, 207–219. doi: 10.1016/j.stemcr.2016.06.008

Roig-Merino, A., Urban, M., Bozza, M., Peterson, J. D., Bullen, L., Büchler-Schäff, M., et al. (2022). An episomal DNA vector platform for the persistent genetic modification of pluripotent stem cells and their differentiated progeny. Stem Cell Rep. 17, 143–158. doi: 10.1016/j.stemcr.2021.11.011

Rowitch, D. H., & Kriegstein, A. R. (2010). Developmental genetics of vertebrate glial-cell specification. Nature, 468(7321), 214–222. https://doi.org/10.1038/nature09611

Russo, G. L., Sonsalla, G., Natarajan, P., Breunig, C. T., Bulli, G., Merl-Pham, J., et al. (2021). CRISPR-mediated induction of neuron-enriched mitochondrial proteins boosts direct glia-to-neuron conversion. Cell Stem Cell 28, 524–534.e7. doi: 10.1016/j.stem.2020.10.015

Sagner, A., and Briscoe, J. (2019). Establishing neuronal diversity in the spinal cord: A time and a place. Development 146:182154. doi: 10.1242/dev.182154

Sagy, N., Slovin, S., Allalouf, M., Pour, M., Savyon, G., Boxman, J. and Nachman, I. (2019). Prediction and control of symmetry breaking in embryoid bodies by environment and signal integration. Development 146, dev181917. https://doi.org/10.1242/dev.181917

Salamatina, A., Yang, J. H., Brenner-Morton, S., Bikoff, J. B., Fang, L., Kintner, C. R., et al. (2020). Differential loss of spinal interneurons in a mouse model of ALS. Neuroscience 450, 81–95. doi: 10.1016/j.neuroscience.2020.08.011

Samuel, R. M., Navickas, A., Maynard, A., Gaylord, E. A., Garcia, K., Bhat, S., Majd, H., Richter, M. N., Elder, N., Le, D., Nguyen, P., Shibata, B., Llabata, M. L., Selleri, L., Laird, D. J., Darmanis, S., Goodarzi, H., & Fattahi, F. (2023). Generation of Schwann cell derived melanocytes from hPSCs identifies pro-metastatic factors in melanoma. BioRxiv. https://doi.org/10.1101/2023.03.06.531220

Satir, T. M., Nazir, F. H., Vizlin-Hodzic, D., Hardselius, E., Blennow, K., Wray, S., et al. (2020). Author correction: Accelerated neuronal and synaptic maturation by BrainPhys medium increases Aβ secretion and alters Aβ peptide ratios from iPSC-derived cortical neurons. Sci. Rep. 10:3993. doi: 10.1038/s41598-020-61008-z

Schiffmann, Y. (2006). Symmetry breaking and convergent extension in early chordate development. Prog. Biophys. Mol. Biol. 92, 209-231. https://doi.org/10.1016/j.pbiomolbio.2005.10.002

Schweitzer, J. S., Song, B., Herrington, T. M., Park, T.-Y., Lee, N., Ko, S., et al. (2020). Personalized iPSC-derived dopamine progenitor cells for Parkinson's disease. N. Engl. J. Med. 382, 1926–1932. doi: 10.1056/NEJMoa1915872

Sheng, G. (2015). Epiblast morphogenesis before gastrulation. Developmental Biology, 401(1), 17–24. https://doi.org/10.1016/j.ydbio.2014.10.003

Shi, Y., Kirwan, P., Smith, J., Robinson, H. P. C. and Livesey, F. J. (2012). Human cerebral cortex development from pluripotent stem cells to functional excitatory synapses. Nat. Neurosci. 15, 477-486. https://doi.org/10.1038/nn.3041

Shi, Y., Lin, S., Staats, K. A., Li, Y., Chang, W.-H., Hung, S.-T., Hendricks, E., Linares, G. R., Wang, Y., Son, E. Y., et al. (2018). Haploinsufficiency leads to neurodegeneration in C9ORF72 ALS/FTD human induced motor neurons. Nat. Med. 24, 313–325. doi:10.1038/nm.4490.

Shum, A. S. W., Poon, L. L. M., Tang, W. W. T., Koide, T., Chan, B. W. H., Leung, Y.-C. G., Shiroishi, T. and Copp, A. J. (1999). Retinoic acid induces down-regulation of Wnt-3a, apoptosis and diversion of tail bud cells to a neural fate in the mouse embryo. Mech. Dev. 84, 17-30. https://doi.org/10.1016/S0925-4773(99)00059-3

Simpson, D. J., Olova, N. N., and Chandra, T. (2021). Cellular reprogramming and epigenetic rejuvenation. Clin. Epigenet. 13:170. doi: 10.1186/s13148-021-01158-7

Sloan, S. A., Andersen, J., Paşca, A. M., Birey, F., and Paşca, S. P. (2018). Generation and assembly of human brain region-specific three-dimensional cultures. Nat. Prot. 13, 2062–2085. doi: 10.1038/s41596-018-0032-7

Smith, J. R., Vallier, L., Lupo, G., Alexander, M., Harris, W. A., and Pedersen, R. A. (2008). Inhibition of activin/nodal signaling promotes specification of human embryonic stem cells into neuroectoderm. Dev. Biol. 313, 107–117. doi: 10.1016/j.ydbio.2007.10.003

Song, M.-R., Sun, Y., Bryson, A., Gill, G. N., Evans, S. M., and Pfaff, S. L. (2009). Islet-to-LMO stoichiometries control the function of transcription complexes that specify motor neuron and V2a interneuron identity. Development 136, 2923–2932. doi: 10.1242/dev.037986

Squair, J. W., Gautier, M., Mahe, L., Soriano, J. E., Rowald, A., Bichat, A., et al. (2021). Neuroprosthetic baroreflex controls haemodynamics after spinal cord injury. Nature 590, 308–314. doi: 10.1038/s41586-020-03180-w

Squair, J. W., Milano, M., de Coucy, A., Gautier, M., Skinnider, M. A., James, N. D., Cho, N., Lasne, A., Kathe, C., Hutson, T. H., Ceto, S., Baud, L., Galan, K., Aureli, V., Laskaratos, A., Barraud, Q., Deming, T. J., Kohman, R. E., Schneider, B. L., … Anderson, M. A. (2023). Recovery of walking after paralysis by regenerating characterized neurons to their natural target region. Science, 381(6664), 1338–1345. https://doi.org/10.1126/science.adi6412

Sternfeld, M. J., Hinckley, C. A., Moore, N. J., Pankratz, M. T., Hilde, K. L., Driscoll, S. P., Hayashi, M., Amin, N. D., Bonanomi, D., Gifford, W. D., Sharma, K., Goulding, M., & Pfaff, S. L. (2017). Speed and segmentation control mechanisms characterized in rhythmically-active circuits created from spinal neurons produced from genetically-tagged embryonic stem cells. eLife, 6. https://doi.org/10.7554/eLife.21540

Steventon, B., Duarte, F., Lagadec, R., Mazan, S., Nicolas, J.-F. and Hirsinger, E. (2016). Species-specific contribution of volumetric growth and tissue convergence to posterior body elongation in vertebrates. Development 143, 1732-1741. https://doi.org/10.1242/dev.126375

Strano, A., Tuck, E., Stubbs, V. E., and Livesey, F. J. (2020). Variable outcomes in neural differentiation of human PSCs arise from intrinsic differences in developmental signaling pathways. Cell Rep. 31:107732. doi: 10.1016/j.celrep.2020.107732

Suhr, S. T., Chang, E. A., Tjong, J., Alcasid, N., Perkins, G. A., Goissis, M. D., et al. (2010). Mitochondrial rejuvenation after induced pluripotency. PLoS One 5:e14095. doi: 10.1371/journal.pone.0014095

Sweeney, L. B., Bikoff, J. B., Gabitto, M. I., Brenner-Morton, S., Baek, M., Yang, J. H., Tabak, E. G., Dasen, J. S., Kintner, C. R., & Jessell, T. M. (2018). Origin and segmental diversity of spinal inhibitory interneurons. Neuron, 97(2), 341-355.e3. https://doi.org/10.1016/j.neuron.2017.12.029

Takahashi, K., and Yamanaka, S. (2006). Induction of pluripotent stem cells from mouse embryonic and adult fibroblast cultures by defined factors. Cell 126, 663–676. doi: 10.1016/j.cell.2006.07.024

Takahashi, K., Tanabe, K., Ohnuki, M., Narita, M., Ichisaka, T., Tomoda, K., & Yamanaka, S. (2007). Induction of pluripotent stem cells from adult human fibroblasts by defined factors. Cell, 131(5), 861–872. https://doi.org/10.1016/j.cell.2007.11.019

Takemoto, T., Uchikawa, M., Kamachi, Y., & Kondoh, H. (2006). Convergence of Wnt and FGF signals in the genesis of posterior neural plate through activation of the Sox2 enhancer N-1. Development, 133(2), 297–306. https://doi.org/10.1242/dev.02196

Takemoto, T., Uchikawa, M., Yoshida, M., Bell, D. M., Lovell-Badge, R., Papaioannou, V. E., & Kondoh, H. (2011). Tbx6-dependent Sox2 regulation determines neural or mesodermal fate in axial stem cells. Nature, 470(7334), 394–398. https://doi.org/10.1038/nature09729

Tanabe, Y. and Jessell, T. M. (1996). Diversity and Pattern in the Developing Spinal Cord. Science 274, 1115-1123. https://doi.org/10.1126/science.274.5290.1115

Tanabe, Y., William, C., and Jessell, T. M. (1998). Specification of motor neuron identity by the MNR2 homeodomain protein. Cell 95, 67–80. doi: 10.1016/s0092-8674(00)81783-3

Tang, H., Hammack, C., Ogden, S. C., Wen, Z., Qian, X., Li, Y., et al. (2016). Zika virus infects human cortical neural progenitors and attenuates their growth. Cell Stem Cell 18, 587–590. doi: 10.1016/j.stem.2016.02.016

Tang, X., Zhou, L., Wagner, A. M., Marchetto, M. C. N., Muotri, A. R., Gage, F. H., et al. (2013). Astroglial cells regulate the developmental timeline of human neurons differentiated from induced pluripotent stem cells. Stem Cell Res. 11, 743–757. doi: 10.1016/j.scr.2013.05.002

Teratani-Ota, Y., Yamamizu, K., Piao, Y., Sharova, L., Amano, M., Yu, H., et al. (2016). Induction of specific neuron types by overexpression of single transcription factors. Vitro Cell Dev. Biol. Anim. 52, 961–973. doi: 10.1007/s11626-016-0056-7

Thaler, J. P., Lee, S.-K., Jurata, L. W., Gill, G. N., & Pfaff, S. L. (2002). LIM Factor Lhx3 Contributes to the Specification of Motor Neuron and Interneuron Identity through Cell-Type-Specific Protein-Protein Interactions. Cell, 110(2), 237–249. https://doi.org/10.1016/S0092-8674(02)00823-1

Thomson, J. A., Itskovitz-Eldor, J., Shapiro, S. S., Waknitz, M. A., Swiergiel, J. J., Marshall, V. S., & Jones, J. M. (1998). Embryonic stem cell lines derived from human blastocysts. Science, 282(5391), 1145–1147. https://doi.org/10.1126/science.282.5391.1145

Tian, R., Gachechiladze, M. A., Ludwig, C. H., Laurie, M. T., Hong, J. Y., Nathaniel, D., et al. (2019). CRISPR interference-based platform for multimodal genetic screens in human iPSC-derived neurons. Neuron 104, 239–255.e12. doi: 10.1016/j.neuron.2019.07.014

Toda, S., Blauch, L. R., Tang, S. K. Y., Morsut, L., and Lim, W. A. (2018). Programming self-organizing multicellular structures with synthetic cell-cell signaling. Science 361, 156–162. doi: 10.1126/science.aat0271

Toda, S., McKeithan, W. L., Hakkinen, T. J., Lopez, P., Klein, O. D., and Lim, W. A. (2020). Engineering synthetic morphogen systems that can program multicellular patterning. Science. 370, 327–331.

Trushko, A., Di Meglio, I., Merzouki, A., Blanch-Mercader, C., Abuhattum, S., Guck, J., Alessandri, K., Nassoy, P., Kruse, K., Chopard, B. et al. (2020). Buckling of an epithelium growing under spherical confinement. Dev. Cell 54, 655-668.e6. https://doi.org/10.1016/j.devcel.2020.07.019

Tung, Y.-T., Lu, Y.-L., Peng, K.-C., Yen, Y.-P., Chang, M., Li, J., et al. (2015). Mir-17~92 governs motor neuron subtype survival by mediating nuclear PTEN. Cell Rep. 11, 1305–1318. doi: 10.1016/j.celrep.2015.04.050

Tzouanacou, E., Wegener, A., Wymeersch, F. J., Wilson, V., and Nicolas, J.-F. (2009). Redefining the progression of lineage segregations during mammalian embryogenesis by clonal analysis. Dev. Cell 17, 365–376. doi: 10.1016/j.devcel.2009.08.002

Ulloa, F., Itasaki, N., & Briscoe, J. (2007). Inhibitory Gli3 activity negatively regulates Wnt/beta-catenin signaling. Current Biology, 17(6), 545–550. https://doi.org/10.1016/j.cub.2007.01.062

Valiulahi, P., Vidyawan, V., Puspita, L., Oh, Y., Juwono, V. B., Sittipo, P., et al. (2021). Generation of caudal-type serotonin neurons and hindbrain-fate organoids from hPSCs. Stem Cell Rep. 16, 1938–1952. doi: 10.1016/j.stemcr.2021.06.006

van den Akker, E., Forlani, S., Chawengsaksophak, K., De Graaff, W., Beck, F., Meyer, B. I. and Deschamps, J. (2002). Cdx1 and Cdx2 have overlapping functions in anteroposterior patterning and posterior axis elongation. Development 129, 2181-2193. https://doi.org/10.1242/dev.129.9.2181

van den Brink, S. C. . ., Alemany, A., van Batenburg, V., Moris, N., Blotenburg, M., Vivié, J., Baillie-Johnson, P., Nichols, J., Sonnen, K. F., Martinez Arias, A. et al. (2020). Single-cell and spatial transcriptomics reveal somitogenesis in gastruloids. Nature 582, 405-409. https://doi.org/10.1038/s41586-020-2024-3

van den Brink, S. C., Baillie-Johnson, P., Balayo, T., Hadjantonakis, A.-K., Nowotschin, S., Turner, D. A., & Martinez Arias, A. (2014). Symmetry breaking, germ layer specification and axial organisation in aggregates of mouse embryonic stem cells. Development, 141(22), 4231–4242. https://doi.org/10.1242/dev.113001

van der Walt, S., Schönberger, J. L., Nunez-Iglesias, J., Boulogne, F., Warner, J. D., Yager, N., Gouillart, E. and Yu, T. and the scikit-image contributors (2014). scikit-image: image processing in Python. PeerJ 2, e453. https://doi.org/10.7717/peerj.453

Veenvliet, J. V., Bolondi, A., Kretzmer, H., Haut, L., Scholze-Wittler, M., Schifferl, D., Koch, F., Guignard, L., Kumar, A. S., Pustet, M. et al. (2020). Mouse embryonic stem cells self-organize into trunk-like structures with neural tube and somites. Science 370, eaba4937. https://doi.org/10.1126/science.aba4937

Veenvliet, J. V., Lenne, P.-F., Turner, D. A., Nachman, I., & Trivedi, V. (2021). Sculpting with stem cells: How models of embryo development take shape. Development, 148(24). https://doi.org/10.1242/dev.192914

Verrier, L., Davidson, L., Gierliński, M., Dady, A., & Storey, K. G. (2018). Neural differentiation, selection and transcriptomic profiling of human neuromesodermal progenitor-like cells in vitro. Development, 145(16). https://doi.org/10.1242/dev.166215

Vierbuchen, T., Ostermeier, A., Pang, Z. P., Kokubu, Y., Südhof, T. C., and Wernig, M. (2010). Direct conversion of fibroblasts to functional neurons by defined factors. Nature 463, 1035–1041. doi: 10.1038/nature08797

Vila, O. F., Chavez, M., Ma, S. P., Yeager, K., Zholudeva, L. V., Colón-Mercado, J. M., et al. (2021). Bioengineered optogenetic model of human neuromuscular junction. Biomaterials 276:121033. doi: 10.1016/j.biomaterials.2021.121033

Volpato, V., Smith, J., Sandor, C., Ried, J. S., Baud, A., Handel, A., et al. (2018). Reproducibility of molecular phenotypes after long-term differentiation to human iPSC-derived neurons: A multi-site omics study. Stem Cell Rep. 11, 897–911. doi: 10.1016/j.stemcr.2018.08.013

Wang, C., Ward, M. E., Chen, R., Liu, K., Tracy, T. E., Chen, X., et al. (2017). Scalable production of iPSC-derived human neurons to identify tau-lowering compounds by high-content screening. Stem Cell Rep. 9, 1221–1233. doi: 10.1016/j.stemcr.2017.08.019

Wang, T., Yuan, W., Liu, Y., Zhang, Y., Wang, Z., Zhou, X., Ning, G., Zhang, L., Yao, L., Feng, S., & Kong, X. (2014). The role of the JAK-STAT pathway in neural stem cells, neural progenitor cells and reactive astrocytes after spinal cord injury. Biomedical Reports, 3(2), 141. https://doi.org/10.3892/br.2014.401

Ward, P. J., Jones, L. N., Mulligan, A., Goolsby, W., Wilhelm, J. C., and English, A. W. (2016). Optically-induced neuronal activity is sufficient to promote functional motor axon regeneration in vivo. PLoS One 11:e0154243. doi: 10.1371/journal.pone.0154243

Warmflash, A., Sorre, B., Etoc, F., Siggia, E. D., & Brivanlou, A. H. (2014). A method to recapitulate early embryonic spatial patterning in human embryonic stem cells. Nature Methods, 11(8), 847–854. https://doi.org/10.1038/nmeth.3016

Warren, L., Manos, P. D., Ahfeldt, T., Loh, Y.-H., Li, H., Lau, F., et al. (2010). Highly efficient reprogramming to pluripotency and directed differentiation of human cells with synthetic modified mRNA. Cell Stem Cell 7, 618–630. doi: 10.1016/j.stem.2010.08.012

Wichterle, H., Lieberam, I., Porter, J. A., and Jessell, T. M. (2002). Directed differentiation of embryonic stem cells into motor neurons. Cell 110, 385–397. doi: 10.1016/s0092-8674(02)00835-8

Wilson, V. and Beddington, R. (1997). Expression of T protein in the primitive streak is necessary and sufficient for posterior mesoderm movement and somite differentiation. Dev. Biol. 192, 45-58. https://doi.org/10.1006/dbio.1997.8701

Wilson, V., Olivera-Martinez, I. and Storey, K. G. (2009). Stem cells, signals and vertebrate body axis extension. Development 136, 1591-1604. https://doi.org/10.1242/dev.021246

Wilson, V., Rashbass, P. and Beddington, R. S. (1993). Chimeric analysis of T (Brachyury) gene function. Development 117, 1321-1331. https://doi.org/10.1242/dev.117.4.1321

Wind, M., Gogolou, A., Manipur, I., Granata, I., Butler, L., Andrews, P. W., et al. (2021). Defining the signalling determinants of a posterior ventral spinal cord identity in human neuromesodermal progenitor derivatives. Development 148:194415. doi: 10.1242/dev.194415

Wolf, F.A., Angerer, P., and Theis, F.J. (2018). SCANPY: large-scale single-cell gene expression data analysis. Genome Biol. 19, 15. https://doi.org/10.1186/s13059-017-1382-0.

Wu, D., Jin, Y., Shapiro, T. M., Hinduja, A., Baas, P. W., and Tom, V. J. (2020). Chronic neuronal activation increases dynamic microtubules to enhance functional axon regeneration after dorsal root crush injury. Nat. Commun. 11:6131. doi: 10.1038/s41467-020-19914-3

Wymeersch, F. J., Huang, Y., Blin, G., Cambray, N., Wilkie, R., Wong, F. C. K., et al. (2016). Position-dependent plasticity of distinct progenitor types in the primitive streak. eLife 5:e10042. doi: 10.7554/eLife.10042

Wymeersch, F. J., Skylaki, S., Huang, Y., Watson, J. A., Economou, C., Marek-Johnston, C., Tomlinson, S. R., & Wilson, V. (2019). Transcriptionally dynamic progenitor populations organised around a stable niche drive axial patterning. Development, 146(1). https://doi.org/10.1242/dev.168161

Wymeersch, F. J., Wilson, V. and Tsakiridis, A. (2021). Understanding axial progenitor biology in vivo and in vitro. Development 148, dev180612. https://doi.org/10.1242/dev.180612

Xue, X., Kim, Y. S., Ponce-Arias, A.-I., O'Laughlin, R., Yan, R. Z., Kobayashi, N., Tshuva, R. Y., Tsai, Y.-H., Sun, S., Zheng, Y., Liu, Y., Wong, F. C. K., Surani, A., Spence, J. R., Song, H., Ming, G.-L., Reiner, O., & Fu, J. (2024). A patterned human neural tube model using microfluidic gradients. Nature, 628(8007), 391–399. https://doi.org/10.1038/s41586-024-07204-7

Yamaguchi, T. P. (2001). Heads or tails: Wnts and anterior–posterior patterning. Curr. Biol. 11, R713-R724. https://doi.org/10.1016/S0960-9822(01)00417-1

Yang, N., Chanda, S., Marro, S., Ng, Y.-H., Janas, J. A., Haag, D., et al. (2017). Generation of pure GABAergic neurons by transcription factor programming. Nat. Methods 14, 621–628. doi: 10.1038/nmeth.4291

Yang, Y., Jiao, J., Gao, R., Le, R., Kou, X., Zhao, Y., et al. (2015). Enhanced rejuvenation in induced pluripotent stem cell-derived neurons compared with directly converted neurons from an aged mouse. Stem Cells Dev. 24, 2767–2777. doi: 10.1089/scd.2015.0137

Yates, J. L., Warren, N., and Sugden, B. (1985). Stable replication of plasmids derived from epstein-barr virus in various mammalian cells. Nature 313, 812–815. doi: 10.1038/313812a0

Yoo, A. S., Sun, A. X., Li, L., Shcheglovitov, A., Portmann, T., Li, Y., et al. (2011). MicroRNA-mediated conversion of human fibroblasts to neurons. Nature 476, 228–231. doi: 10.1038/nature10323

Yu, G., Wang, L.-G., Han, Y. and He, Q.-Y. (2012). clusterProfiler: an R package for comparing biological themes among gene clusters. OMICS: A J. Integr. Biol. 16, 284-287. https://doi.org/10.1089/omi.2011.0118

Yu, J., Vodyanik, M. A., Smuga-Otto, K., Antosiewicz-Bourget, J., Frane, J. L., Tian, S., et al. (2007). Induced pluripotent stem cell lines derived from human somatic cells. Science 318, 1917–1920. doi: 10.1126/science.1151526

Zhang, Y., Pak, C., Han, Y., Ahlenius, H., Zhang, Z., Chanda, S., et al. (2013). Rapid single-step induction of functional neurons from human pluripotent stem cells. Neuron 78, 785–798. doi: 10.1016/j.neuron.2013.05.029

Zhang, Y., Zhang, Z., Chen, P., Ma, C. Y., Li, C., Au, T. Y. K., Tam, V., Peng, Y., Wu, R., Cheung, K. M. C. et al. (2020). Directed differentiation of notochord-like and nucleus pulposus-like cells using human pluripotent stem cells. Cell Rep. 30, 2791-2806.e5. https://doi.org/10.1016/j.celrep.2020.01.100

Zhang, Z., Yu, D., Seo, M., Hersh, C. P., Weiss, S. T. and Qiu, W. (2019). Novel Data Transformations for RNA-seq differential expression analysis. Sci. Rep. 9, 4820. https://doi.org/10.1038/s41598-019-41315-w

Zheng, Y., Xue, X., Resto-Irizarry, A. M., Li, Z., Shao, Y., Zheng, Y., Zhao, G. and Fu, J. (2019). Dorsal-ventral patterned neural cyst from human pluripotent stem cells in a neurogenic niche. Sci. Adv. 5, eaax5933. https://doi.org/10.1126/sciadv.aax5933

Zholudeva, L. V., & Lane, M. A. (2019). Choosing the right cell for spinal cord repair. Journal of Neuroscience Research, 97(2), 109–111. https://doi.org/10.1002/jnr.24351

Zholudeva, L. V., and Lane, M. A. (2019). Transplanting cells for spinal cord repair: Who, what, when, where and why? Cell Trans. 28, 388–399. doi: 10.1177/0963689718824097

Zholudeva, L. V., Fortino, T., Agrawal, A., Vila, O. F., Williams, M., McDevitt, T., Lane, M. A., & Srivastava, D. (2024). Human spinal interneurons repair the injured spinal cord through synaptic integration. BioRxiv. https://doi.org/10.1101/2024.01.11.575264

Zholudeva, L. V., Iyer, N., Qiang, L., Spruance, V. M., Randelman, M. L., White, N. W., Bezdudnaya, T., Fischer, I., Sakiyama-Elbert, S. E., & Lane, M. A. (2018). Transplantation of Neural Progenitors and V2a Interneurons after Spinal Cord Injury. Journal of Neurotrauma, 35(24), 2883–2903. https://doi.org/10.1089/neu.2017.5439

Zholudeva, L. V., Karliner, J. S., Dougherty, K. J., & Lane, M. A. (2017). Anatomical Recruitment of Spinal V2a Interneurons into Phrenic Motor Circuitry after High Cervical Spinal Cord Injury. Journal of Neurotrauma, 34(21), 3058–3065. https://doi.org/10.1089/neu.2017.5045

Zholudeva, L. V., Qiang, L., Marchenko, V., Dougherty, K. J., Sakiyama-Elbert, S. E., and Lane, M. A. (2018). The neuroplastic and therapeutic potential of spinal interneurons in the injured spinal cord. Trends Neurosci. 41, 625–639. doi: 10.1016/j.tins.2018.06.004

Zhong, G., Droho, S., Crone, S. A., Dietz, S., Kwan, A. C., Webb, W. W., Sharma, K. and Harris-Warrick, R. M. (2010). Electrophysiological Characterization of V2a Interneurons and Their Locomotor-Related Activity in the Neonatal Mouse Spinal Cord. J. Neurosci. 30, 170-182. https://doi.org/10.1523/JNEUROSCI.4849-09.2010

Zhou, J., Kim, H. Y., Davidson, L. A. (2009). Actomyosin stiffens the vertebrate embryo during crucial stages of elongation and neural tube closure. Development 136, 677-688. https://doi.org/10.1242/dev.026211

Zhou, T., Tan, L., Cederquist, G. Y., Fan, Y., Hartley, B. J., Mukherjee, S., Tomishima, M., Brennand, K. J., Zhang, Q., Schwartz, R. E. et al. (2017). High-content screening in hPSC-neural progenitors identifies drug candidates that inhibit Zika virus infection in fetal-like organoids and adult brain. Cell Stem Cell 21, 274-283.e5. https://doi.org/10.1016/j.stem.2017.06.017

Publishing Agreement

It is the policy of the University to encourage open access and broad distribution of all theses, dissertations, and manuscripts. The Graduate Division will facilitate the distribution of UCSF theses, dissertations, and manuscripts to the UCSF Library for open access and distribution. UCSF will make such theses, dissertations, and manuscripts accessible to the public and will take reasonable steps to preserve these works in perpetuity.

I hereby grant the non-exclusive, perpetual right to The Regents of the University of California to reproduce, publicly display, distribute, preserve, and publish copies of my thesis, dissertation, or manuscript in any form or media, now existing or later derived, including access online for teaching, research, and public service purposes.

DocuSigned by:
Nicholas Elder
E69D0A649AD843F...
Author Signature

12/3/2024
Date